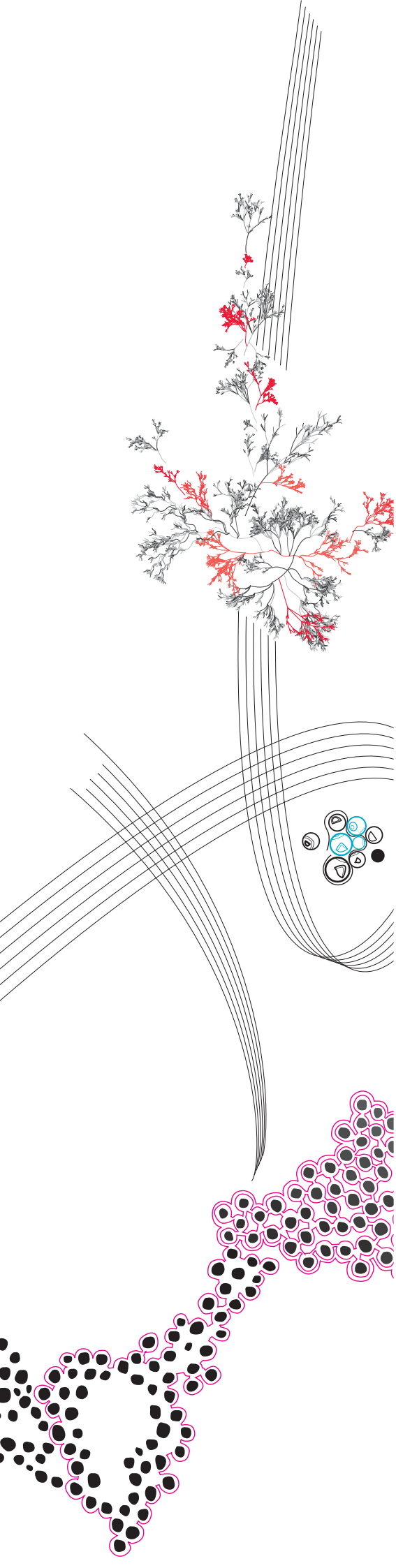

UNIVERSITY OF TWENTE.

Faculty of Electrical Engineering,
Mathematics & Computer Science

The influence of feedforward inhibition on spontaneous and evoked activity in coupled neural mass models

Lucas F. Jansen Klomp

M.Sc. Thesis
September 2021

Graduation committee:
dr. H.G.E. Meijer
dr. V. Ramírez
prof. dr. C. Brune

Summary

Epilepsy is a common neurological disorder affecting between 0.4-1% of the population. When anti-epileptic drugs are not viable and a focus from which seizures arise can be assigned, removing the epileptogenic zone through surgery is an option. This type of surgery currently has a 40-80% success rate, depending on the center, cohort and epilepsy and surgery characteristics. Therefore, it is desirable to improve the methods used for this surgery. A way to improve epilepsy surgery is to construct patient-specific computational models that can help predict the outcome of surgery. In recent years, the notion has emerged that epilepsy must be seen as a network disorder rather than a localized disorder. Hence, the constructed computational model should include the connections between different areas of the brain.

During the workup to surgery, Single Pulse Electrical Stimulation (SPES) can be used to monitor connectivity in the brain. During SPES, monophasic electrical pulses (0.2 Hz, 1 ms, 4-8 mA) are applied to electrodes placed on the brain. These pulses can evoke responses in other areas of the brain. Early responses to the stimulations (ERs, $<$100 ms) can be linked to connectivity of the brain. Delayed responses (DRs, $>$100 ms) are seen as biomarkers of the epileptogenic cortex. In literature it has been shown that it is possible to simulate both the early and delayed responses to SPES in a network of just two neural mass models using feedforward inhibition. This study showed that disinhibition led to DRs, but did not consider reciprocal connections nor larger networks.

In this thesis, we first investigate the influence of feedforward inhibition on spontaneous activity in a network of two reciprocally coupled neural mass models through simulations and a bifurcation analysis. We show that feedforward inhibition has a significant effect on the spontaneous activity of coupled neural mass models and the generation of activity associated with epilepsy. Moreover, a key step in developing a patient-specific neural mass model is to reproduce the patients' ERs and DRs through stimulation within the model. Hence, we want to understand better how stimulation-induced activity propagates through the network. In this thesis we investigate evoked responses in small networks through simulations to find the influence of specific parameters on evoked activity. We use an evolutionary algorithm to fit parameters for networks of 12 nodes. The results show that

it is possible to fit desired ERs and part of the desired DRs in small networks of neural mass models. Moreover, optimizing parameters shows that most desired ERs and some desired DRs can be fitted in patient-specific networks based on clinical data collected at the University Medical Centre Utrecht. These models may later be used to study the onset and propagation of seizures, and possibly assist in delineating epileptiform tissue, thus improving epilepsy surgery.

Acknowledgements

This thesis concludes a little more than five years as a student at the University of Twente. Working on this thesis was not always easy, and I couldn't have done it without the help and support of several people.

First, I would like to thank dr. Hil Meijer for his supervision throughout this project. Thank you for our weekly meetings and always making time for me. I have greatly appreciated your insight and advice (sometimes also about things not directly related to the thesis). I would also like to thank the other members of my graduation committee, Prof. dr. Christoph Brune and dr. Valente Ramírez. I would especially like to thank Valente for always being enthusiastic and taking the time to give detailed feedback on my writing.

I would like to thank the epilepsy research group at the University Medical Centre Utrecht for welcoming me in their group. I especially want to thank Geertjan Huiskamp, once more for his supervision during my internship but also for inviting me to the UMCU and giving me a tour during the IEMU.

Annemarie, Femke, Jarco, Jente, Leander, Lotte, Nienke, Sven, Tessa and Wisse, thank you for all of the good times during these past five years. I really couldn't wish for a better group of friends. Finally, I would like to thank my brother and my parents. Thank you for always being there for me and supporting me.

Contents

Chapter 1

Introduction

Epilepsy is a common neurological disorder affecting around 0.4-1% of the world's population [1]. When treatment using drugs is not viable, removal of the epileptogenic zone (EZ) through surgery is an option. The epileptogenic zone is defined as the smallest part of the cortex the removal of which results in the patient being seizure free. This type of surgery currently has a 40-80% success rate [2]. In order to better delineate the epileptogenic cortex, it is important to consider the connectivity and activity of the brain. Analysis of this activity has lead to the view that epilepsy can be seen as a network disorder, rather than a localized disorder [3].

During the workup for surgery, electrocorticography (ECoG) is used to monitor activity of the brain. In this measurement method, small electrodes are placed directly on the brain for recording electrical signals. Single pulse electrical stimulation (SPES) is used during an ECoG monitoring period, which reveals effective connectivity between areas of the brain [4]. In SPES, a stimulation is applied to pairs of adjacent electrodes and responses are measured in all other electrodes. The stimulation mainly evokes two types of responses: early responses (ER) and delayed responses (DR) [5]. Early responses are responses found within 100 ms after applying a pulse, whereas delayed responses are found between 100 ms and 1 s after applying a pulse [5], [6]. The occurrence of ERs can be linked directly to the connectivity of the brain [7], [8]. On the other hand, DRs are biomarkers of the epileptogenic cortex, meaning that the occurrence of DRs signifies that a part of the brain may belong to the epileptogenic zone [9]. We note that DRs occur only stochastically.

In early responses, three peaks are commonly found: the N1, P1 and N2 peaks [6], [10]. The N1 peak is a large negative peak in the EEG signal shortly after the stimulation, the P1 peak is a subsequent positive peak and the N2 peak is a second negative peak that does not appear in every ER. Delayed responses are often seen as a spike and sharp wave occurring later after stimulation [5], [11]. Examples of ERs and DRs from clinical data are shown in Figure 1.1.

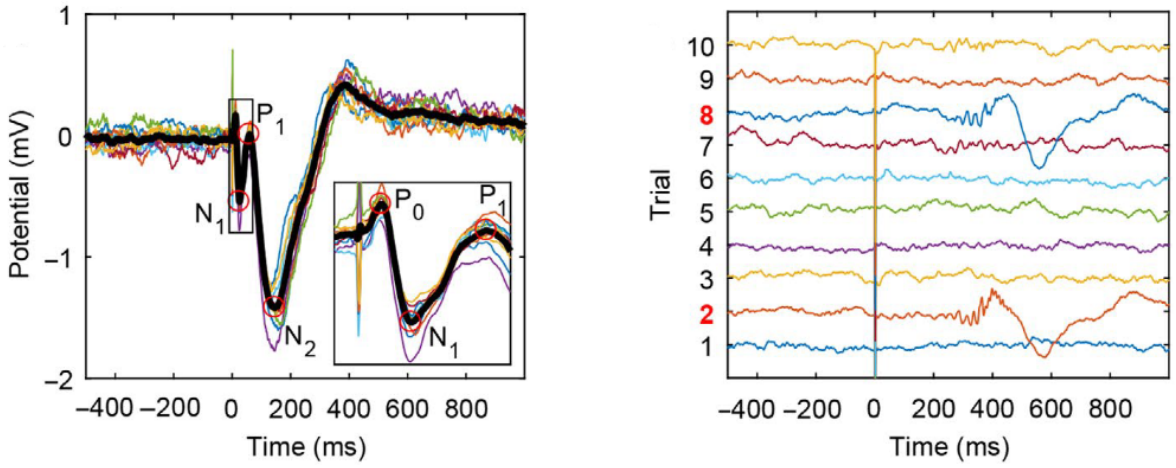

(a) Early response, averaged over 10 stimulations. The coloured lines indicate results from individual stimulations, whereas the black line gives the average signal over 10 stimulations.

(b) Delayed responses. Ten stimulations are shown on the vertical axis, and stimulations 2 and 8 yield a DR.

Figure 1.1: Early and delayed responses in clinical data, adapted from [6].

Simulating ECoG signals by modelling individual neurons is not feasible due to the extremely large amount of neurons in the brain. Therefore, it is practical to consider a model for the average activity within a region of the brain, specifically a model of the activity at a single electrode. In columns of neurons perpendicular to the surface of the brain, the firing of neurons is seen to synchronize [12]. Due to this synchronization, it is sufficient to model the average activity of populations of neurons in such a cortical column, as this average activity is what most affects the measured ECoG signal. Neural mass models (NMMs) are models describing the average activity of a neuronal population within a cortical column.

In this thesis we consider the Jansen-Rit and Wendling neural mass models [13], [14]. Both the Jansen-Rit model and the Wendling model describe the activity of several populations of neurons within a single cortical column. The Jansen-Rit model consists of three neuronal populations: pyramidal cells and excitatory and inhibitory inter-neurons. Each of these populations can be modelled using a second-order ordinary differential equation (ODE). The Wendling model consists of four populations, as the inhibitory inter-neurons are split into a slow inhibitory population and a fast inhibitory population. To model connected areas of the brain, neural mass models can be coupled in several ways. In their original paper, Jansen and Rit propose a model in which the activity of the pyramidal cells of one neural mass is projected onto the excitatory inter-neurons of the other neural mass [13]. However, the activity of one neural mass may also have an effect on the activity of the inhibitory inter-neurons in another region of the brain. In literature, the importance of such

feedforward inhibitory connections within the Wendling model was highlighted as it allowed the simulation of ER and DR-like responses within two feedforward coupled neural mass models [6]. Eissa et al. show that an amount of feedforward inhibition within a certain range on a macroscopic scale leads to the appearance of epileptic behaviour [15].

While it is known that feedforward inhibition is important for simulating activity evoked by stimulation, such as ERs and DRs, it is not known what the influence of feedforward inhibition is on the spontaneous activity of neural mass models. By spontaneous activity, we mean the activity of the model in absence of stimulation. Moreover, it is interesting to investigate whether stimulation evoked activity, specifically ERs and DRs, can be modelled in networks of neural mass models. The reproduction of these early and delayed responses in a model is an important step in developing patient-specific neural mass models that may eventually improve epilepsy surgery.

We now formulate our two main research questions. First, what is the influence of feedforward inhibition on the spontaneous activity of two reciprocally coupled neural mass models? As a follow-up question, how does evoked activity propagate in networks of neural mass models?

The thesis is organised as follows. We first introduce the Jansen-Rit and Wendling neural mass models. Moreover, we present models for coupled Jansen-Rit and Wendling models with feedforward inhibition.

In the first part of our results, we investigate the influence of feedforward inhibition on spontaneous activity. We analyse two reciprocally coupled neural mass models, where both nodes are modelled using the Jansen-Rit or Wendling model. We assess the influence of feedforward inhibition on this model through bifurcation analysis. Specifically, we characterize the bifurcations underlying the appearance and disappearance of spike-wave discharges (SWDs). Spike-wave discharges are large amplitude oscillations in the (simulated) ECoG signal that are associated with certain types of epilepsy [16]–[18].

In the second part of our results, we assess the influence of feedforward inhibition on evoked activity. We investigate the propagation of stimulation-evoked activity within small networks of Wendling neural mass models using simulations. We then fit parameters in artificial 12-node networks to show desired ERs an DRs. Parameter optimization is done using an evolutionary algorithm. Finally, we consider the performance of our optimization on clinical data provided by the University Medical Centre Utrecht.

Chapter 2

Neural mass models

We first describe the models used in this thesis. We explain the Jansen-Rit model, Wendling model and the coupling used between neural masses in the case that multiple linked neural masses are considered [13], [14]. Both the Jansen-Rit and Wendling models are neural mass models that model the activity of several neuronal populations within a cortical column. The Jansen-Rit model is based on one of the first neural mass models, as introduced by Lopes da Silva et al. in [19]. The Wendling model is an extension of the Jansen-Rit model. Both neural mass models can be used to approximate electroencephalography (EEG) measurements or intracranial EEG (ECoG) measurements.

2.1 The Jansen-Rit model

In this section, we describe the Jansen-Rit model [13]. We first review the model and then describe the dynamics and activity types found in the model.

2.1.1 Description of the Jansen-Rit model

The Jansen-Rit model describes the neuronal activity within a cortical column [13]. The model contains a pyramidal population which receives both excitatory and inhibitory feedback from populations of inter-neurons. Each population receives an average firing rate as input, comprised of input from other populations and in some cases external input. This firing rate is transformed to a postsynaptic potential (PSP) using a transformation with impulse response

$$h(t) = \begin{cases} Kkte^{-kt}, & t \geq 0, \\ 0, & t < 0. \end{cases} \tag{2.1}$$

Summing all incoming PSPs yields the membrane potential for a population. Here, K and k are constants which depend on whether the population is excitatory or inhibitory. The constant K denotes the synaptic gain or maximum amplitude of the postsynaptic potential, whereas $1/k$ is the time constant for the post-synaptic potential. It is assumed

that the constants K and k are the same for the excitatory inter-neurons and the pyramidal neurons, as they both have excitatory synapses. These constants are denoted as A and a respectively. Similarly, we denote the values for K and k for the inhibitory inter-neurons by B and b respectively. The impulse response described in equation 2.1 corresponds to the following second-order ordinary differential equation (ODE), which describes the dynamics of the postsynaptic potential for a neuronal population:

$$\ddot{v}(t) = -2k\dot{v}(t) - k^2 v(t) + Kkx(t). \tag{2.2}$$

Here, $x(t)$ denotes the incoming firing rate. Meanwhile $v(t)$ denotes the projected post-synaptic potential by the considered population. Rewriting equation 2.2 introducing an auxiliary state variable $z = \dot{v}$ we obtain:

$$\begin{cases} \dot{v} = z, \\ \dot{z} = Kkx - 2kz - k^2 v. \end{cases}$$

A sigmoid function is used to transform the membrane potential for a population into a mean firing rate of the neurons in this population. This sigmoid function is given by

$$\sigma(v) = \frac{2e_0}{1 + e^{r(v_h - v)}}.$$

Here, e_0 denotes half the maximum firing rate for a neuronal population, v_h is the potential for which half the maximum firing rate is achieved and r is the slope of the sigmoid function at v_h [20]. The following system of six coupled first-order nonlinear ODEs comprise the Jansen-Rit model:

$$\begin{cases} \dot{v}_0 = z_0, \\ \dot{z}_0 = Aa\sigma(v_1 - v_2) - 2az_0 - a^2 v_0, \\ \dot{v}_1 = z_1, \\ \dot{z}_1 = Aa\left(I + C_2\sigma(C_1 v_0)\right) - 2az_1 - a^2 v_1, \\ \dot{v}_2 = z_2, \\ \dot{z}_2 = BbC_4\sigma(C_3 v_0) - 2bz_2 - b^2 v_2. \end{cases} \tag{2.3}$$

In this system, the state variables v_i denote the postsynaptic potentials of the three neuronal populations, and z_i are auxiliary state variables. A schematic view of the interaction between the three populations is given in Figure 2.1. Moreover, the constants C_1, C_2, C_3 and C_4 are used to account for the connectivity (the amount of synapses) between populations of neurons and $I(t)$ denotes an external input firing rate. Within our analysis, this external firing rate is generally taken to be constant.

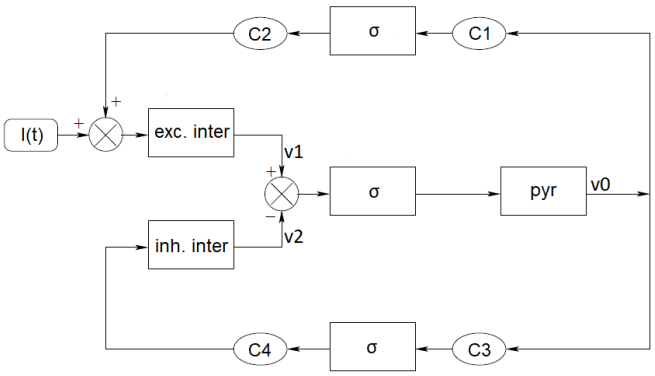

Figure 2.1: A schematic view of the Jansen-Rit neural mass model. Adapted from Grimbert et al. [20].

Values for the parameters as used by Grimbert et al. are given in Table 2.1 [20]. Parameter choices for the Jansen-Rit model are not set in stone. A list of admissible parameter ranges based on experiments and theoretically considered ranges for the Wendling model, an extension of the Jansen-Rit model, is given in the work by Ferrat et al. [21]. The parameters C_1, C_2, C_3 and C_4 will vary as they are based on the connectivity between neuronal populations. However, in general the constants will follow the relations $C_1 = C$, $C_2 = 0.8C$, $C_3 = 0.25C$ and $C_4 = 0.25C$ [13]. In this way, only one connectivity constant C needs to be varied when analyzing the system. Lastly, we note that the signal obtained from EEG or ECoG measurements can be approximated by the membrane potential or input for the pyramidal neurons and is thus given by $v_1 - v_2$. Hence, the quantity $v_1 - v_2$ is of particular interest when analysing the Jansen-Rit model.

Table 2.1: Parameter values for the Jansen-Rit model as described in the work by Grimbert et al. [20].

Parameter	Interpretation	Value
A	Synaptic gain for the pyramidal and excitatory populations	3.25
a	Reciprocal of the time scale for the pyramidal and excitatory populations	100
B	Synaptic gain for the inhibitory population	22
b	Reciprocal of the time scale for the inhibitory population	50
C	Connectivity constant	135
v_0	Potential for which the sigmoid function has its median value	6
e_0	Half the difference between $\max_v(\sigma(v))$ and $\min_v(\sigma(v))$	2.5
r	Slope of sigmoid function	0.56

2.1.2 Dynamics of the Jansen-Rit model

In this section, we review the bifurcations present in a Jansen-Rit neural mass model as described in [20]. For a minimal review of bifurcation theory we refer to Appendix A. To locate the bifurcations in an uncoupled Jansen-Rit neural mass we first find the equilibria of the system. At an equilibrium point we have

$$\begin{cases} v_0 = \frac{A}{a}\sigma(v_1 - v_2), \\ z_0 = 0, \\ v_1 = \frac{A}{a}(I + C_2\sigma(C_1 v_0)), \\ z_1 = 0, \\ v_2 = \frac{B}{b}C_4\sigma(C_3 v_0), \\ z_2 = 0. \end{cases}$$

The equilibria of the Jansen-Rit system can then be expressed as

$$\left(\frac{A}{a}\sigma(v_1 - v_2), 0, \frac{A}{a}\left(I + C_2\sigma\left(\frac{A}{a}\sigma(v_1 - v_2)\right)\right), 0, \frac{B}{b}C_4\sigma\left(C_3\frac{A}{a}\sigma(v_1 - v_2)\right), 0\right)$$

where $v_1 - v_2$ satisfies

$$v_1 - v_2 = \frac{A}{a}I + \frac{A}{a}C_2\sigma\left(\frac{A}{a}C_1\sigma(v_1 - v_2)\right) - \frac{B}{b}C_4\sigma\left(\frac{A}{a}C_3\sigma(v_1 - v_2)\right).$$

Using MATCONT [22] the found equilibrium points and found cycles may be continued letting I be a free parameter. Other parameter choices are taken as in Table 2.1. This yields the one-parameter bifurcation diagram as seen in Figure 2.2.

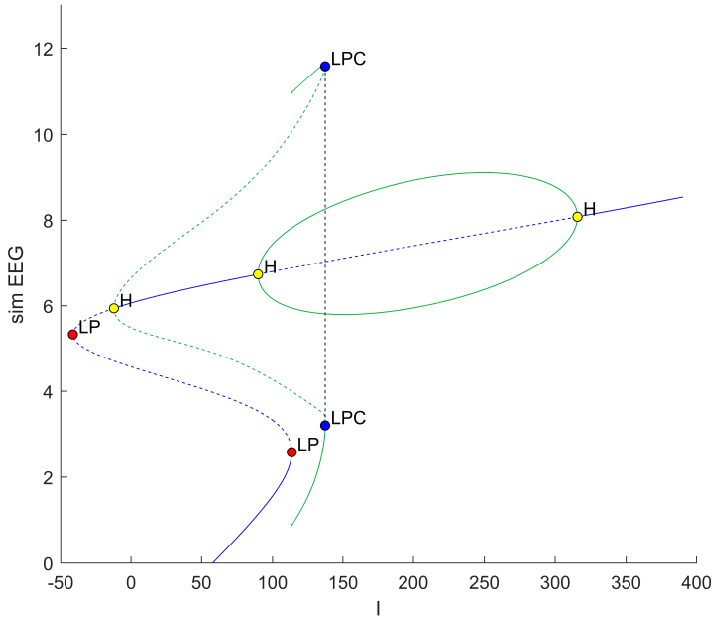

Figure 2.2: 1-parameter bifurcation diagram for the Jansen-Rit system as found by Grimbert et al. [20].

Here, the positions of equilibria are plotted in blue, where a dashed blue line denotes an unstable equilibrium and a solid line denotes a stable equilibrium. In the bifurcation diagram, we see that there is a region where two equilibria are stable for $-12.147498 \leq I \leq 89.829108$. We will refer to the equilibrium with the lowest value for $v_1 - v_2$ by the lower stable equilibrium. Similarly, we refer to the other stable equilibrium by the higher stable equilibrium, also for $I > 315$. We see that two fold (LP) points and three Hopf (H) points are found. The fold points are located at

$$I_{LP_1} \approx 113.586,$$
$$I_{LP_2} \approx -41.301.$$

We thus find that between these two parameter values three equilibria exist, whereas outside of this region only one equilibrium exists. The Hopf points are found at

$$I_{H_1} \approx -12.147,$$
$$I_{H_2} \approx 89.829,$$
$$I_{H_3} \approx 315.696.$$

The maximum and minimum values for the simulated ECoG of the cycles resulting from these Hopf bifurcations are plotted in green in Figure 2.2. For an unstable cycle, the green line is dashed and for a stable cycle the green line is solid. From the Hopf point at I_{H_1} an

unstable cycle is born (subcritical Hopf bifurcation), which turns into a stable cycle after the limit point of cycles point found at

$$I_{LPC} \approx 137.379.$$

This cycle cannot be continued further near $I \approx 113.586$. The period of the limit cycle increases rapidly near this value for I, as the branch terminates on a homoclinic bifurcation.

The cycle originating from the second Hopf point at I_{H_2} is stable (supercritical Hopf bifurcation) and this cycle exists up until the third Hopf point at I_{H_3} where it disappears.

2.1.3 Activity types in the Jansen-Rit model

We now show various activity types that the Jansen-Rit model can generate. We simulate the Jansen-Rit system using a simple forward Euler scheme with a time step of 1×10^{-4} s.

We follow the bifurcation diagram presented in Figure 2.2. We first simulate the system for $I = 50$ starting near the lower stable equilibrium which can be seen as the solid blue line on the bottom of the bifurcation diagram. In this case, we see that the simulated EEG signal $v_1(t) - v_2(t)$ seen in Figure 2.3a is constant as it converges to the lower equilibrium state. Starting near the higher equilibrium for $I = 60$ we again see that the system converges to an equilibrium state. The vertical axis is reversed to conform to standard methods of visualizing EEG measurements.

Simulating the system for $I = 135$ (Figure 2.3c) for certain initial conditions, we find spike-wave-discharges (SWD). Spike-wave-discharges are oscillations with high amplitude that are commonly associated with certain types of epilepsy [16]–[18]. This behaviour corresponds to the stable limit cycle with high amplitude found in the bifurcation diagram. Note that the scale used for the simulation shown in Figure 2.3c is very different from the other shown simulations.

Starting a simulation at $I = 200$ (Figure 2.3d) we see that the simulation shows an α-rhythm, which are oscillations with a frequency of $7 - 13$ Hz commonly seen during wakefulness [23]. The oscillations shown here correspond to the stable cycle between I_{H_2} and I_{H_3}. Lastly, we see that starting close to the present stable equilibrium at $I = 350$ (2.3e) the simulation is again seen to converge to an equilibrium state.

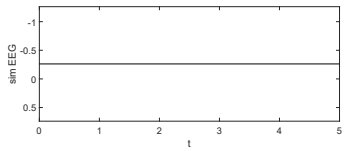

(a) Simulation for $I = 50$.

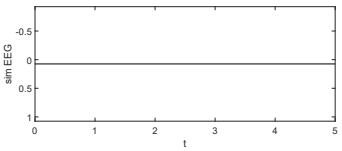

(b) Simulation for $I = 60$.

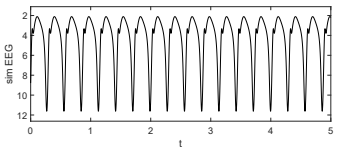

(c) Simulation for $I = 135$.

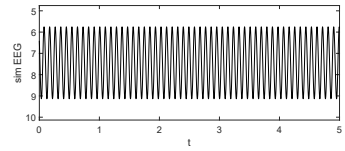

(d) Simulation for $I = 200$.

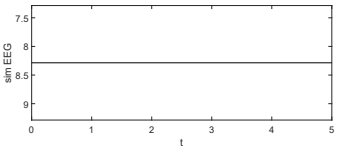

(e) Simulation for $I = 350$.

Figure 2.3: Simulations of the Jansen-Rit system for various values of I.

2.2 The Wendling model

The Wendling model is an extension of the Jansen-Rit model and distinguishes a fast inhibitory population and a slow inhibitory population [14]. The added fast inhibitiory population is modelled in the same way as the neuronal populations considered in the Jansen-Rit model. The constants K and k as seen in Equation 2.2 are adjusted for the new population. The addition of a fast inhibitory population allows for richer spontaneous activity [24]. Moreover, the interaction between fast and slow inhibitory populations is essential for modelling early and delayed responses in single pulse electrical stimulation (SPES) [6].

2.2.1 Description of the Wendling model

The original system of ten ODEs proposed by Wendling et al. can be reduced to an equivalent system of eight ODEs [25]. Similar to the Jansen-Rit model, this model includes a population of excitatory neurons, a population of pyramidal neurons and a population of slow inhibitory inter-neurons. Moreover, a population of fast inhibitory inter-neurons is added. This population is modelled analogously to the ODEs derived for the Jansen-Rit model, with synaptic gain G and time scale g. The fast inhibitory population receives input from both the pyramidal population as well as from the slow inhibitory population. The Wendling model for a single cortical column is then given by:

$$\begin{cases} \dot{v_0} = z_0, \\ \dot{z_0} = Aa\sigma(u_{\text{py}}) - 2az_0 - a^2 v_0, \\ \dot{v_1} = z_1, \\ \dot{z_1} = Aa(I + C_2\sigma(u_{\text{ex}})) - 2az_1 - a^2 v_1, \\ \dot{v_2} = z_2, \\ \dot{z_2} = BbC_4\sigma(u_{\text{is}}) - 2bz_2 - b^2 z_2, \\ \dot{v_3} = z_3, \\ \dot{z_3} = GgC_7\sigma(u_{\text{if}}) - 2gz_3 - g^2 v_3. \end{cases}$$

The input firing rates for each population is given by

$$\begin{cases} u_{\text{py}} = v_1 - v_2 - v_3, \\ u_{\text{ex}} = C_1 v_0, \\ u_{\text{is}} = C_3 v_0, \\ u_{\text{if}} = C_5 v_0 - \frac{C_6}{C_4} v_2. \end{cases}$$

The sigmoid function $\sigma(v)$ is given by

$$\sigma(v) = \frac{2e_0}{1 + e^{r(v_0 - v)}}.$$

The EEG-signal can again be approximated by the membrane potential of the pyramidal population, given by the input to the pyramidal cells $u_{\text{py}} = v_1(t) - v_2(t) - v_3(t)$. The Wendling model can generate more neural rhythms than the Jansen-Rit model. In their original paper, Wendling et al. vary the parameters B and G to show six different activity types [14]. Moreover, poly-SWDs can be generated for certain parameter choices [24], [26]. Parameter choices for the model are given in Table 2.2. In our analysis of spontaneous activity, we mostly adhere to the standard parameter choices given by Wendling et al. [14].

We consider two choices for B and G. In the first case $B = 24, G = 10$ is used. For these parameter choices, the slow inhibitory population is dominant over the fast inhibitory population. On the other hand, choosing $B = 22, G = 8$, we consider a case where fast inhibition is more important to the behaviour of the system. We note that both parameter choices are close to the band where spike-wave-discharges are found by Wendling et al. [14]. Hence, as we vary parameters, we may expect the appearance of SWDs in the system.

Parameter	Interpretation	Value
A	Synaptic gain for excitatory and pyramidal populations	3.25
B	Synaptic gain for slow inhibitory population	24 **or** 22
G	Synaptic gain for fast inhibitory population	10 **or** 8
a	Reciprocal of time scale for excitatory and pyramidal populations	100
b	Reciprocal of time scale for slow inhibitory population	50
g	Reciprocal of time scale for fast inhibitory population	500
C	Connectivity constant	135
c_1	Relative connectivity of pyramidal to excitatory population	1
c_2	Relative connectivity of excitatory to pyramidal population	0.8
c_3	Relative connectivity of pyramidal to slow inhibitory population	0.25
c_4	Relative connectivity of slow inhibitory to pyramidal population	0.25
c_5	Relative connectivity of pyramidal to fast inhibitory population	0.3
c_6	Relative connectivity of slow inhibitory to fast inhibitory population	0.1
c_7	Relative connectivity of fast inhibitory to pyramidal population	0.8
e_0	Half the difference between $\max_v(\sigma(v))$ and $\min_v(\sigma(v))$	2.5
v_0	Potential for which the sigmoid function has its median value	6
r	Slope of sigmoid function	0.56

Table 2.2: Parameter values for Wendling's neural mass model with feedforward inhibition as given by Wendling et al. [14] (with B and G chosen differently).

2.2.2 Dynamics of the Wendling model

We now consider the dynamics of the Wendling system under both proposed parameter choices when varying the input firing rate I. We start with the case that $B = 24$, $G = 10$.

Dynamics for $B = 24, G = 10$

The 1-parameter bifurcation diagram for this case is given in Figure 2.4. The dynamics for this case are very similar to the dynamics found for the Jansen-Rit system. This can be attributed to the larger value of B, the synaptic gain for the slow inhibitory population. A subcritical Hopf bifurcation is found at

$$I_{H_1} \approx 8.550.$$

From this Hopf bifurcation an unstable limit cycle emerges. This limit cycle undergoes a limit point of cycles bifurcation at

$$I_{LPC} \approx 156.382,$$

after which it becomes stable. This stable limit cycle is associated with spike-wave-discharge-like activity and ends in a SNIC bifurcation close to

$$I_{SNIC} \approx 131.285.$$

A second Hopf point is found at

$$I_{H_2} \approx 129.799.$$

The stable cycle resulting from this subcritical Hopf bifurcation is associated with an α-rhythm and ceases to exist after

$$I_{H_3} \approx 437.716,$$

where a third subcritical Hopf point is detected. Lastly, two limit points are found. One is responsible for the SNIC bifurcation and its location is thus given by the location of the SNIC bifurcation. We find a second fold point at

$$I_{LP_1} \approx -11.872.$$

From the locations of the found bifurcations we infer that a cycle responsible for spike-wave-discharges is stable between $I \approx 131.285$ and $I \approx 156.382$ whereas a cycle responsible for an α-rhythm is stable between $I \approx 129.799$ and $I \approx 437.716$.

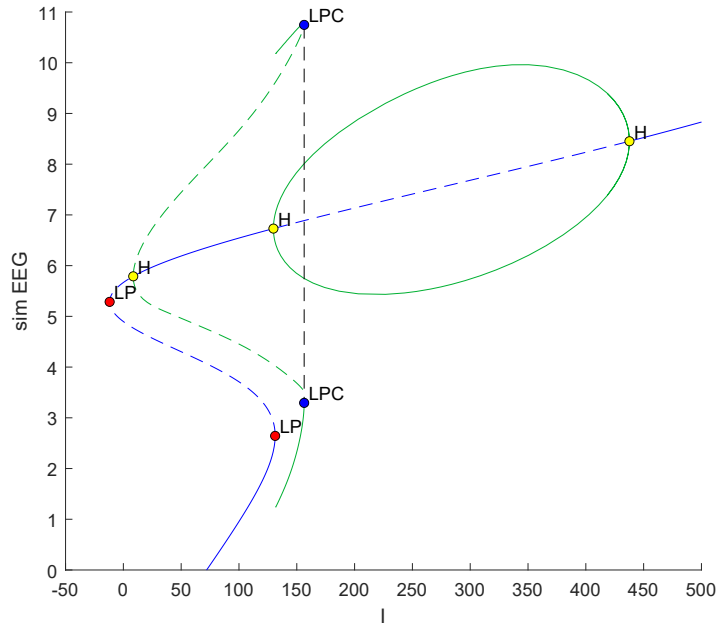

Figure 2.4: 1-parameter bifurcation diagram for the Wendling model setting $B = 24$ and $G = 10$.

Dynamics for $B = 22, G = 8$

The 1-parameter bifurcation diagram for this case is given in Figure 2.5. For these choices

of parameters two fold points are detected at

$$I_{LP_1} \approx 119.993,$$
$$I_{LP_2} \approx -34.624.$$

A subcritical Hopf point is detected at

$$I_H \approx -23.315.$$

For $I > I_H$ the equilibrium remains stable. The unstable limit cycle resulting from the Hopf bifurcation ends in a homoclinic-to-saddle bifurcation. For the parameter choices $B = 22, G = 8$ we see no stable cycles and the ECoG signal always converges to an equilibrium state.

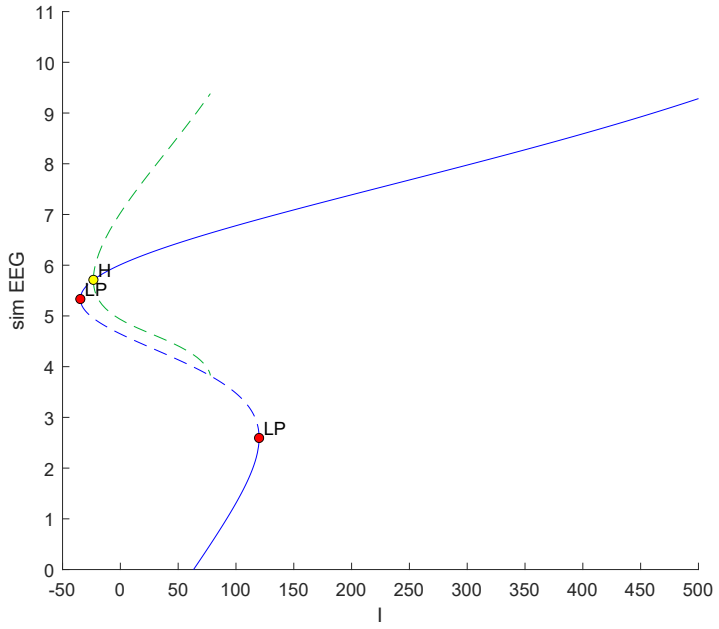

Figure 2.5: 1-parameter bifurcation diagram for the Wendling model setting $B = 22$ and $G = 8$.

2.3 Coupled neural mass models

To model different but connected areas of the brain, neural mass models can be coupled. When neural mass models are coupled, we propagate the firing rate of the pyramidal population of one neural mass to another neural mass. However, the effect of the activity of one neural mass is not immediately "felt" by another. Hence, the firing rate $f(t)$ of the pyramidal population is propagated using a distributed delay following a Gamma distribution

$h(t) = Kte^{-Kt}$, meaning that a convolution is taken between $f(t)$ and $h(t)$. The input firing rate $x(t)$ given to the other neural mass becomes

$$x(t) = \int_{-\infty}^{t} h(t-s)f(s)\mathrm{d}s.$$

We thus find

$$x'(t) = h(0)f(t) + \int_{-\infty}^{t} h'(t-s)f(s)\mathrm{d}s$$

Since $h(0) = 0$ and $h'(t) = Ke^{-Kt} - K^2te^{-Kt}$ we find that

$$\begin{aligned} x'(t) &= K\int_{-\infty}^{t} e^{-K(t-s)}f(s)\mathrm{d}s - KX(t) \\ \implies \frac{x''(t)}{K} + x'(t) &= f(t) - K\int_{-\infty}^{t} e^{-K(t-s)}f(s)\mathrm{d}s \\ \implies \frac{x''(t)}{K} + x'(t) &= f(t) - x'(t) - KX(t). \end{aligned}$$

We can therefore model $x(t)$ by the following system of two ODEs:

$$\begin{cases} x'(t) = z(t), \\ z'(t) = Kf(t) - 2z(t) - K^2x(t). \end{cases}$$

The state variable $x(t)$ can then be taken as additive external firing rate input for populations in a neural mass.

2.3.1 The coupled Jansen-Rit model

In the original paper by Jansen and Rit, a model for two coupled Jansen-Rit neural masses is given [13]. The model equations are:

$$\begin{cases} \dot{v}_{0j} = z_{0j}, \\ \dot{z}_{0j} = Aa\sigma(v_{1j} - v_{2j}) - 2az_{0j} - a^2v_{0j}, \\ \dot{v}_{1j} = z_{1j}, \\ \dot{z}_{1j} = Aa\left(u_j + C_2\sigma(C_1v_{0j}) + K^{i,j}v_{3i}\right) - 2az_{1j} - a^2v_{1j}, \\ \dot{v}_{2j} = z_{2j}, \\ \dot{z}_{2j} = BbC_4\sigma(C_3v_{0j}) - 2az_{2j} - a^2v_{2j}, \\ \dot{v}_{3j} = z_{3j}, \\ \dot{z}_{3j} = Ad\sigma(v_{1j} - v_{2j}) - 2dz_{2j} - d^2v_{2j}. \end{cases}$$

Here, $i \neq j$, $i, j \in \{1, 2\}$. The sigmoid function σ and the parameter values in this model are taken to be the same as in the Jansen-Rit model for a single cortical column. The

chosen parameter values can be found in Table 2.1. The final two equations correspond to the distributed delay for the outgoing firing rate to other neural masses. The parameter d is chosen to represent a different time scale for the signal propagated to other neural masses. We set $d = 33 \approx a/3$ according to the estimation made by Jansen and Rit [13].

The bifurcations present in this model have been studied extensively for three cases by Ahmadizadeh et al. [27]. The cases considered in their paper are

- Reciprocally coupled neural masses with symmetrical input ($u_1 = u_2$, $K^{1,2} = K^{2,1}$).
- Reciprocally coupled neural masses with a single input ($u_2 = 0$, $K^{1,2} = K^{2,1}$).
- Feedforward coupled neural masses with a single input ($u_2 = 0$ $K^{2,1} = 0$).

Ahmadizadeh et al. find rich dynamics for the considered cases, showing a larger range of possible behaviour for two coupled neural masses as opposed to a single Jansen-Rit neural mass. Their analysis gives insight in the generation of spike-wave discharges as a result of changes in another neural mass. As SWDs are associated with certain types of epilepsy, their analysis is thus interesting in the context of epilepsy research [16]–[18]. An analysis where I_1 and I_2 are fixed and $K^{1,2} = 650 - K$ and $K^{2,1} = K$ through Lyapunov exponents is performed for two coupled Jansen-Rit models in [28].

For our analysis of the influence of feedforward inhibition in reciprocally coupled neural mass models, we extend the coupled Jansen-Rit model and introduce a feedforward inhibition term. This gives the system of ODEs:

$$\begin{cases} \dot{v}_{0j} = z_{0j}, \\ \dot{z}_{0j} = Aa\sigma(v_{1j} - v_{2j}) - 2az_{0j} - a^2 v_{0j}, \\ \dot{v}_{1j} = z_{1j}, \\ \dot{z}_{1j} = Aa\left(I_j + C_2\sigma(C_1 v_{0j}) + K^{i,j} v_{3i}\right) - 2az_{1j} - a^2 v_{1j}, \\ \dot{v}_{2j} = z_{2j}, \\ \dot{z}_{2j} = Bb(C_4\sigma(C_3 v_{0j}) + K^{i,j}\beta v_{3i}) - 2az_{2j} - a^2 v_{2j}, \\ \dot{v}_{3j} = z_{3j}, \\ \dot{z}_{3j} = Ad\sigma(v_{1j} - v_{2j}) - 2dz_{3j} - d^2 v_{3j}. \end{cases} \tag{2.4}$$

Here, β is a scalar indicating what fraction of external input is projected onto the inhibitory population of interneurons.

2.3.2 The coupled Wendling-model

We now give a formulation for coupled Wendling neural masses with feedforward inhibition and feedforward excitation. We formulate the coupling between the neural masses in a way

analogous to how Jansen-Rit models are coupled. This results in the following system of $10N$ ODEs, where N is the amount of coupled Wendling models:

$$\begin{cases} \dot{v}_{0j} = z_{0j}, \\ \dot{z}_{0j} = Aa\sigma(u_{\mathsf{py}_j}) - 2az_{0j} - a^2 v_{0j}, \\ \dot{v}_{1j} = z_{1j}, \\ \dot{z}_{1j} = Aa(\sigma(u_{\mathsf{ex}_j}) + I_j + \sum_{i\neq j} K^{i,j} v_{4i}) - 2az_{1j} - a^2 v_{1j}, \\ \dot{v}_{2j} = z_{2j}, \\ \dot{z}_{2j} = Bb(\sigma(u_{\mathsf{is}_j}) + \beta \sum_{i\neq j} K^{i,j} v_{4i}) - 2bz_{2j} - b^2 v_{2j}, \\ \dot{v}_{3j} = z_{3j}, \\ \dot{z}_{3j} = Gg(\sigma(u_{\mathsf{if}_j}) + \gamma \sum_{i\neq j} K^{i,j} v_{4i}) - 2gz_{3j} - g^2 v_{3j}, \\ \dot{v}_{4j} = z_{4j}, \\ \dot{z}_{4j} = Ad\sigma(u_{\mathsf{py}_j}) - 2dz_{4j} - d^2 v_{4j}. \end{cases} \tag{2.5}$$

Here, $j \in \{1, ..., N\}$ and

$$\begin{cases} u_{\mathsf{py}_j} = v_{1j} - v_{2j} - v_{3j}, \\ u_{\mathsf{ex}_j} = C_1 v_{0j}, \\ u_{\mathsf{is}_j} = C_3 v_{0j}, \\ u_{\mathsf{if}_j} = C_5 v_{0j} - \frac{C_6}{C_4} v_{2j}. \end{cases}$$

The sigmoid function $\sigma(v)$ is given by

$$\sigma(v) = \frac{2e_0}{1 + e^{r(v_0 - v)}}.$$

The parameters $K^{i,j}$ denote the coupling strength between neural masses. We again set $d = 33 \approx a/3$ according to the estimations made by Jansen and Rit [13]. The scaling constants for the amount of external input propagated to the slow inhibitory populations and fast inhibitory populations are denoted by β and γ, respectively. Following parameter choices made by Hebbink et al. we will assume that $\gamma = 0.7\beta$ [6]. All other parameter choices remain as for the uncoupled Wendling neural mass and can be found in Table 2.2.

Chapter 3

The influence of feedforward inhibition on spontaneous activity of two reciprocally coupled neural masses

3.1 Introduction

In this chapter, we analyze the influence of feedforward inhibition on spontaneous activity of two reciprocally coupled neural mass models. Feedforward inhibition is known to be important in the context of computational models for epilepsy [6], [15]. However, the effect of feedforward inhibition on the spontaneous activity of coupled neural mass models is not known. A good understanding of this spontaneous activity would provide a link between modelling choices necessary for generating characteristic evoked responses and the appearance and disappearance of seizure-like activity.

In this chapter, we consider two weakly reciprocally coupled neural mass models representing two areas of the brain that are relatively far away from each other. We consider coupled Jansen-Rit models as well as coupled Wendling models. Our goal is to investigate whether feedforward inhibition has an effect on the appearance of seizure-like activity in the two neural mass models. In order to do this, we first view simulations of two coupled neural mass models. We then provide a bifurcation analysis of two coupled neural mass models to characterize the dynamics underlying the appearance and disappearance of SWD-like activity.

In literature, there are various works dealing with the analysis of coupled neural mass models, modelling connected areas of the brain [27]–[29]. Our analysis of coupled areas is similar to the work by Ahmadizadeh et al. in which two reciprocally coupled Jansen-Rit models are considered [27]. However, our analysis adds to the results in that paper in the following ways. First, we consider two coupled Jansen-Rit models with feedforward inhibition, as introduced in Equation 2.4. The role of feedforward inhibition has not been explored in [27]. For the case that no feedforward inhibition is present, we discuss parameter choices where both neural masses receive different but nonzero excitatory background input. We consider these parameter choices as in the context of modelling ECoG signals it is reasonable to assume that different areas of the brain receive nonzero background input from long-range connections. However, these background inputs can vary when considering different areas of the brain. The choice for separate but nonzero background inputs is different from the case considered in Ahmadizedah et al. where the goal is to model a hierarchy between two neural mass models by setting the excitatory background input to zero for one of the two neural masses [27]. Finally, we provide a bifurcation analysis of two coupled Wendling neural masses, which does not exist in literature to our knowledge.

3.2 Methods

We first consider two coupled Jansen-Rit models with feedforward inhibition as provided in Equation 2.4. For this model, we keep parameter choices as in Table 2.1. To quantify the influence of feedforward inhibition on the spontaneous activity of two reciprocally coupled Jansen-Rit neural masses, we vary the excitatory background inputs I_1 and I_2 as well as the amount of feedforward inhibition scaling β. These parameter variations are applied to a system of two weakly linked neural masses with $K^{1,2} = K^{2,1} = 25$. We will also provide some simulations where $K^{1,2}$ and $K^{2,1}$ are varied to investigate the influence of connectivity on spontaneous activity.

We first simulate the system to find where the two neural masses show spike-wave discharges, which are associated with certain types of epileptic activity [16]–[18]. We then provide a bifurcation analysis for various choices of β for $I_2 = 120$ and $I_2 = 150$, letting I_1 be a free parameter. A bifurcation diagram in the (I_1, β) plane is constructed for $I_2 = 150$. In this way, we gain an understanding of the bifurcations underlying the appearance and disappearance of SWD-like behaviour and also gain insight in other activity types present in two reciprocally coupled neural masses.

We then consider two coupled Wendling neural masses, given by Equation 2.5. Parameter choices are as in Table 2.2. We again vary I_1, I_2 and β, letting $\gamma = 0.7\beta$, and provide some simulations where $K^{1,2}$ and $K^{2,1}$ are varied. Similar to the case of two coupled Jansen-Rit models, we first simulate the system for various choices of I_2, varying I_1 and β. For our simulations, we look at the slow inhibition dominated case with weaker coupling ($K^{1,2} = K^{2,1} = 25$). For the fast inhibition dominated case, we consider a stronger coupling between neural masses ($K^{1,2} = K^{2,1} = 100$). A stronger coupling is taken as no SWD-like activity is found in the fast inhibition dominated case for $K^{1,2} = K^{2,1} = 25$. We then provide a bifurcation analysis for the fast inhibition dominated case with stronger coupling as the slow inhibition dominated case is similar to two coupled Jansen-Rit models. In our bifurcation analysis, we fix $I_2 = 250$ and $I_2 = 170$ and investigate the dynamics of the system for various choices of β, letting I_1 be a free parameter. Finally, a bifurcation diagram in the (I_1, β) plane is constructed for $I_2 = 250$.

For both the coupled Jansen-Rit and coupled Wendling models, simulations are done using ODE45, a standard solver in MATLAB. After a transient of 35 s, we measure the maximum and minimum EEG signal in a simulation of 5 s and thus find the amplitude of the signal for both neural masses. If the amplitude of the signal is higher than 8 mV within the considered 5 s, we classify the neural mass as spiking for the parameter values for which the system is simulated. In this way, whether a neural mass exhibits population spikes can be measured

in a grid. In this chapter, the term spike denotes periodic activity with high amplitude in the simulated ECoG signal, and is thus not related to spikes as seen in single neurons. For our bifurcation analysis, MATCONT is used for numerical continuation [22].

3.3 Results for two coupled Jansen-Rit models

We simulate two coupled Jansen-Rit neural masses to gain insight in the parameter ranges for which SWD-like spikes occur in the model. The results of simulations following the methods described in Section 3.2 can be seen in Figure 3.1. We note that simulations used for making Figure 3.1 are started from a random initial condition distributed according to a multivariate standard normal distribution. The results obtained are therefore also stochastic. Moreover, "spots" of different behaviour within a region are indicators of bistability.

We now briefly go over each of the diagrams shown in Figure 3.1. For $I_2 = 100$, a band of spiking behaviour observed for the first neural mass is observed for parameter ranges similar to the region where SWD-like activity can be observed in a single Jansen-Rit model. The band of spiking activity slightly moves to the right as the amount of feedforward inhibition scaling β increases.

For $I_2 = 110$, a small band of spiking activity for the second neural mass appears for very low values of β. For $I_2 = 120$ and $I_2 = 130$, we see that a large area of spiking behaviour for the second neural mass emerges. Moreover, a band exists for low values of β where simultaneous spiking is seen for both neural masses. For $I_2 = 130$ this band of simultaneous spiking behaviour is seen to extend to higher values of β.

For $I_2 = 150$ we see that spiking behaviour is only observed for the first neural mass for low values of β. As β increases a band of spiking behaviour for the second neural mass appears as well as a region where both neural masses show spiking behaviour. For high values of β, small regions where only one neural mass shows spiking behaviour appear next to the band of simultaneous spiking. Similar results can be seen for $I_2 = 170$ and $I_2 = 200$, where the band of spiking behaviour for the second neural mass appears for increasingly high values of β. When $I_2 = 300$, spiking is again only observed for the first neural mass in a small band.

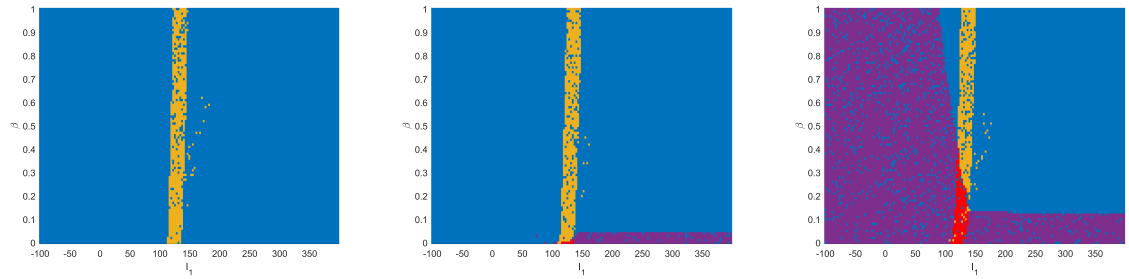

(a) Spiking behaviour for $I_2 = 100$. *(b)* Spiking behaviour for $I_2 = 110$. *(c)* Spiking behaviour for $I_2 = 120$.

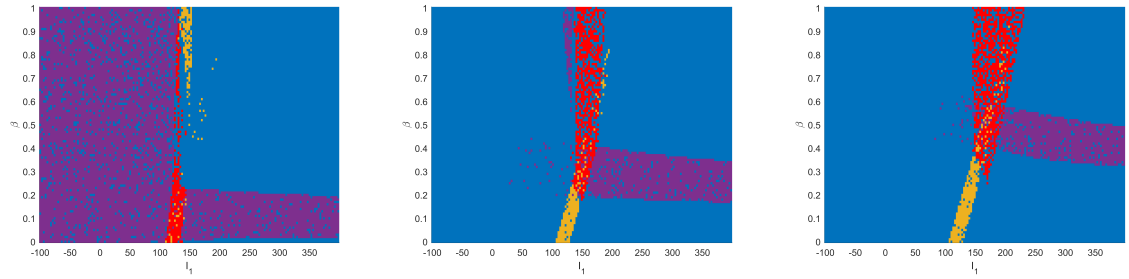

(d) Spiking behaviour for $I_2 = 130$. *(e)* Spiking behaviour for $I_2 = 150$. *(f)* Spiking behaviour for $I_2 = 170$.

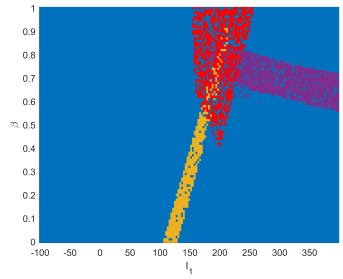

(g) Spiking behaviour for $I_2 = 200$.

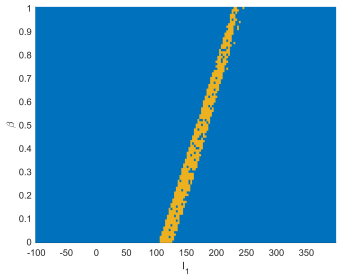

(h) Spiking behaviour for $I_2 = 300$.

Figure 3.1: Diagrams showing regions of spiking behaviour for both coupled neural masses. I_1 and β are varied, whereas I_2 is fixed. Here, **blue** means no neural mass is spiking, **yellow** means only neural mass 1 is spiking, **purple** means only neural mass 2 is spiking and **red** means both neural masses are spiking.

We provide similar simulations in order to investigate the influence of the connection strength on the activity of two neural mass models. For these simulations, we fix $I_2 = 150$ and $\beta = 0.35$ as this choice of parameters shows many different types of activity as shown in Figure 3.1e. We first fix $K^{2,1} = 25$ and vary the feedforward connection $K^{1,2}$. Then, we set $K^{1,2} = 25$ and vary $K^{2,1}$. The results are shown in Figure 3.2.

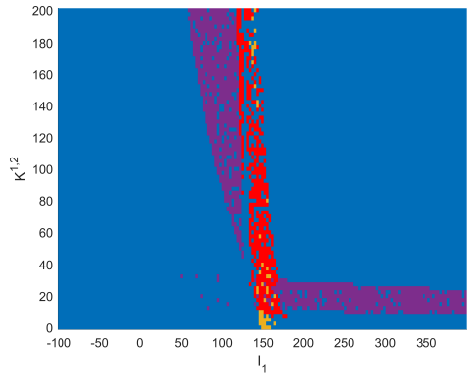

(a) Spiking behaviour for $K^{2,1} = 25$.

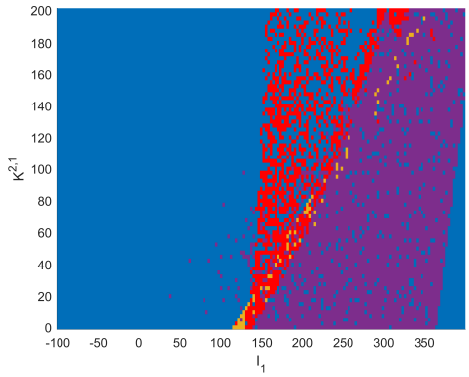

(b) Spiking behaviour for $K^{1,2} = 25$.

Figure 3.2: Diagrams showing regions of spiking behaviour for both coupled neural masses. I_2 and β are fixed. Here, **blue** means no neural mass is spiking, **yellow** means only neural mass 1 is spiking, **purple** means only neural mass 2 is spiking and **red** means both neural masses are spiking.

These simulations show that the connectivity has a large effect on the spontaneous activity of two reciprocally coupled Jansen-Rit neural mass models. Specifically, we have found that a stronger feedback connection promotes the appearance of simultaneous SWD-like activity in the two coupled neural mass models.

3.3.1 Bifurcation analysis for $\mathbf{I_2 = 120}$

In this section we present the results from bifurcation analysis for the case that $I_2 = 120$, for which the results of the simulations are shown in Figure 3.1c. The choice for $I_2 = 120$ is made because simulations in Figure 3.1 show that the system exhibits rich and representative behaviour for this choice of I_2. Through our bifurcation analysis, we show the dynamics underlying the appearance and disappearance of SWD-like activity as well as other activity types present in the two coupled Jansen-Rit neural masses. We consider the cases $\beta = 0$, $\beta = 0.3$ and $\beta = 0.7$.

Bifurcation analysis for $I_2 = 120$, $\beta = 0$

We first provide a bifurcation analysis for $I_2 = 120$ and $\beta = 0$. In this case, no feedforward inhibition is present. Bifurcation diagrams and several simulations are shown in Figure 3.3.

In Figures 3.3a and 3.3b, we see the full 1-parameter bifurcation diagram. In Figure 3.3a the amplitude of the simulated ECoG signal for the first neural mass is shown, and the amplitude of the simulated ECoG signal for the second neural mass is shown in Figure 3.3b. An equilibrium branch similar to the one seen for a single Jansen-Rit neural mass (Figure 2.2) is seen to remain for the first neural mass. However, this equilibrium branch is entirely

unstable. This can be attributed to oscillations of the second neural mass, which causes periodic forcing of the first neural mass. Two stable cycles exist for high values of I_1, both clearly seen in Figure 3.3. Simulations for these cycles are given in Figures 3.3o and 3.3p. These two cycles are responsible for the bistability between spiking activity and no spiking activity (α-rhythm) of the second neural mass as seen in Figure 3.1c. Both cycles become unstable after a Neimark-Sacker bifurcation, from which a stable torus-like attractors originate. Simulations for the two resulting tori are shown in Figures 3.3m and 3.3n. These tori remain stable along the region where only unstable cycles and equilibria are found in Figures 3.3a and 3.3b. One of the tori corresponds to an α-rhythm for both neural masses, whereas the other corresponds to spiking behaviour for the second neural mass and an α-rhythm for the first. Hence, the bistable behaviour as seen in Figure 3.1c is explained for the parameter range where these tori are stable. As shown in Figure 3.3c , the cycle showing α-rhythms for the second neural masses undergoes two LPC bifurcations. After a Hopf point, the cycle disappears. The cycle responsible for spiking behaviour of the second neural mass regains stability after another NS point, as is seen in Figure 3.3c (simulation shown in Figure 3.3j). After a third NS point shown in 3.3e near $I_1 = -20$, the cycle becomes unstable once more. After several fold of limit cycle bifurcations the cycle becomes stable again and remains stable for low values of I_1 (simulation shown in Figure 3.3i and 3.3k).

An unstable cycle emerges from a Hopf point near the two NS bifurcations found for high values of I_1. This cycle becomes stable after an NS bifurcation (most clearly seen in Figure 3.3c). The resulting stable cycle corresponds to an α-rhythm for both neural masses for higher values of I_1. As I_1 decreases, the amplitude of the oscillation in the first neural mass also decreases. A simulation for this cycle with small amplitude for the first neural mass is shown in Figure 3.3h. The cycle becomes unstable after a Neimark-Sacker bifurcation near $I_1 = -15$, after which it undergoes several fold of limit cycle bifurcations, shown in Figure 3.3e. After the last LPC bifurcation near $I_1 = 100$, the cycle becomes stable again and a simulation is shown in Figure 3.3h.

From a Hopf point near the first NS point from the left in Figure 3.3e, an unstable cycle emerges for which the shape is reminiscent of the cycle that caused SWD-like behaviour in a single Jansen-Rit neural mass. However, the cycle is completely unstable here. After undergoing several LPC bifurcations most clearly shown in Figures 3.3d and 3.3g, the cycle remains unstable and disappears after a homoclinic (SNIC) bifurcation. Instead, spiking behaviour for both neural masses is seen in the form of activity with higher period. An example of such activity is shown in Figure 3.3l. Cycles with higher period or torus-like attractors responsible for this activity could not be continued numerically.

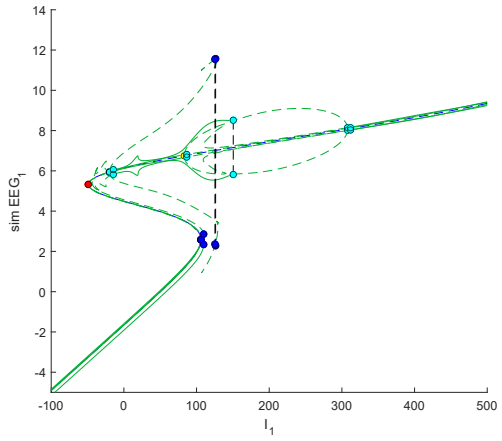

(a) 1-parameter bif. diagram represented in the ECoG signal for NM1.

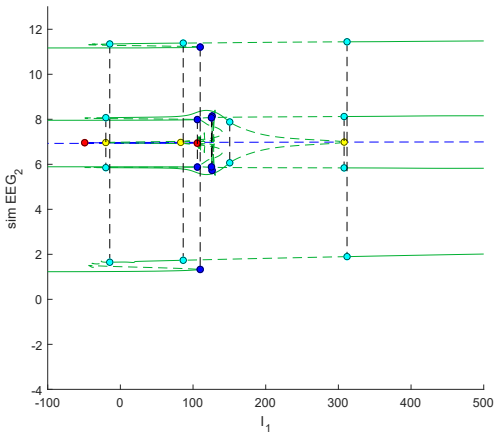

(b) 1-parameter bif. diagram represented in the ECoG signal for NM2.

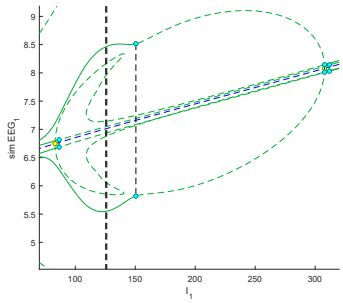

(c) Zoom-in 1.

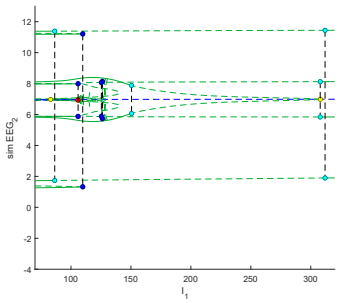

(d) Zoom-in 2.

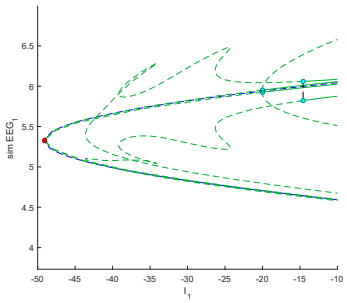

(e) Zoom-in 3.

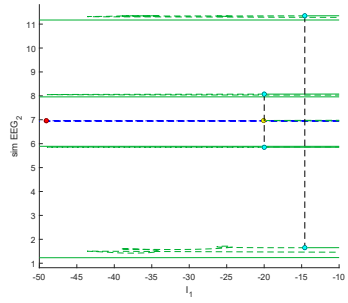

(f) Zoom-in 4.

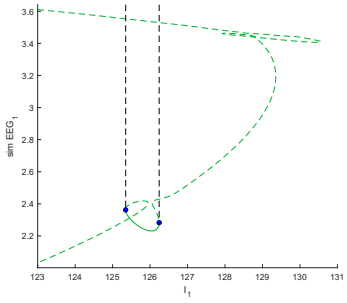

(g) Zoom-in 5.

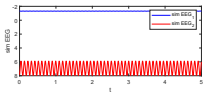

(h) $I_1 = 10.5$.

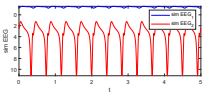

(i) $I_1 = 11$.

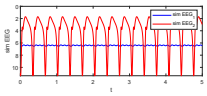

(j) $I_1 = 38$.

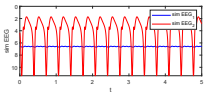

(k) $I_1 = 65$.

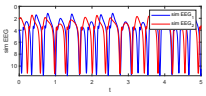

(l) $I_1 = 126$.

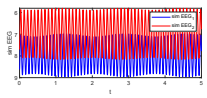

(m) $I_1 = 248$.

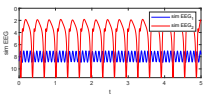

(n) $I_1 = 289$.

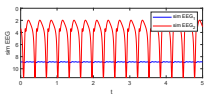

(o) $I_1 = 440$.

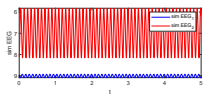

(p) $I_1 = 453$.

Figure 3.3: One-parameter bifurcation diagram and simulations for $I_2 = 120$, $\beta = 0$. In the bifurcation diagrams, **red** = LP, **yellow** = H, **blue** = LPC, **cyan** = NS, **magenta** = PD.

Bifurcation analysis for $I_2 = 120$, $\beta = 0.3$

We now move on to the case that $I_2 = 120$ and $\beta = 0.3$. We now find that there are two branches of equilibria, most clearly seen in Figure 3.4b. Both equilibria are stable for high values of I_1, and simulations are shown in Figure 3.4q and 3.4r. The higher equilibrium (in NM2) seems to show oscillatory behaviour when simulated. However, this behaviour is transient and the signal will eventually converge to the equilibrium state.

The activity of the system for higher values of I_1 is in many ways similar to the case that $\beta = 0$. Namely, we see an NS bifurcation corresponding to the appearance of desynchronized α-rhythms near $I_1 = 330$ (Figure 3.4p). Another stable cycle also exists for this parameter range (Figure 3.4o)

Spiking behaviour for the first neural mass can again be linked to the existence of a torus-like structure, a simulation of which is shown in Figure 3.4n. A stable cycle corresponding to SWD-like activity for the first neural mass also exists, as shown in Figures 3.4c and 3.4d between $I_1 \approx 126$ and $I_1 \approx 143$. This cycle becomes stable after an unstable cycle originating from the leftmost Hopf bifurcation in Figure 3.4g and 3.4h undergoes a fold of limit cycles. It becomes unstable again after another LPC point. A simulation of this cycle is shown in Figure 3.4l. Similar to the case that $\beta = 0$, the unstable cycle originating from the rightmost Hopf point in Figure 3.4g ends in a SNIC bifurcation as shown in Figures 3.4e and 3.4f. Simultaneous spiking is again seen as activity with a higher period, an example is shown in Figure 3.4k.

For low values of I_1, a stable cycle corresponding to SWD-like activity for the second neural mass persists. This cycle undergoes two period-doubling bifurcations before becoming unstable after a fold of limit cycles. A simulation is shown in Figure 3.4j and the bifurcations are most clearly shown in Figures 3.3b and 3.3d.

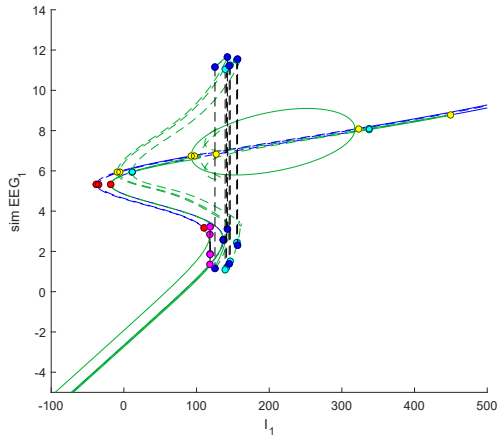

(a) 1-parameter bif. diagram represented in the ECoG signal for NM1.

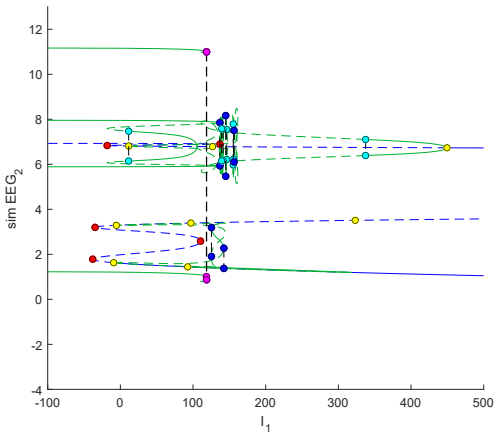

(b) 1-parameter bif. diagram represented in the ECoG signal for NM2.

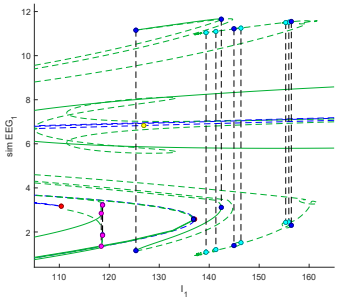

(c) Zoom-in 1.

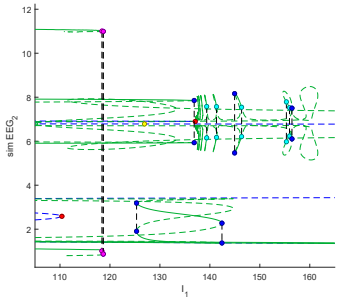

(d) Zoom-in 2.

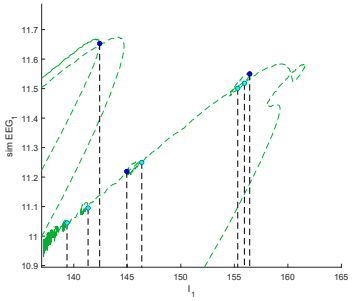

(e) Zoom-in 3.

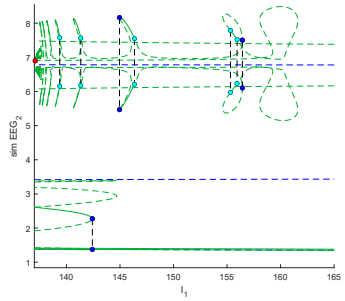

(f) Zoom-in 4.

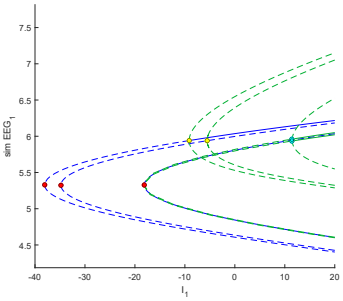

(g) Zoom-in 5.

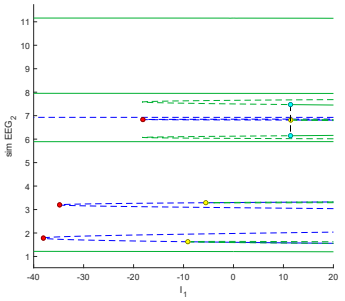

(h) Zoom-in 6.

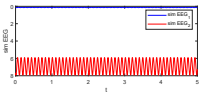

(i) $I_1 = 85$.

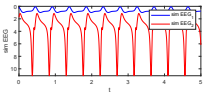

(j) $I_1 = 86$.

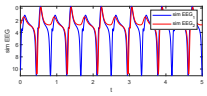

(k) $I_1 = 123$.

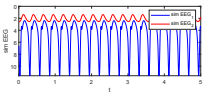

(l) $I_1 = 139$.

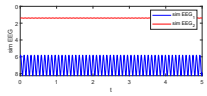

(m) $I_1 = 140$.

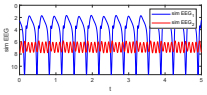

(n) $I_1 = 150$.

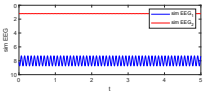

(o) $I_1 = 304$.

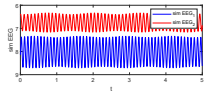

(p) $I_1 = 326$.

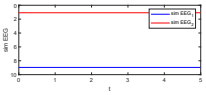

(q) $I_1 = 456$.

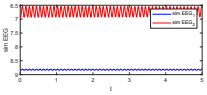

(r) $I_1 = 456.5$.

Figure 3.4: One-parameter bifurcation diagram and simulations for $I_2 = 120$, $\beta = 0.3$. In the bifurcation diagrams, **red** = LP, **yellow** = H, **blue** = LPC, **cyan** = NS, **magenta** = PD.

Bifurcation analysis for $I_2 = 120$, $\beta = 0.7$

Lastly, we look at the case that $I_2 = 120$ and $\beta = 0.7$. The two equilibrium branches seen in the previous diagram remain. Instead of activity governed by a torus-like structure, we now see that two stable cycles resulting from Hopf bifurcations (shown in Figure 3.5e, simulations in Figures 3.5l and 3.5m) result in an α-rhythm for the first neural mass and small oscillations for the second neural mass.

For SWD-like activity, we have found that an unstable cycle originating from the leftmost Hopf bifurcation in Figure 3.5a becomes stable after an LPC point. This results in SWD-like activity for the first neural mass (Figure 3.5j) and the cycle disappears after a homoclinic bifurcation. Another stable cycle exists for low values of I_1 that corresponds to spiking behaviour of only the second neural mass as shown in Figure 3.3b. This cycle also disappears after a homoclinic bifurcation. A simulation close to the homoclinic bifurcation point is shown in Figure 3.5i, while a simulation for a lower value of I_1 is shown in Figure 3.5g.

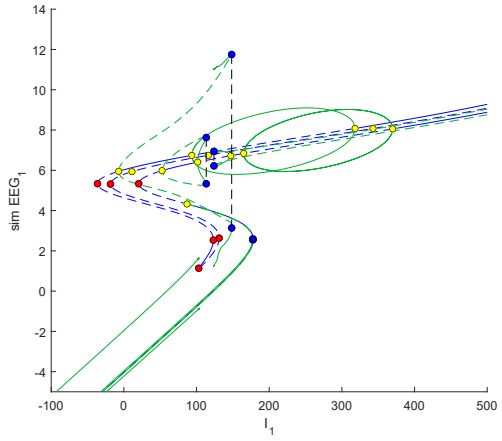

(a) 1-parameter bif. diagram represented in the ECoG signal for NM1.

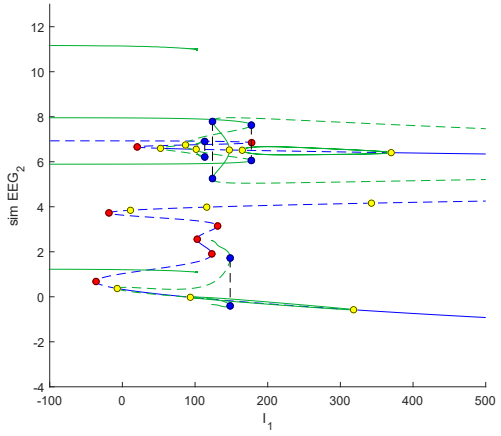

(b) 1-parameter bif. diagram represented in the ECoG signal for NM2.

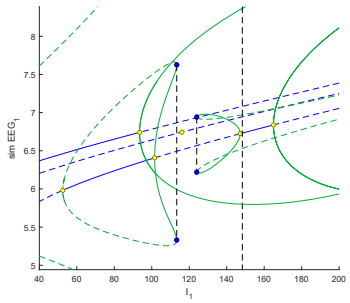

(c) Zoom-in 1.

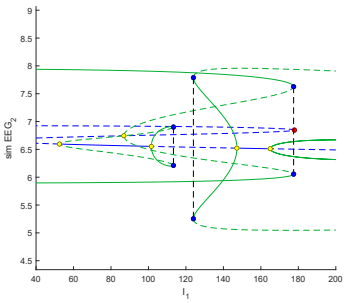

(d) Zoom-in 2.

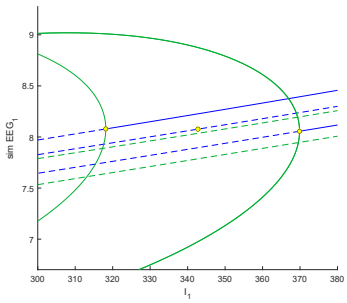

(e) Zoom-in 3.

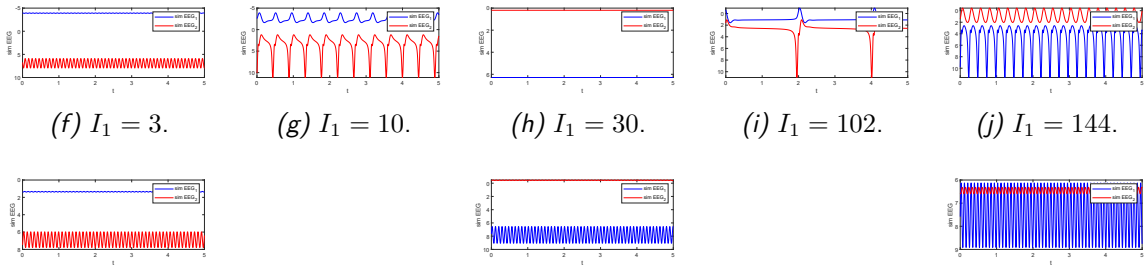

(f) $I_1 = 3$. *(g)* $I_1 = 10$. *(h)* $I_1 = 30$. *(i)* $I_1 = 102$. *(j)* $I_1 = 144$.

(k) $I_1 = 159.5$. *(l)* $I_1 = 265$. *(m)* $I_1 = 273$.

Figure 3.5: One-parameter bifurcation diagram and simulations for $I_2 = 120$, $\beta = 0.7$. In the bifurcation diagrams, **red** = LP, **yellow** = H, **blue** = LPC, **cyan** = NS, **magenta** = PD.

3.3.2 Bifurcation analysis for $\mathbf{I_2 = 150}$

We now provide several one-parameter bifurcation diagrams in order to better understand the activity seen in Figure 3.1e. We set $I_2 = 150$. This choice for I_2 was made from the considered values in Figure 3.1 because it shows rich and representative activity that is considerably different from the activity seen for $I_2 = 120$. Once again, we consider several values of β in order to get an understanding of the dynamics underlying switches in activity types within the two Jansen-Rit neural masses. We consider $\beta = 0, \beta = 0.2$ and $\beta = 0.8$. The choice $I_2 = 150$ corresponds to a second neural mass that without external input is expected to show an α-rhythm.

Bifurcation analysis for $I_2 = 150$, $\beta = 0$

We first consider a case where no feedforward inhibition is present. A single equilibrium branch exists that is unstable for all considered values of I_1. We see that for high values of I_1, a stable cycle exists corresponding to an α-rhythm for the second neural mass and small oscillations for the first neural mass (Figure 3.6b, simulation is shown in Figure 3.6k). This cycle becomes unstable after a Neimark-Sacker point. After this point, a torus-like structure is stable that corresponds to a desynchronized α-rhythm for both neural masses (Figure 3.6j). The unstable cycle becomes stable again after two LPC points, as shown in Figure 3.6d (and Figure 3.6c). The stable cycle corresponds to two α-rhythms with the same frequency for both neural masses (Figure 3.6i). The cycle briefly becomes unstable due to an NS point, before becoming stable again after another Neimark-Sacker bifurcation (bifurcations shown in Figure 3.6c). The resulting stable cycle corresponds to an α-rhythm for the second neural mass and periodic activity with small amplitude for the first neural mass (Figure 3.6g). This cycle remains stable up to an NS point. The cycle becomes stable for a final time after two LPC bifurcations (Figure 3.6b), and this cycle again corresponds

to an α-rhythm for the second neural mass and periodic activity with small amplitude for the first neural mass. A simulation is shown in Figure 3.6f.

Once again, an unstable cycle originating from a Hopf point ends in a homoclinic bifurcation after an LPC bifurcation (Figure 3.6e). A stable torus-like structure exists that shows SWD-like activity for the first neural mass and an α-rhythm for the second neural mass. A simulation for this torus is shown in Figure 3.6h.

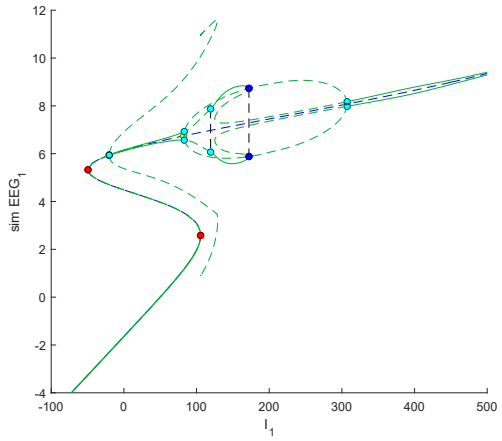

(a) 1-parameter bif. diagram represented in the ECoG signal for NM1.

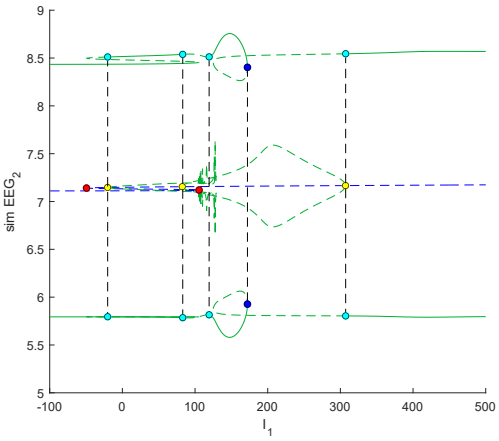

(b) 1-parameter bif. diagram represented in the ECoG signal for NM2.

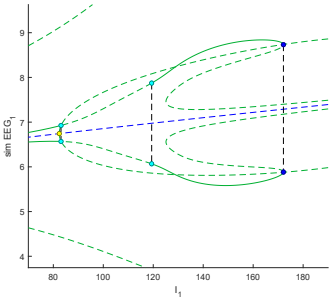

(c) Zoom-in 1.

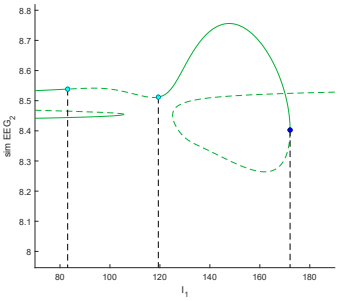

(d) Zoom-in 2.

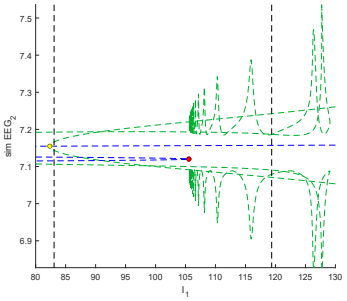

(e) Zoom-in 3.

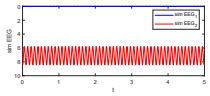

(f) $I_1 = 50$.

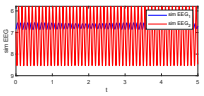

(g) $I_1 = 76.5$.

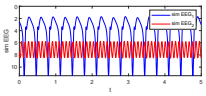

(h) $I_1 = 120$.

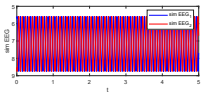

(i) $I_1 = 150$.

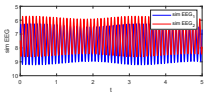

(j) $I_1 = 240$.

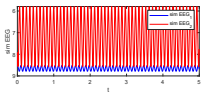

(k) $I_1 = 400$.

Figure 3.6: One-parameter bifurcation diagram and simulations for $I_2 = 150$, $\beta = 0$. In the bifurcation diagrams, **red** = LP, **yellow** = H, **blue** = LPC, **cyan** = NS, **magenta** = PD.

Bifurcation analysis for $I_2 = 150$, $\beta = 0.2$

Similarly, we provide the one-parameter bifurcation diagram for the case that $I_2 = 150$ and $\beta = 0.2$. For this choice of β, once again only one completely unstable equilibrium branch is present.

We see that two stable cycles are found for high values of I_1 (Figure 3.7b, simulations are shown in Figure 3.7p and 3.7q). The first stable cycle corresponds to spiking behaviour in the second neural mass, while the other corresponds to an α-rhythm in the second neural mass. Both cycles become unstable after the occurrence of a Neimark-Sacker bifurcation. The tori resulting from these bifurcations are stable and cause the bistability between spiking activity of the second neural mass and no spiking activity for the second neural mass in the band seen in Figure 3.1. Simulations for the two tori are shown in Figures 3.7n and 3.7o. The limit cycle responsible for the appearance of spiking activity in the second neural mass can be continued letting β be a free parameter. This reveals that the band seen in Figure 3.1 is bounded from below by a fold of limit cycles bifurcation, and bounded from above by a homoclinic bifurcation for high values of I_1. Continuations of these bifurcations are shown in the 2-parameter diagram in Section 3.3.3.

A cycle corresponding to simultaneous spiking behaviour is found and a simulation is shown in Figure 3.7j. Continuing this cycle reveals that there is an isolated branch of cycles responsible for this simultaneous SWD-like behaviour (Figure 3.7e and 3.7f). This cycle is stable between two LPC points. A torus-like structure responsible for spiking behaviour of the first neural mass also exists, as shown in Figure 3.7i. For low values of I_1, two stable cycles remain corresponding to an α-rhythm for the second neural mass and periodic activity with small amplitude for the first neural mass (simulations are shown in Figures 3.7g and 3.7h). Lastly, a stable cycle exists between two LPC bifurcations located approximately at $I_1 = 240$ and $I_1 = 300$ responsible for spiking behaviour of the second neural mass and an α-rhythm for the first neural mass (simulation shown in Figure 3.7m, bifurcations shown in Figures 3.7c and 3.7d).

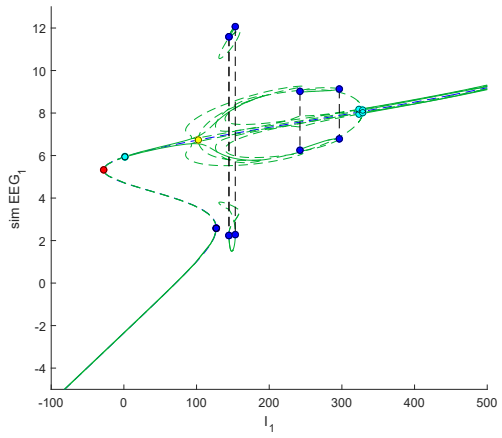

(a) 1-parameter bif. diagram represented in the ECoG signal for NM1.

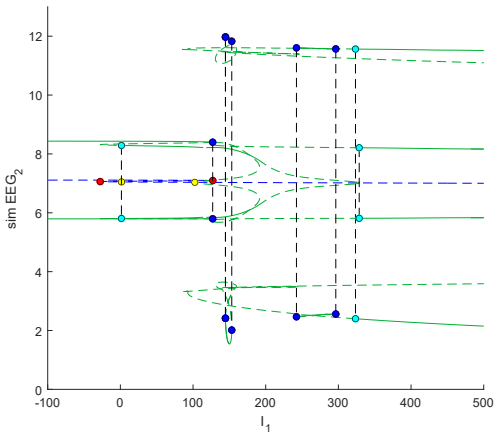

(b) 1-parameter bif. diagram represented in the ECoG signal for NM2.

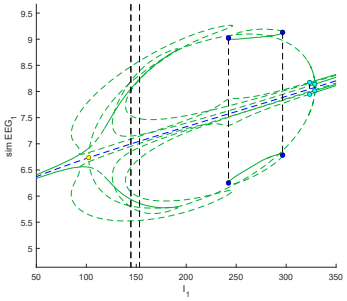

(c) Zoom-in 1.

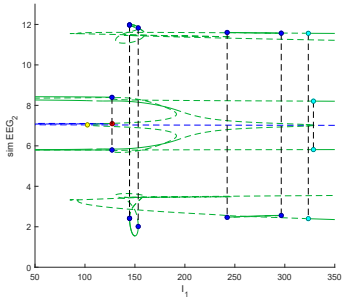

(d) Zoom-in 2.

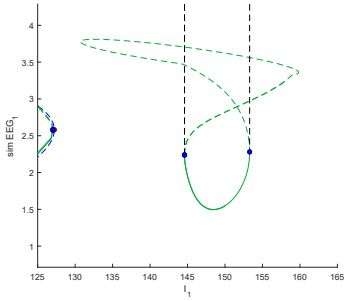

(e) Zoom-in 3.

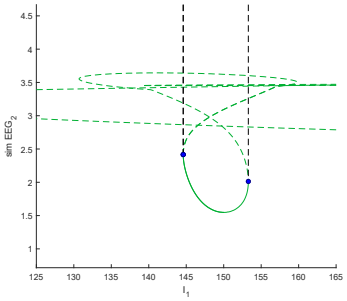

(f) Zoom-in 4.

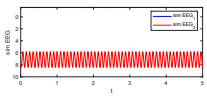

(g) $I_1 = 24$.

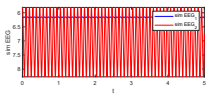

(h) $I_1 = 24.5$.

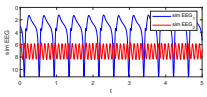

(i) $I_1 = 134$.

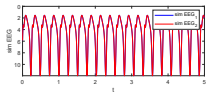

(j) $I_1 = 150$.

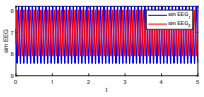

(k) $I_1 = 164$.

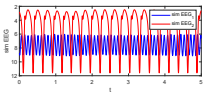

(l) $I_1 = 232$.

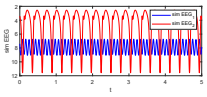

(m) $I_1 = 282$.

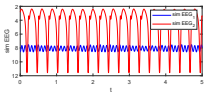

(n) $I_1 = 319.5$.

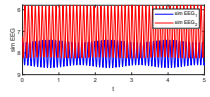

(o) $I_1 = 320$.

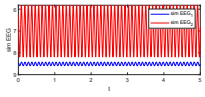

(p) $I_1 = 399$.

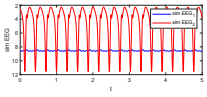

(q) $I_1 = 400$.

Figure 3.7: One-parameter bifurcation diagram and simulations for $I_2 = 150$, $\beta = 0.2$. In the bifurcation diagrams, **red** = LP, **yellow** = H, **blue** = LPC, **cyan** = NS, **magenta** = PD.

Bifurcation analysis for $I_2 = 150$, $\beta = 0.8$

Finally, we provide the one-parameter bifurcation diagram for the case that $\beta = 0.8$.

We see that two branches of equilibria exist for $\beta = 0.8$ (Figures 3.8a and 3.8b). For high values of I_1, the system will tend to one of two stable equilibria. We will call the equilibrium that has a higher simulated EEG signal in the second neural mass the upper branch equilibria and the other equilibrium the lower branch of equilibria. The higher branch of equilibria undergoes a Hopf bifurcation for $I_1 \approx 378.27$. From this supercritical Hopf bifurcation a stable cycle emerges corresponding to an α-rhythm for the first neural mass and smaller periodic activity for the second neural mass (Figure 3.8p). The cycle becomes unstable after a Neimark-Sacker bifurcation, from which a torus corresponding to desynchronized activity emerges (Figure 3.8n). A second supercritical Hopf bifurcation for the lower branch of equilibria at $I_1 \approx 319.58$ yields a stable cycle corresponding to an α-rhythm for the first neural mass and small periodic activity for the second neural mass (Figure 3.8o). This cycle ends in another Hopf bifurcation at $I_1 \approx 96.04$.

The small band of spiking activity for the first neural mass seen next to the region of synchronous spiking corresponds to a torus-like structure. A simulation is shown in Figure 3.8m. Synchronized spiking behaviour occurs when a cycle, originating from a homoclinic bifurcation, undergoes a period-doubling bifurcation after which it becomes stable (bifurcation shown in Figure 3.8e and 3.8f). After a second period-doubling bifurcation ($I_1 \approx 137.9$), the cycle again becomes unstable and the simultaneuous spiking ends. A cycle corresponding to spiking behaviour of only the second neural mass is stable between two LPC bifurcations located at $I_1 \approx 122.19$ and $I_1 \approx 133.35$ (leftmost LPC bifurcations in Figure 3.8e and 3.8f, simulation shown in Figure 3.8j). For low values of I_1, a cycle remains corresponding to an α-rhythm for the second neural mass and periodic activity with small amplitude for the first neural mass (cycle shown in the bifurcation diagram in Figure 3.8a and 3.8b, simulation shown in Figure 3.8i).

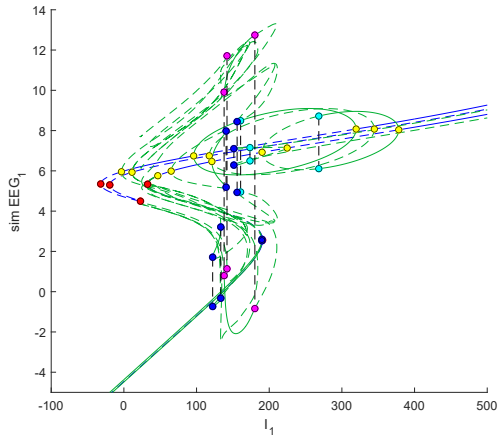

(a) 1-parameter bif. diagram represented in the ECoG signal for NM1.

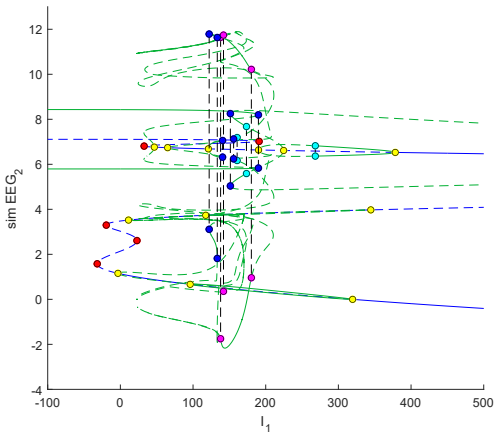

(b) 1-parameter bif. diagram represented in the ECoG signal for NM2.

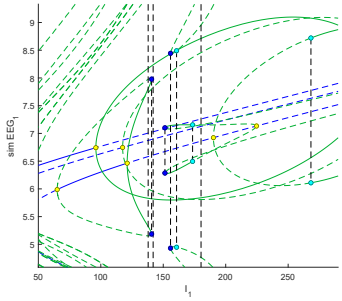

(c) Zoom-in 1.

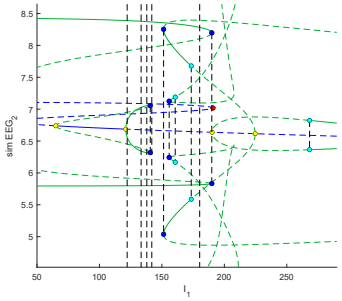

(d) Zoom-in 2.

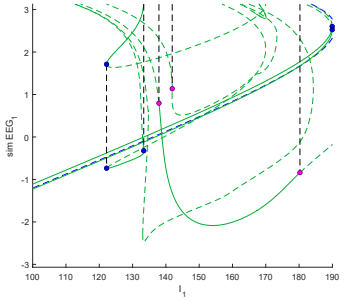

(e) Zoom-in 3.

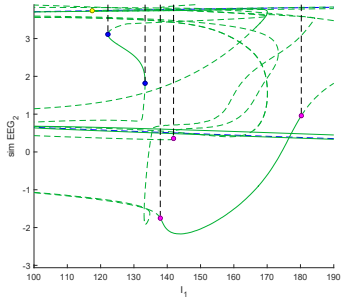

(f) Zoom-in 4.

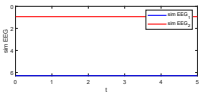

(g) $I_1 = 33$.

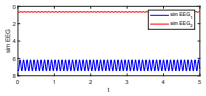

(h) $I_1 = 105.5$.

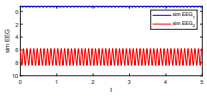

(i) $I_1 = 114$.

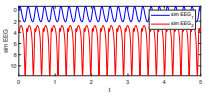

(j) $I_1 = 126$.

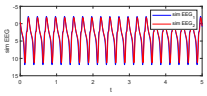

(k) $I_1 = 156$.

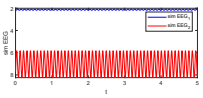

(l) $I_1 = 187$.

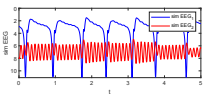

(m) $I_1 = 191$.

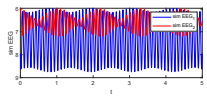

(n) $I_1 = 259$.

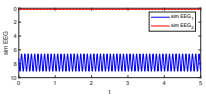

(o) $I_1 = 270$.

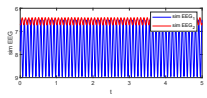

(p) $I_1 = 319.5$.

Figure 3.8: One-parameter bifurcation diagram and simulations for $I_2 = 150$, $\beta = 0.8$. In the bifurcation diagrams, **red** = LP, **yellow** = H, **blue** = LPC, **cyan** = NS, **magenta** = PD.

3.3.3 Bifurcation diagram in the (I_1, β) plane for $I_2 = 150$

Finally, we present a 2-parameter bifurcation diagram for $I_2 = 150$ showing various relevant bifurcations of cycles in the (I_1, β) plane in Figure 3.10. We only show a small subset of all bifurcations, responsible for the switches between spiking and non-spiking behaviour. We do not show codimension 2 bifurcations.

For high values of I_1, the region of spiking behaviour is enclosed between an LPC bifurcation branch and a homoclinic bifurcation. For lower values of I_1, spiking behaviour for the second neural mass is governed by activity with higher period (i.e. torus-like structures, Figures 3.9a and 3.9b). Hence, no specific bounds for the region of spiking behaviour are found for these lower values of I_1. Within this area, a stable cycle corresponding to spiking behaviour of the second neural mass does exist between two LPC bifurcations. The area of SWDs for the second neural mass to the left of the area where both neural masses are seen to spike simultaneously is also bounded by activity with higher period. However, in the center of this region stable cycles can be found that are responsible for SWDs in the second neural mass. We have not pursued a further bifurcation analysis of this region. The region where only spiking behaviour for the first neural mass is seen is also caused by a torus-like structure. Hence, no clear bounds are found for this region in a 2-parameter bifurcation diagram.

Simultaneous spiking in both neural masses is seen between two LPC bifurcations for lower values of β. For higher values of β, simultaneous spiking behaviour exists between two PD bifurcations. Between the region enclosed by the LPC bifurcations and the region enclosed by the PD bifurcations, cycles with higher period exist (simulation shown in Figure 3.9c). We note that the region where simultaneous spiking behaviour exists does not completely coincide with the region between the two PD bifurcations. This may be due to the choice in initial conditions, as simulations show that stable SWDs do remain in the system (Figure 3.9d). Past the PD bifurcations, a stable period-2 cycle remains corresponding to spiking behaviour for both neural masses (Figure 3.9e).

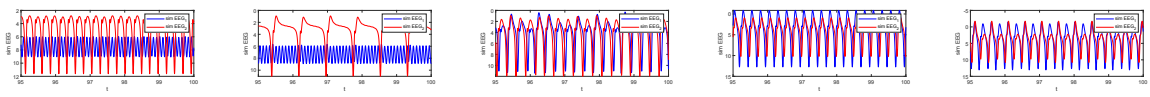

(a) $I_1 = 221$, $\beta = 0.19$. *(b)* $I_1 = 200$, $\beta = 0.39$. *(c)* $I_1 = 137$, $\beta = 0.28$. *(d)* $I_1 = 180$, $\beta = 0.8$. *(e)* $I_1 = 187$, $\beta = 0.9$.

Figure 3.9: Simulations elaborating on specific regions in the 2-parameter bifurcation diagram.

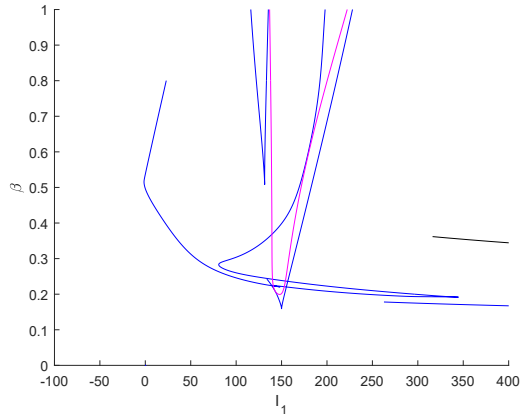

(a) 2-parameter bifurcation diagram.

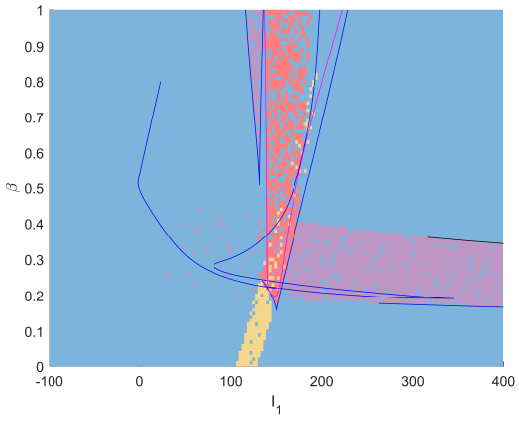

(b) 2-parameter bifurcation diagram plotted along with results from simulations.

Figure 3.10: 2-parameter bifurcation diagram for two reciprocally coupled Jansen-Rit neural mass models with $I_2 = 150$. Here, **blue**=LPC, **magenta**=PD and **black**=Hom.

3.4 Results for two coupled Wendling models

We now analyze two coupled Wendling neural masses with feedforward inhibition. The model and parameter choices are described in Section 2.3.2.

We start by simulating the system and varying I_1 and β while keeping I_2 fixed for various values of I_2. We follow the methods for simulation described in section 3.2. We first consider the case that $B = 24$ and $G = 10$ and set $K^{1,2} = K^{2,1} = 25$. We thus look at a slow inhibition dominated case with weak coupling. We go through the diagrams found in Figure 3.11.

For $I_2 = 100$ (Figure 3.11a) we see that a small band exists where spiking behaviour is present for the first neural mass. The second neural mass never shows spiking behaviour. We note that for larger β a larger region for I_1 corresponds to bistable behaviour where one stable solution corresponds to no spiking behaviour and the other corresponds to only spiking behaviour for the first neural mass.

In the case that $I_2 = 130$ (Figure 3.11b) we see that a region exists for high I_1 and low β where the second neural mass shows spiking behaviour. This behaviour disappears when β becomes larger. There is also a small region where both neural masses spike. When $I_2 = 150$ (Figure 3.11c) spiking behaviour for the second neural mass becomes prominent for low values of I_1. This is interesting as it is not seen for other values of I_2. This may

be attributed to the fact that a single neural mass has a stable cycle corresponding to SWD-like behaviour for $I_2 = 150$.

The observed behaviour for $I_2 = 170$, $I_2 = 200$, $I_2 = 250$ and $I_2 = 300$ (Figures 3.11d, 3.11e, 3.11f and 3.11g) are all qualitatively similar. For higher values of β a region can be seen where both neural masses show SWD-like behaviour simulaneously. Moreover, for a certain range of β we see that spiking behaviour for the second neural mass is prominent for large I_1. A region where both no spiking behaviour as well as spiking behaviour for the second neural mass are stable remains close to the band where both neural masses are seen spiking simultaneously.

The result obtained for $B = 24, G = 10$ shows similar dynamics when compared to the results for two coupled Jansen-Rit models. A small band exists where the first neural mass always spikes. For larger values of I_2 a region exists for high values of I_1 and $\beta > 0$ where only the second neural mass shows SWD-like behaviours. Lastly, there exists a band for $\beta > 0$ where both neural masses are seen to spike simultaneously. This similarity can be attributed to the fact that for the parameter choices $B = 24, G = 10$ the slow inhibition is dominant in the Wendling model.

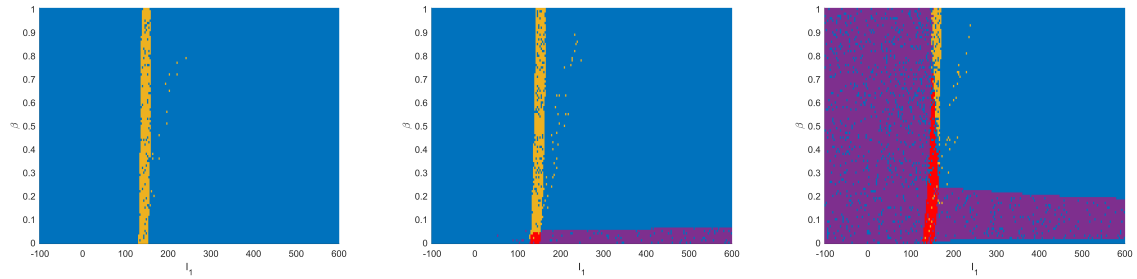

(a) Spiking behaviour for $I_2 = 100$. *(b)* Spiking behaviour for $I_2 = 130$. *(c)* Spiking behaviour for $I_2 = 150$.

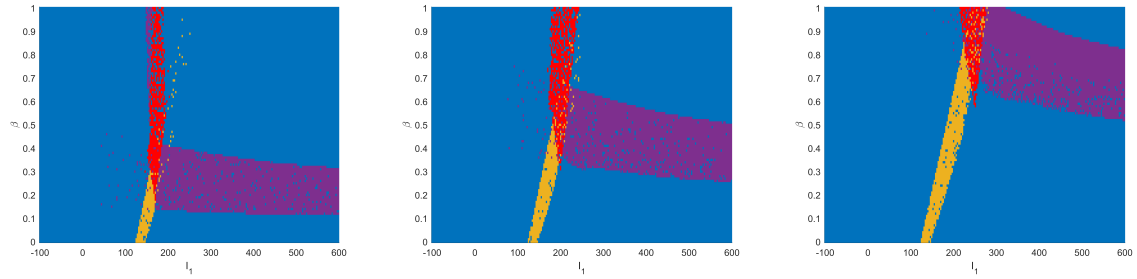

(d) Spiking behaviour for $I_2 = 170$. *(e)* Spiking behaviour for $I_2 = 200$. *(f)* Spiking behaviour for $I_2 = 250$.

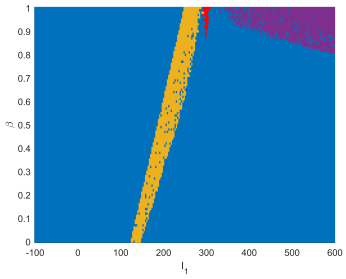

(g) Spiking behaviour for $I_2 = 300$.

Figure 3.11: Diagrams showing regions of spiking behaviour for both coupled neural masses. I_1 and β are varied, whereas I_2 is fixed. Here, **blue** means no neural mass is spiking, **yellow** means only neural mass 1 is spiking, **purple** means only neural mass 2 is spiking and **red** means both neural masses are spiking.

We now consider the case $B = 22, G = 8$. In this case we see qualitatively different dynamics for a single Wendling neural mass than for a single Jansen-Rit neural mass. Since low values of connectivity between neural masses yield no spiking behaviour in two coupled neural masses we increase $K^{1,2}$ and $K^{2,1}$ and set $K^{1,2} = K^{2,1} = 100$.

For $I_2 = 100$ (Figure 3.12a) no spiking behaviour is seen for either neural mass. For $I_2 = 150$ and $I_2 = 170$ (Figures 3.12b and 3.12c) we see a small region where both neural masses show SWD-like behaviour. This region ceases to exist for large values of β but is not seen when $\beta = 0$. This region grows for higher values of I_2. In the case that $I_2 = 250$

(Figure 3.12d) we see that a large region of spiking behaviour for both neural masses exists for higher values of β. Moreover, we see a small band where stable spiking behaviour for just the second neural mass is seen. Lastly, for $I_2 = 350$ we see that the region of simultaneous spiking grows larger. Moreover, a narrow region of SWDs is found for the first neural mass for lower values of β.

For the parameter choices $B = 22$, $G = 8$ we note that no spiking behaviour is found in the case $\beta = 0$. Moreover, we see that increased feedforward inhibition can bring the system to a state where both neural masses spike simultaneously. The disappearance of many regions where only one neural mass spikes may be attributed to the increased value for $K^{1,2}$ and $K^{2,1}$.

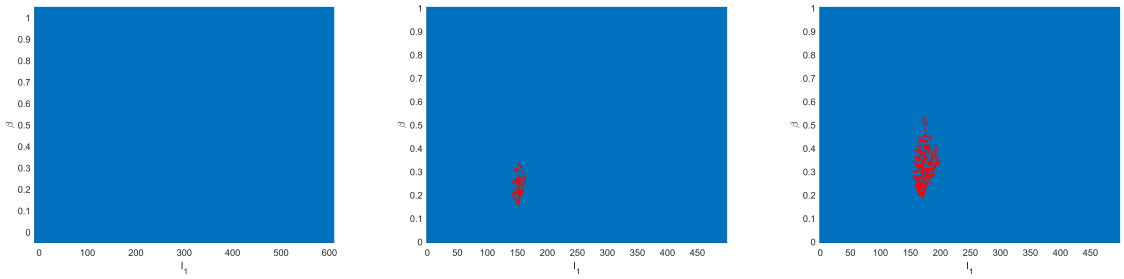

(a) Spiking behaviour for $I_2 = 100$. *(b)* Spiking behaviour for $I_2 = 150$. *(c)* Spiking behaviour for $I_2 = 170$.

(d) Spiking behaviour for $I_2 = 250$. *(e)* Spiking behaviour for $I_2 = 350$.

Figure 3.12: Diagrams showing regions of spiking behaviour for both coupled neural masses. I_1 and β are varied, whereas I_2 is fixed. Here, **blue** means no neural mass is spiking, **yellow** means only neural mass 1 is spiking, **purple** means only neural mass 2 is spiking and **red** means both neural masses are spiking.

For the case that $I_2 = 250$ and $\beta = 0.65$, we also investigate the influence of the strength of both the feedforward and feedback connectivity. The results for these simulations are given in Figure 3.13.

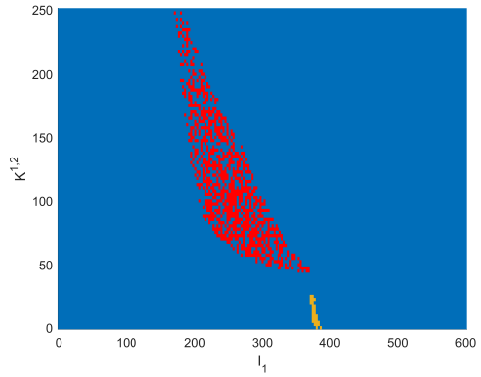

(a) Spiking behaviour for $K^{2,1} = 100$.

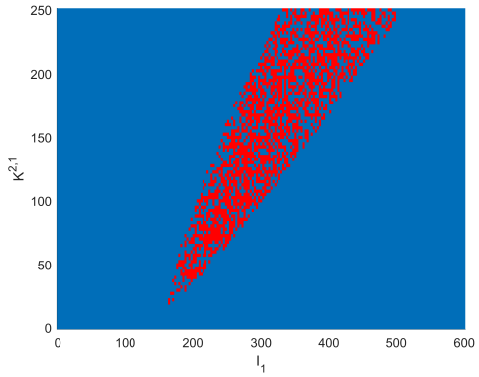

(b) Spiking behaviour for $K^{1,2} = 100$.

Figure 3.13: Diagrams showing regions of spiking behaviour for both coupled neural masses. I_2 and β are fixed. Here, **blue** means no neural mass is spiking, **yellow** means only neural mass 1 is spiking, **purple** means only neural mass 2 is spiking and **red** means both neural masses are spiking.

We have found that simultaneous spiking behaviour for both Wendling neural masses ceases to exist if the feedforward connectivity is too weak or too strong. Moreover, we find that increasing the feedback connectivity promotes the generation of simultaneous SWD-like activity in both coupled neural mass models. This is similar to what was found for two coupled Jansen-Rit models in section 3.3.

3.4.1 Bifurcation analysis for $\mathbf{B = 22}$, $\mathbf{G = 8}$

In this section we provide a bifurcation analysis of two coupled Wendling neural masses for the case that $B = 22$ and $G = 8$. We choose not to do a bifurcation analysis for the case that $B = 24, G = 10$ as the activity of the system is then shown to be very similar to the activity of two coupled Jansen-Rit neural masses (as seen in Figure 3.11). Spiking behaviour for this case is shown in Figure 3.12.

Bifurcation analysis for $I_2 = 250$, $\beta = 0$

We start by considering the case that $I_2 = 250$ and $\beta = 0$. Bifurcation diagrams and simulations are shown in Figure 3.14. We see that there is a single equilibrium branch, that becomes unstable between two Hopf bifurcations and between a Hopf bifurcation and a fold bifurcation (Figures 3.14a and 3.14b). Between two Hopf bifurcations, a stable cycle exists corresponding to and α-rhythm for both neural masses (Figure 3.14e). From a second Hopf point an unstable cycle emerges that disappears after a homoclinic bifurcation (Figures 3.14a and 3.14b). We see no stable behaviour corresponding to SWD-like activity, which is in correspondence with what is found in the simulations shown in Figure 3.12.

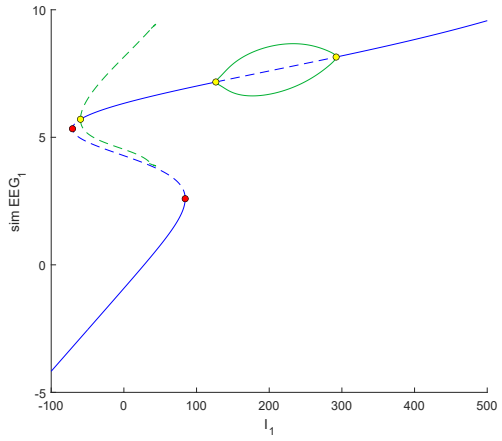

(a) 1-parameter bif. diagram represented in the ECoG signal for NM1.

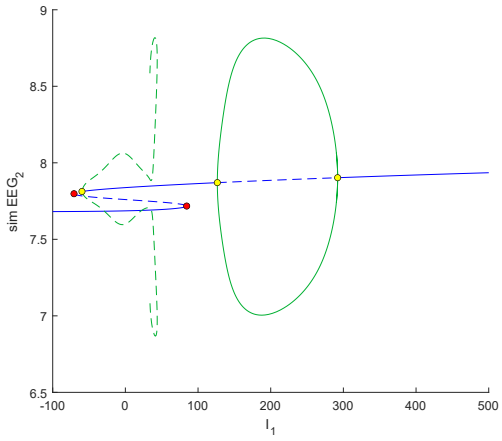

(b) 1-parameter bif. diagram represented in the ECoG signal for NM2.

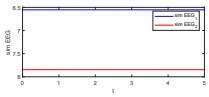

(c) $I_1 = 30$.

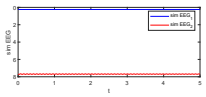

(d) $I_1 = 35$.

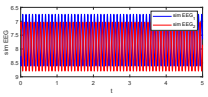

(e) $I_1 = 210$.

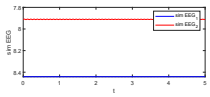

(f) $I_1 = 340$.

Figure 3.14: One-parameter bifurcation diagram and simulations for $I_2 = 250$, $\beta = 0$. In the bifurcation diagrams, **red** = LP, **yellow** = H, **blue** = LPC, **cyan** = NS, **magenta** = PD.

Bifurcation analysis for $I_2 = 250$, $\beta = 0.3$

We now give the 1-parameter bifurcation diagram for the case that $I_2 = 250$ and $\beta = 0.3$, shown in Figure 3.15. We see here that there is a small region for large I_1 where SWD-like behaviour occurs for the second neural mass (Figure 3.15a and 3.15b, a better view of the cycle in the second neural mass is given in Figure 3.15e). The region where this stable limit cycle exists starts at an LPC bifurcation around $I_1 \approx 455$. The cycle then becomes unstable between two LPC bifurcations and between two PD bifurcations before finally ending in a homoclinic bifurcation. Simulations are shown in Figures 3.15l and 3.15n.

For $I_1 \approx 390$ a Neimark-Sacker bifurcation is found along a stable limit cycle. For higher values of I_1 the stable limit cycle corresponds to an α-rhythm for the second neural mass and smaller oscillations for the first neural mass (Figure 3.15k and 3.15m). Due to the Neimark-Sacker bifurcation a torus-like structure exists for $I_1 < 390$. This torus-like structure corresponds to an α-rhythm for both neural masses with different frequencies (Figure 3.15j). Past a second Neimark-Sacker bifurcation near $I_1 \approx 270$, a stable limit cycle remains corresponding to α-rhythms for both neural masses with the same frequency (Figure 3.15i). This cycle ends in a Hopf bifurcation.

From a Hopf bifurcation near $I_1 \approx 200$, a stable cycle emerges that corresponds to small oscillatory behaviour for both neural masses (Figure 3.15h). This behaviour becomes unstable after an NS bifurcation and becomes stable again after an LPC point before ending in another Hopf point (Figures 3.15a and 3.14b). An unstable cycle emerges from a Hopf point near $I_1 \approx 90$, corresponding to unstable spiking behavour for the first neural mass. After various bifurcations, this cycle ends in a homoclinic bifurcation. The cycle never becomes stable (Figures 3.15c and 3.15d).

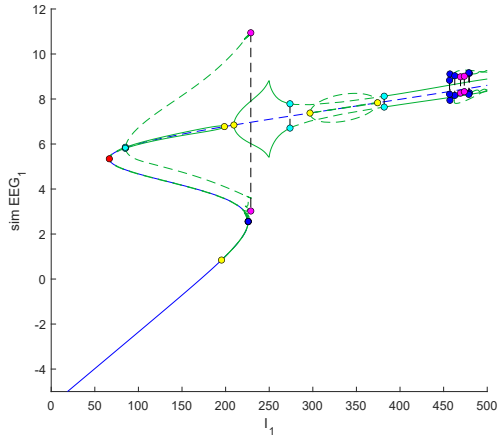

(a) 1-parameter bif. diagram represented in the ECoG signal for NM1.

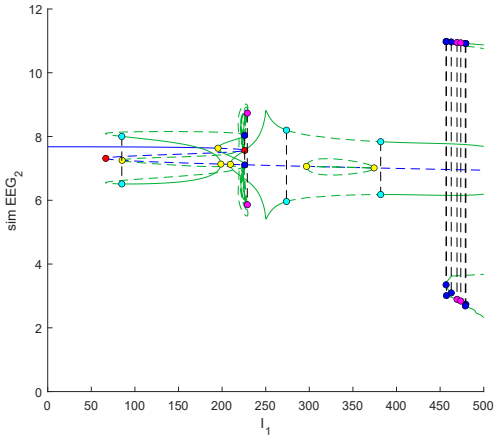

(b) 1-parameter bif. diagram represented in the ECoG signal for NM2.

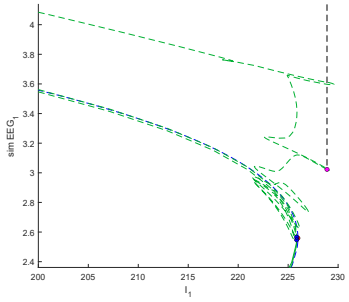

(c) Zoom-in 1.

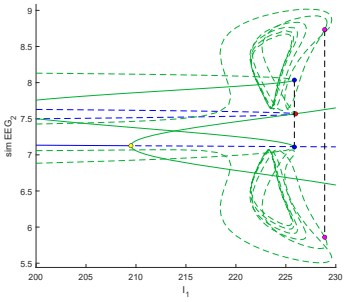

(d) Zoom-in 2.

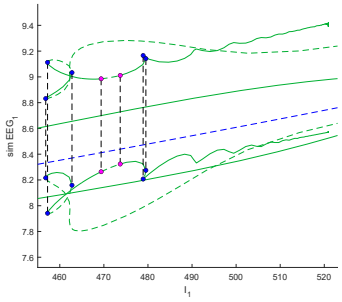

(e) Zoom-in 3.

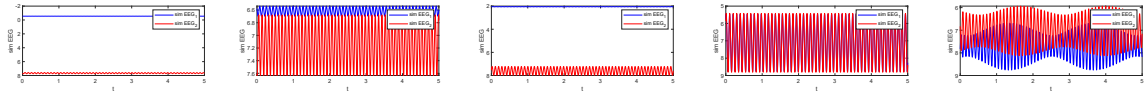

(f) $I_1 = 155$. *(g)* $I_1 = 175$. *(h)* $I_1 = 222$. *(i)* $I_1 = 250$. *(j)* $I_1 = 350$.

(k) $I_1 = 420$. *(l)* $I_1 = 459$. *(m)* $I_1 = 491$. *(n)* $I_1 = 498$.

Figure 3.15: One-parameter bifurcation diagram and simulations for $I_2 = 250$, $\beta = 0.3$. In the bifurcation diagrams, **red** = LP, **yellow** = H, **blue** = LPC, **cyan** = NS, **magenta** = PD.

Bifurcation analysis for $I_2 = 250$, $\beta = 0.7$

We now give the 1-parameter bifurcation diagram for the case that $I_2 = 250$ and $\beta = 0.7$, shown in Figure 3.16. Here, we see that there exists a stable cycle with large amplitude, originating from a Hopf point near $I_1 = 360$ (best seen in Figures 3.16a and 3.16b). This cycle becomes stable at a limit-point of cycles bifurcation around $I_1 = 320$ and loses stability after a period-doubling bifurcation at $I_1 \approx 215$. This is consistent with the region of spiking behaviour for both neural masses found in the simulations in Figure 3.12d. A simulation of the synchronized SWD-like behaviour is given in Figure 3.16k.

Otherwise, mostly small oscillations are seen in the simulations, though various unstable cycles exist in the system. For high values of I_1 a stable equilibrium exists (Figure 3.16m). Near $I_1 \approx 340$, a supercritical Hopf bifurcation occurs from which a stable cycle emerges showing small oscillations for both the first and second neural mass (Figure 3.16l). This stable cycle becomes unstable after an LPC bifurcation near $I_1 \approx 420$.

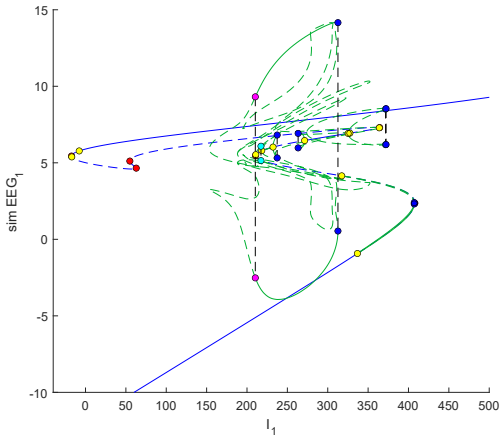

(a) 1-parameter bif. diagram represented in the ECoG signal for NM1.

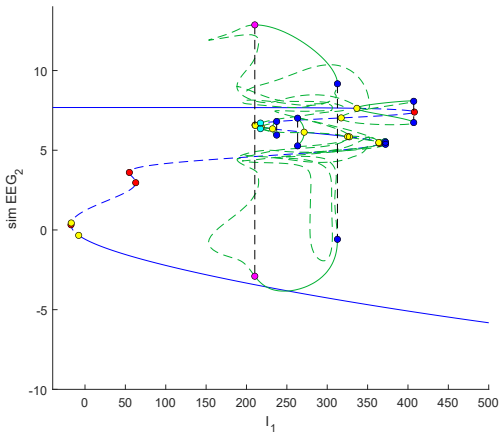

(b) 1-parameter bif. diagram represented in the ECoG signal for NM2.

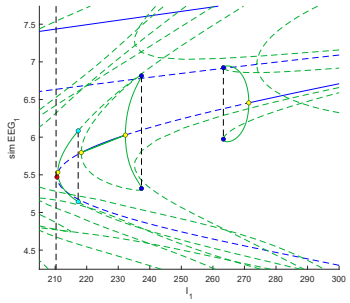

(c) Zoom-in 1.

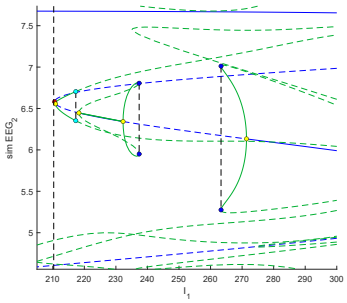

(d) Zoom-in 2.

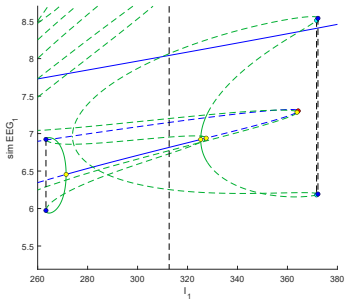

(e) Zoom-in 3.

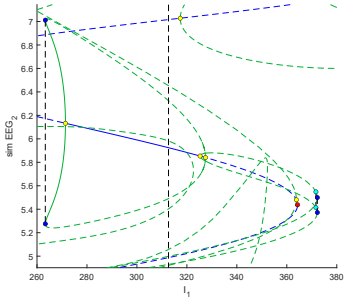

(f) Zoom-in 4.

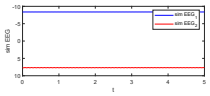

(g) $I_1 = 110$.

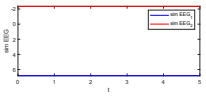

(h) $I_1 = 110.5$.

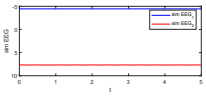

(i) $I_1 = 230.5$.

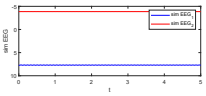

(j) $I_1 = 255$.

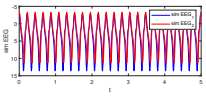

(k) $I_1 = 284$.

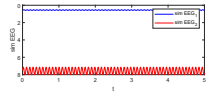

(l) $I_1 = 377.5$.

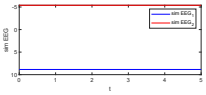

(m) $I_1 = 440$.

Figure 3.16: One-parameter bifurcation diagram and simulations for $I_2 = 250$, $\beta = 0.7$. In the bifurcation diagrams, **red** = LP, **yellow** = H, **blue** = LPC, **cyan** = NS, **magenta** = PD.

Bifurcation analysis for $I_2 = 170$, $\beta = 0.3$

The bifurcation diagram for the case that $I_2 = 170$ and $\beta = 0.3$ is shown in Figure 3.17. The main goal of this analysis is to identify the dynamics responsible for the onset and offset of SWD-like behaviour for these parameter settings, when compared to the results found for $I_2 = 250, \beta = 0.7$. For high values of I_1 we see that two stable equilibria exist (Figures 3.17a and 3.17b, simulations in Figures 3.17k and 3.17l). We note that throughout the bifurcation diagram, two branches of equilibria are seen compared to one for the case that $I_2 = 250, \beta = 0.7$. At around $I_1 \approx 380$ a supercritical Hopf bifurcation occurs resulting in a stable limit cycle. This limit cycle corresponds to an α-rhythm for the first neural mass and smaller oscillations for the second neural mass (Figure 3.17j) and ends in another Hopf bifurcation.

Similar to the case where $I_2 = 250$, $\beta = 0.7$ we see that a region exists between an LPC bifurcation and a period-doubling point where synchronized SWD-like activity is found (Figure 3.17a and 3.17b, simulation shown in Figure 3.17i). Hence, we find that the dynamics underlying the region of simultaneous spiking is the same as the case where $I_2 = 250, \beta = 0.7$.

For low values of I_1, we see that the simulations converge to either the high equilibrium for the first neural mass or the low equilibrium for the first neural mass (Figures 3.17h and 3.17g).

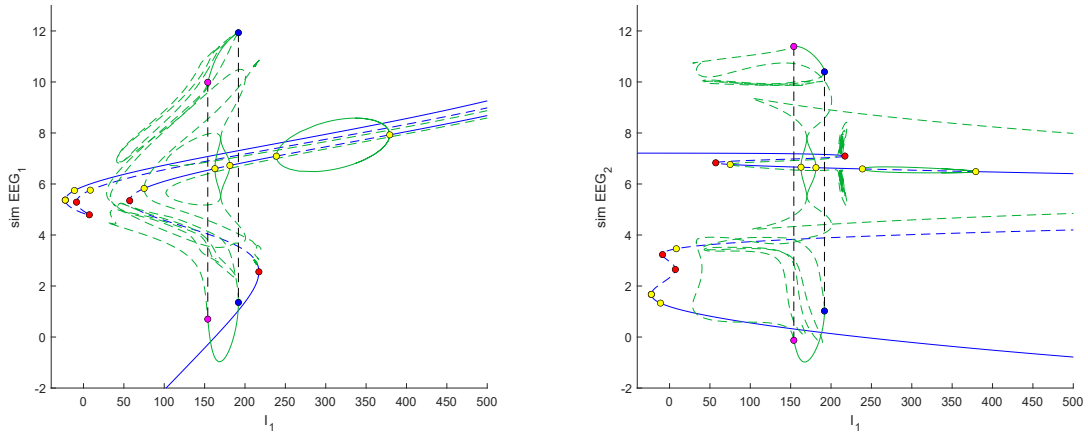

(a) 1-parameter bif. diagram represented in the ECoG signal for NM1.

(b) 1-parameter bif. diagram represented in the ECoG signal for NM2.

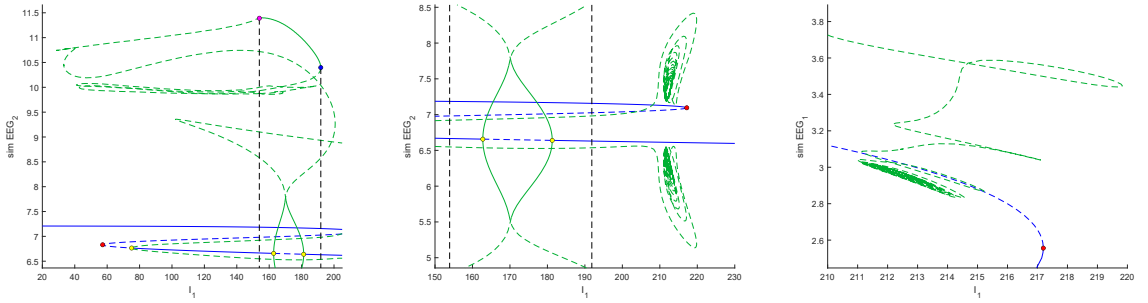

(c) Zoom-in 1. *(d)* Zoom-in 2. *(e)* Zoom-in 3.

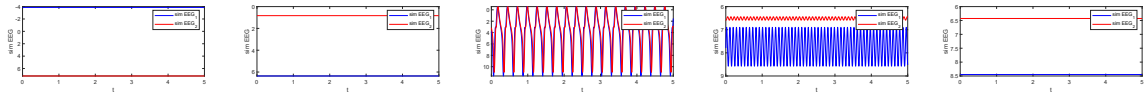

(f) $I_1 = 45$. *(g)* $I_1 = 48$. *(h)* $I_1 = 180$. *(i)* $I_1 = 344$. *(j)* $I_1 = 464$.

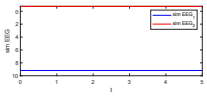

(k) $I_1 = 490$.

Figure 3.17: One-parameter bifurcation diagram and simulations for $I_2 = 170$, $\beta = 0.3$. In the bifurcation diagrams, **red** = LP, **yellow** = H, **blue** = LPC, **cyan** = NS, **magenta** = PD.

3.4.2 Bifurcation diagram in the (I_1, β) plane for $I_2 = 250$

Finally, we show a 2-parameter bifurcation diagram for two reciprocally coupled Wendling neural mass models with $I_2 = 250$ in Figure 3.18. Again, we only show bifurcations relevant for explaining switches between no SWD-like behaviour and SWD-like behaviour. Moreover, we do not consider codimension 2 bifurcations.

We see that the small band of spiking behaviour for the second neural mass is bounded from below by an LPC bifurcation. This region is bounded from above by a homoclinic bifurcation which we were not able to continue.

The region where simultaneous spiking is seen is bounded from the left by an LPC bifurcation for lower values of β. For higher values of β, the cycle responsible for simultaneous spiking becomes unstable on the left after a PD bifurcation. No stable period-2 cycles were found through simulations. On the right side, the region of simultaneous spiking is also bounded by an LPC bifurcation for low values of β. For higher values of β, either a Neimark-Sacker or a period-doubling bifurcation causes the cycle to become unstable. Once again, no simulations of doubled cycles or torus-like attractors were found through simulations.

We note that the region where the cycle responsible for simultaneous spiking becomes unstable due to a PD or NS bifurcation falls outside of our considered set of one-parameter bifurcation diagrams.

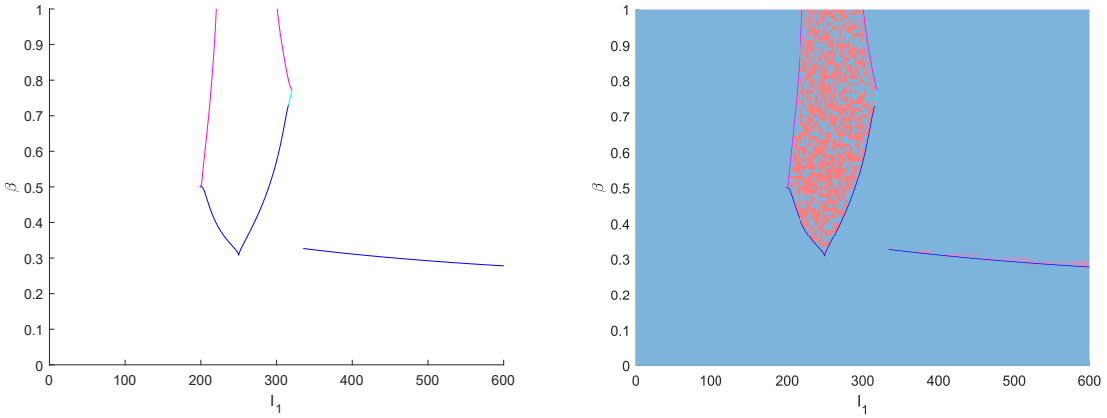

(a) 2-parameter bifurcation diagram.

(b) 2-parameter bifurcation diagram plotted along with results from simulations.

Figure 3.18: 2-parameter bifurcation diagram for two reciprocally coupled Wendling neural mass models with $I_2 = 250$, $K^{1,2} = K^{2,1} = 100$. Here, **blue**=LPC, **magenta**=PD and **cyan**=NS.

3.5 Conclusions

In our analysis, we have considered the activity of two weakly coupled reciprocally coupled Jansen-Rit and Wendling neural mass models in detail as well as the influence of feedforward inhibition on this activity. We have found that two coupled neural mass models give rise to complex dynamics and various pathways to activity associated with epilepsy.

In our analysis, we have seen that feedforward inhibition has a large influence on the activity of coupled neural mass models. In two coupled Jansen-Rit models and the slow inhibition-dominated Wendling model, we observe that for higher excitatory background input I_1, I_2 for both neural masses, spike-wave discharges occur in the second neural mass for a band of values for the feedforward inhibition scaling β. We note that these higher values for the excitatory background input are normally associated with a healthy α-rhythm for neural masses as seen in Figures 2.2 and 2.4 [23].

Epileptiform activity often involves synchronized, high amplitude activity. Thus, synchronous spiking behaviour is particularly interesting when considering the results of our analysis. Small regions of simultaneous population spiking behaviour are found. For two Jansen-Rit models with weak coupling synchronous spiking is only found for larger β and

small regions of I_1 where I_1 is close to I_2. When looking at a fast inhibition-dominated case for two Wendling models with stronger coupling, we have indentified a region where spiking activity occurs for both neural masses simultaneously and synchronously. This simultaneous spiking only occurs for nonzero values of β. The large regions of synchronous spiking suggests that coupled Wendling models with strong coupling are more suitable for explaining epileptic activity.

Our findings show that the addition of feedforward inhibition to neural mass models has a large effect on the activity of these neural masses and can promote the appearance of activity associated with epilepsy. The results of this chapter provide a link between the modelling of delayed responses in neural mass models and spontaneous activity of neural mass models. Delayed responses in SPES are considered to be biomarkers of the epileptogenic zone and feedforward inhibition is an essential ingredient for modelling DRs in coupled neural mass models [6]. The fact that feedforward inhibition promotes the generation of spike-wave discharges for nonzero values of β is thus consistent with this modelling choice and the underlying clinical data.

In the various cases we consider in our bifurcation analysis, we have found that many pathways to SWD-like activity are present in two coupled neural masses. Most commonly, a fold bifurcation of a limit cycle or a homoclinic bifurcation are responsible for the onset or offset of SWD-like activity. In literature, it has been shown that it is possible to infer the bifurcations underlying seizure onset and seizure offset from clinical data [30]. Hence, the analysis in this chapter may provide a basis for the investigation of (patient-specific) generation of seizures in coupled neural mass models.

Chapter 4

Modelling stimulation evoked activity in networks of neural mass models

4.1 Introduction

For clinical purposes, a network of neural masses is desired. In such a model, each neural mass represents an electrode as placed on the brain during single pulse electrical stimulation (SPES). In this procedure, used during presurgical monitoring for patients with epilepsy, short monophasic pulses are given to pairs of electrodes placed directly on the brain. Responses to this stimulation are measured in other electrodes placed on the brain. In networks of two feedforward coupled Wendling neural masses it has been shown that it is possible to model both early and delayed responses with the addition of feedforward inhibition to the model [6]. To create a computational model that can be used to predict surgery outcome for patients with epilepsy, responses evoked by SPES should be modelled correctly. Hence, our goal is to construct a network of neural masses that are coupled following the network implied by early responses in SPES and show desired ERs and DRs in simulations.

This chapter is organised in the following way. We construct a network of neural mass models and first map the occurrence of evoked activity in tiny networks to gain insight into the influence of different parameters on the generation of evoked responses. We then fit ERs and DRs in artificial networks of 12 nodes using an evolutionary algorithm and reflect on the results. Finally, we use our evolutionary algorithm to fit ERs and DRs in data provided by the University Medical Centre Utrecht.

4.2 Methods

We first describe our methods. We introduce the method by which ER networks are constructed. We then give the neural mass model used in our networks and describe how stimulation is modelled within Wendling neural mass models. Moreover, we give the used evolutionary algorithm for fitting ERs and DRs in larger networks of neural masses. Lastly, we describe our method of generating small artificial ER networks.

4.2.1 Early response networks

Since early responses are indicative of connections between areas of the brain, data of the occurrence of ERs can be used to construct a network representing the connectivity in the brain. Such ER networks form the basis for modelling connections within a patient-specific network of neural mass models. Within a patient-specific network, neural mass models should be coupled if a connection is present in the ER network, and no other strong connections should exist.

After SPES measurements, a matrix is constructed that contains whether the stimulation of a pair of electrodes results in an evoked ER in another electrode. We construct a network from this information in the following way. Each electrode corresponds to a node in the constructed graph. A directed edge from node A to node B is added if there is at least one stimulation pair containing electrode A that evokes an early response in electrode B. Hence no double connections or adjustments to the connection are made if an electrode A is present in multiple electrode pairs that evoke an ER in electrode B. The obtained ER network is a simple directed graph. For an introduction to graph theory, we refer to Grimaldi et al. [31].

In Appendix B, we discuss the validity of ER networks as an accurate representation of connectivity of the brain in detail. We have found that under the assumption of nearest neighbour coupling, ER networks may be assumed to represent connectivity in the brain with sufficient accuracy.

4.2.2 Coupled Wendling neural masses with stimulation

We give the model used for each neural mass, as well as a description of how stimulation is modelled within neural mass models. Apart from the addition of this stimulation, the model used here is the same as the Wendling model with feedforward inhibition as described in Chapter 2 and analysed in Chapter 3. The equations for neural mass j are given by

$$\begin{cases} \dot{v}_{0j} = z_{0j}, \\ \dot{z}_{0j} = Aa\sigma(u_{\mathsf{py}_j}) - 2az_{0j} - a^2 v_{0j}, \\ \dot{v}_{1j} = z_{1j}, \\ \dot{z}_{1j} = Aa(C_2\sigma(u_{\mathsf{ex}_j}) + I_j + I_{\mathsf{stim}} + \sum_{i\neq j} K^{i,j} v_{4i}) - 2az_{1j} - a^2 v_{1j}, \\ \dot{v}_{2j} = z_{2j}, \\ \dot{z}_{2j} = Bb(C_4\sigma(u_{\mathsf{is}_j}) + \beta_j \sum_{i\neq j} K^{i,j} v_{4i}) - 2bz_{2j} - b^2 v_{2j}, \\ \dot{v}_{3j} = z_{3j}, \\ \dot{z}_{3j} = Gg(C_7\sigma(u_{\mathsf{if}_j}) + \gamma_j \sum_{i\neq j} K^{i,j} v_{4i}) - 2gz_{3j} - g^2 v_{3j}, \\ \dot{v}_{4j} = z_{4j}, \\ \dot{z}_{4j} = Ad\sigma(u_{\mathsf{py}_j}) - 2dz_{4j} - d^2 v_{4j}. \end{cases} \tag{4.1}$$

Here, $i, j \in \{1, ..., N\}$, and

$$\begin{cases} u_{\mathsf{py}_j} = v_{1j} - v_{2j} - v_{3j}, \\ u_{\mathsf{ex}_j} = C_1 v_{0j}, \\ u_{\mathsf{is}_j} = C_3 v_{0j}, \\ u_{\mathsf{if}_j} = C_5 v_{0j} - \frac{C_6}{C_4} v_{2j}. \end{cases}$$

The sigmoid function $\sigma(v)$ is given by

$$\sigma(v) = \frac{2e_0}{1 + e^{r(v_0 - v)}}.$$

Here, $K \in \mathbb{R}^{N \times N}$ where $K^{i,i} = 0$ for all $i \in \{1, ..., N\}$. Stimulation of a neural mass is modelled as a short block pulse applied to the population of excitatory neurons. Let $T = \{t_1, t_2, ..., t_n\}$ denote the times at which a stimulation is applied. Setting stimulation times $t_i \in T$ we thus have

$$I_{\text{stim}} = \begin{cases} 1500 & \text{if } t \in [t_i, t_i + \frac{1}{100}] \text{ for some } t_i \in T, \\ 0 & \text{else.} \end{cases}$$

The connectivity matrix K represents the weight matrix for a weighted graph $G = (V, E, K)$ where V denotes the labelled sets of nodes in the network, $|V| = N$, and E denotes the set of edges in the graph. Parameter choices are given in Table 4.1.

In simulations done using this model, responses resembling ERs and DRs are detected in the following way. A simulation of 11 seconds is run, with a stimulation at $t = 10$ s. The maximum and minimum simulated EEG signals for each node of the network of neural masses are calculated for the interval $t \in [5, 10]$. If these differ by more than 1 mV, the system is deemed to be in an oscillatory state. Otherwise, we determine the equilibrium state of the system. If the simulated EEG drops 5 mV below the equilibrium state in the interval $t \in [10, 10.3]$, we say that an ER is present. If the simulated EEG drops 10 mV below the equilibrium state in the interval $t \in [10.4, 11]$ we determine that a DR is present. We note that these intervals do not correspond to the intervals commonly associated with ERs and DRs. However, the N2 peak is larger than the N1 peak and occurs later than 100 ms after stimulation. It is important to avoid miscategorization of a large N2 peak as a delayed response.

Parameter	Interpretation	Value
A	Synaptic gain for excitatory and pyramidal populations	4.5
B	Synaptic gain for slow inhibitory population	7
G	Synaptic gain for fast inhibitory population	25
a	Reciprocal of time scale for excitatory and pyramidal populations	100
b	Reciprocal of time scale for slow inhibitory population	10
g	Reciprocal of time scale for fast inhibitory population	130
d	Reciprocal of time scale for output	100
C	Connectivity constant	135
c_1	Relative connectivity of pyramidal to excitatory population	1
c_2	Relative connectivity of excitatory to pyramidal population	0.8
c_3	Relative connectivity of pyramidal to slow inhibitory population	0.25
c_4	Relative connectivity of slow inhibitory to pyramidal population	0.25
c_5	Relative connectivity of pyramidal to fast inhibitory population	0.3
c_6	Relative connectivity of slow inhibitory to fast inhibitory population	0.1
c_7	Relative connectivity of fast inhibitory to pyramidal population	0.8
e_0	Half the difference between $\max_v(\sigma(v))$ and $\min_v(\sigma(v))$	2.5
v_0	Potential for which the sigmoid function has its median value	4.5
r	Slope of sigmoid function	0.56
I_j	Excitatory background input for pyramidal population	Varied
α	Part of external input going to excitatory population	0.1
β_j	Part of external input going to slow inhibitory population	Varied
γ_j	Part of external input going to fast inhibitory population	$0.7\beta_j$
$K^{i,j}$	Connectivity between neural mass i and neural mass j	Varied

Table 4.1: Parameter values for Wendling's neural mass model, based on parameter choices made by Hebbink et al. [6].

4.2.3 Evolutionary algorithm for fitting ERs and DRs

To fit parameters for generating ERs and DRs in larger networks of coupled neural masses, we apply an evolutionary algorithm to minimize a loss function. We restrict our search space to the connectivity matrix $K \in \mathbb{R}^{N\times N}$, the external excitatory input $\mathbf{I} \in \mathbb{R}^N$ and the amount of feedforward inhibition present in each node $\beta \in \mathbb{R}^N$. The choices for K and $\mathbf{I}$ as control parameters are natural, as the connectivity between different areas of the brain and external input from areas outside the considered grid is expected to vary in the network. The choice for β as control parameter is made due to the known importance of feedforward inhibition in simulating early and delayed responses.

We now define our loss function. Suppose that a graph representing the ER network $G = (V, E)$, $|V| = N$ is given and let A be the adjacency matrix for this graph. Stimulation pairs are given in a set S, in which each element is a tuple of two distinct vertices of G.

Let $\mathbf{r} : \mathbb{R}^{N\times N} \times \mathbb{R}^N \times \mathbb{R}^N \to \mathbb{R}^{|S|\times N}$ be given so that $\mathbf{r}(K, \mathbf{I}, \beta) = R$ where $R_{ij} = 1$ if stimulating stimulation pair i causes an ER in node j for the connectivity matrix K and $R_{ij} = 0$ otherwise. Moreover, we let $R^{(0)} \in \mathbb{R}^{|S|\times N}$ be the matrix such that $R^{(0)}_{ij} = 1$ if an ER is desired in node j upon stimulating stimulation pair i and $R^{(0)}_{ij} = 0$ otherwise. Similarly, let $\mathbf{d} : \mathbb{R}^{N\times N} \times \mathbb{R}^N \times \mathbb{R}^N \to \mathbb{R}^{|S|\times N}$ so that $\mathbf{d}(K, \mathbf{I}, \beta) = D$ where $D_{ij} = 1$ if stimulating stimulation pair i evokes a DR in node j for connectivity matrix K, input $\mathbf{I}$ and feedforward inhibition β, and $D_{ij} = 0$ otherwise. We let $D^{(0)} \in \mathbb{R}^{|S|\times N}$ be the matrix containing where DRs are desired. Lastly, let $o : \mathbb{R}^{N\times N} \times \mathbb{R}^N \times \mathbb{R}^N \to \{0, 1\}$ where $o(K, \mathbf{I}, \beta) = 1$ if the network of neural mass models with parameters $K, \mathbf{I}$ and β is in an oscillatory state for any node, and $o(K, \mathbf{I}, \beta) = 0$ otherwise. Using these maps, we can define our loss function as follows:

$$f(K, \mathbf{I}, \beta) = \begin{cases} M \text{ if } o(K, \mathbf{I}, \beta) = 1, \\ \sum_{i=1}^{|S|} \sum_{j=1}^{N} \left| \left(\mathbf{r}(K, \mathbf{I}, \beta) - R^{(0)}\right)_{ij} \right| + 10 \left| \left(\mathbf{d}(K, \mathbf{I}, \beta) - D^{(0)}\right)_{ij} \right| \text{ else.} \end{cases}$$

Here, M is a large constant satisfying $M > 11|S|N$ to ensure that oscillatory behaviour is always discouraged. The penalty from an unwanted or unfound ER is set to 1, while the penalty for an unwanted or unfound DR is set to 10. An alternative loss function is defined in the case that a conservative guess for the parameter values $(\hat{K}, \hat{\mathbf{I}}, \hat{\beta})$ is known for which no oscillatory behaviour is present. In this case, let $p : \mathbb{R}^{N\times N} \times \mathbb{R}^N \times \mathbb{R}^N \to \mathbb{R}$ where

$$p(K, \mathbf{I}, \beta) = \sum_{i=1}^{|S|} \sum_{j=1}^{N} \left| \left(K - \hat{K}\right)_{ij} \right| + \sum_{j=1}^{N} \left| \left(\mathbf{I} - \hat{\mathbf{I}}\right)_{j} \right| + \sum_{j=1}^{N} \left| \left(\beta - \hat{\beta}\right)_{j} \right|.$$

We then adjust the loss function to

$$f(K, \mathbf{I}, \beta) = \begin{cases} M + p(K, \mathbf{I}, \beta) \text{ if } o(K, \mathbf{I}, \beta) = 1, \\ \sum_{i=1}^{|S|} \sum_{j=1}^{N} \left| \left(\mathbf{r}(K, \mathbf{I}, \beta) - R^{(0)}\right)_{ij} \right| + 10 \left| \left(\mathbf{d}(K, \mathbf{I}, \beta) - D^{(0)}\right)_{ij} \right| \text{ else.} \end{cases} \tag{4.2}$$

In this way, parameter choices closer to a known non-oscillatory solution are preferred in the loss function in the case that oscillatory behaviour is found.

We use a differential evolution algorithm to optimize parameter choices for the loss function defined in Equation 4.2 [32]. Differential evolution is known to be an efficient method for optimizing non-differentiable loss functions such as the one posed in (4.2). Moreover, the method generally scales better to high-dimensional problems than other popular algorithms, such as Particle Swarm Optimization [33]–[35].

We give an overview of the standard Differential Evolution algorithm as described in [32]. Given an objective function $f : \mathbb{R}^N \to \mathbb{R}$, our goal is to find $x^* \in D$ where $D \subseteq \mathbb{R}^N$ so that

$$f(x^*) \leq f(x) \quad \forall x \in D.$$

Differential evolution works by repeatedly updating a population of N_p individuals. Initialization is done by uniformly randomly choosing vectors from $v^{(i)} \in \mathbb{R}^N$, $i \in \{1, ..., N_p\}$ to create an initial population. Each of these individuals is then iteratively updated in the following way.

We consider the update of an individual $v^{(i)}$. First, three random individuals $v^{(k)}, v^{(l)}$ and $v^{(n)}$, $k \neq l \neq n$ are chosen at random from the current population. From these three vectors a mutation vector z is constructed:

$$z = v^{(k)} + F(v^{(l)} - v^{(n)}).$$

Here, $F \in \mathbb{R}$ is a scaling factor. A trial vector $\hat{v}^{(i)}$ is constructed, where $\hat{v}_j^{(i)} = z_j$ with probability C_r, or set $\hat{v}_j^{(i)}$ to the old value $\hat{v}_j^{(i)} = v_j^{(i)}$ with probability $1 - C_r$. The parameter $C_r \in [0, 1]$ is called the crossover rate. If $f(\hat{v}^{(i)}) \leq f(v^{(i)})$, the individual $v^{(i)}$ is replaced in the population by $\hat{v}^{(i)}$. The iteration is stopped once a certain stopping criterion is met.

For the DE/1/rand/bin algorithm described above, the parameters N_p, F and C_r must be chosen beforehand. Instead, we employ an adaptive radius-limited DE algorithm as implemented in the Julia library BlackBoxOptim.jl in this chapter, so that these parameter choices are made automatically and dynamically [36]–[38].

4.2.4 Generation of ER networks

We test the optimization of parameters on small artificial ER networks. We now describe the method used for constructing these networks. The nodes of the network are placed in a 4×3 grid and are labelled as seen in Figure 4.11.

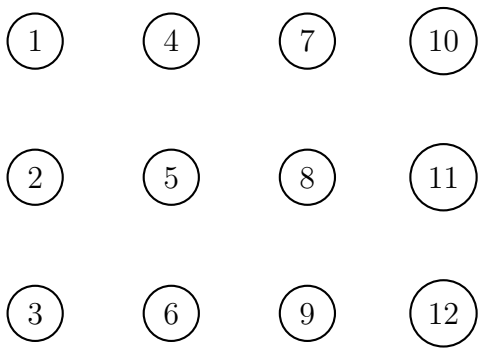

Figure 4.1: Configuration of electrodes.

Connections are added in the following way. A graph where all nodes are connected to their neighbours is first constructed. This is done in order to conform to the conclusions found in Appendix B. Then, each of the edges in this graph is removed with probability 0.3. Finally, between any two nodes, a connection is added with probability 0.15. It is not taken into account whether these connections already exist. This results in an artificial ER network $G = (V, E)$, $|V| = N$. As stimulation pairs, we choose all pairs of adjacent nodes on the rows of the grid shown in Figure 4.11. Hence, nodes 3 and 6, for example, form a stimulation pair, as well as nodes 7 and 10 or nodes 2 and 5. However, nodes 1 and 2, for example, do not form a stimulation pair. In total, we thus have 9 stimulation pairs, given by the set S. Expected ERs can be inferred from the network. Desired DRs are randomly distributed with each response electrode having probability 0.1 of a desired DR.

The constructed network has nodes with degree similar to what is found in ER networks for patients. In the artificial networks, there are fewer ERs than may be expected in a real network. This is due to the method of construction where ERs are inferred from a network without adding connections, instead of generating a sparser network and adding connections based on the stimulation pairs. Lastly, in a real brain network, DRs will not be spread randomly. However, we are not aware of a pattern in the occurrence of DRs that can easily be used for the generation of artificial networks. Hence, the choice for a uniform distribution of DRs was made.

For optimization in patient-specific networks, data was provided by the University Medical Centre Utrecht. Data for the occurrence of ERs for each stimulation pair and scored data for DRs was provided. From the data for the ERs a network is constructed following the method described in 4.2.1. These ERs are also the desired ERs in the network, whereas the desired DRs are directly derived from the scored data for DRs.

4.3 Results

Before moving to the results obtained for fitting parameters in 12-node networks, we first characterize evoked responses in networks of a few nodes, providing intuition for the influence of parameters on the generation of evoked responses. This is interesting as it provides a means to explain the results obtained through optimization of many parameters in larger networks. Specifically, we are interested in the influence of the following parameters on evoked responses:

1. The amount of feedforward inhibition to a node β.
2. The amount of excitatory background input in a node I.
3. The strength of the connection between stimulation pair K_{ff}.

4. The strength of feedback connections K_{rec}.

5. The influence of external constant input, governed by a connectivity K_{ext}.

The first two parameters considered are interesting because they are directly used for fitting parameters in larger networks. By considering the latter three types of connections, we gain an understanding of the influence of different values in the connectivity matrix K.

4.3.1 Primary responses to stimulation

We start by looking at primary responses to stimulation. In this scenario, we have one stimulated electrode that is directly connected to another electrode. Our goal is to find which types of responses can be obtained from such a configuration, and whether added connections or nodes have a significant effect on evoked responses. We begin by considering two nodes with one feedforward connection. A schematic view of the network is given in Figure 4.2. Within this network, we vary β_2, $K^{1,2}$, I_1 and I_2.

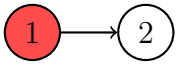

Figure 4.2: Graph with one feedforward connection. A red color indicates stimulation of a neural mass.

We first consider the influence of the excitatory background input on evoked activity. We fix $\beta = 0.7$. Fixing $K^{1,2}$ at several values and varying I_1 and I_2 yields the results seen in Figure 4.4a and 4.4b. Simulations are given in Figure 4.3, showing the characteristic responses obtained in the second neural mass. We see that higher values for the external excitatory input promotes the appearance of early response-like activity. The influence of the external input for the first neural mass on the appearance of ERs disappears for higher values of $K^{1,2}$. Moreover, we find a small band in the parameter plane where both an ER and DR appear. We note that DRs only appear for very high values of I_2.

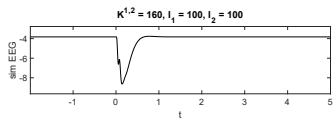

(a) Simulation 1.

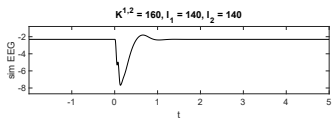

(b) Simulation 2.

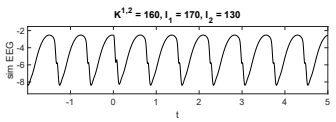

(c) Simulation 3.

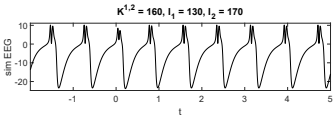

(d) Simulation 4.

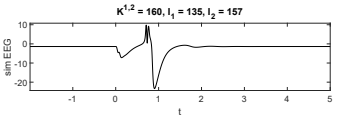

(e) Simulation 5.

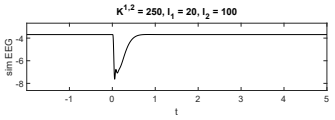

(f) Simulation 6.

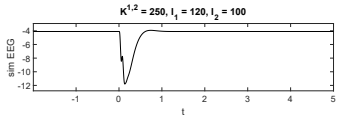

(g) Simulation 7.

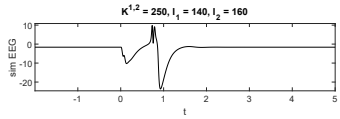

(h) Simulation 8.

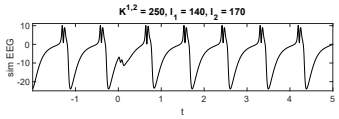

(i) Simulation 9.

Figure 4.3: Simulations corresponding to specific parameter choices in Figure **??**. These simulations show that a variety of characteristic evoked Sresponses may be obtained from the system.

We now investigate the influence of feedforward connections and the amount of feedforward inhibition on primary responses. We thus vary $K^{1,2}$ and β. We first fix $\beta = 0.7$, $I_1 = 140$ and vary $K^{1,2}$ and I_2. Next, we fix $K^{1,2} = 200$, $I_1 = 140$ and vary β and I_2. The results are shown in Figure 4.4c and 4.4d. We see that increasing $K^{1,2}$ and β has a similar effect on the observed evoked activity. Increasing either parameter promotes the appearance of ERs as well as DRs, and a slim band of increasing width where DRs occur is seen for both $K^{1,2}$ and β. A small area where only a DR and no ER occurs is also seen, corresponding to an ER-like response that is too small to be registered as an ER and a DR-like response. We thus find that both the amount of feedforward inhibition and a higher connectivity promote delayed responses.

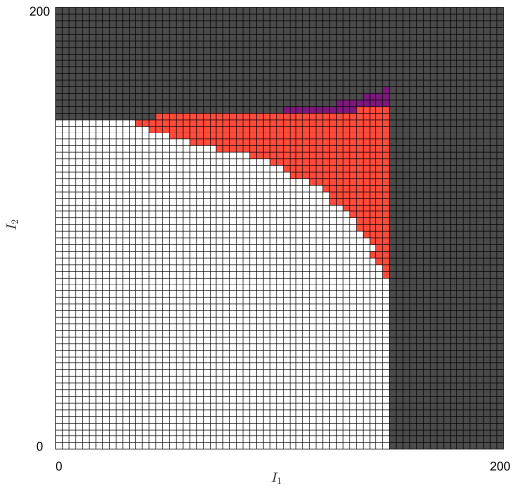

(a) Behaviour for $K^{1,2} = 160$, $\beta = 0.7$.

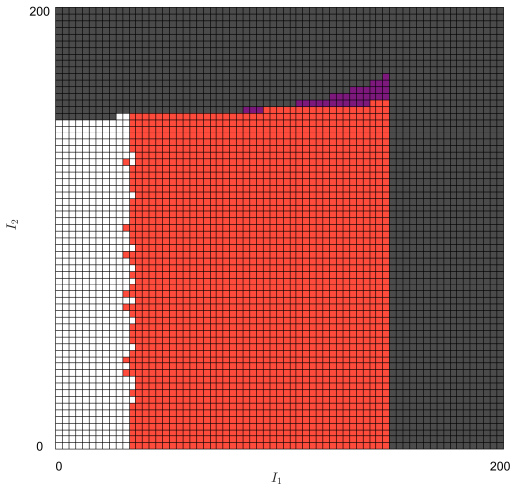

(b) Behaviour for $K^{1,2} = 250$, $\beta = 0.7$.

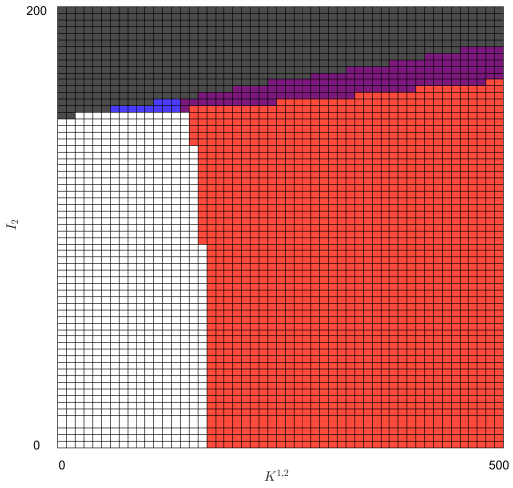

(c) Behaviour for $I_1 = 140$, $\beta = 0.7$.

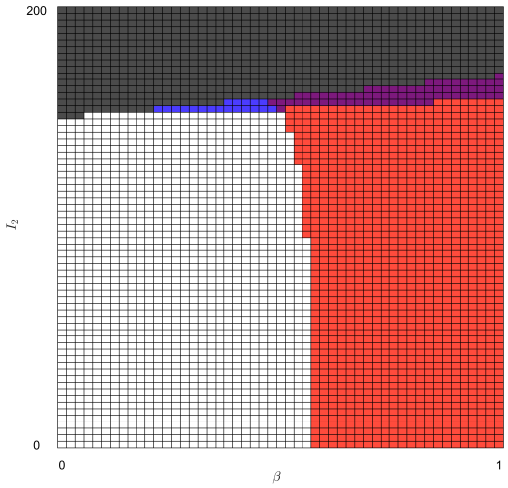

(d) Behaviour for $I_1 = 140$,$K^{1,2} = 250$.

Figure 4.4: Observed evoked activity in node 2 of the network shown in Figure 4.2. Here, **gray** denotes oscillatory behaviour, **white** denotes no significant response, **red** denotes an ER, **blue** denotes a DR and **purple** denotes both an ER and DR.

We now investigate the influence of an added reciprocal connection to the network. The network considered is shown in Figure 4.5.

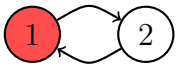

Figure 4.5: Graph with a reciprocal connection. A red color indicates stimulation of a neural mass.

For this network, we aim to find the influence of the added extra reciprocal connection $K^{2,1}$. To do this, we fix $\beta = 0.7$ and look at two cases:

1. We fix $I_1 = 140$ and $I_2 = 160$ and vary both connectivities.
2. We fix $I_1 = 140$ and $K^{1,2} = 300$ and vary $K^{2,1}$ and I_2.

In the first case, we directly compare the influence of both connectivities. In the second case, we choose values for the excitatory background input that have been shown to generate DRs for specific parameter choices in the feedforward case. We are now interested in whether these parameter ranges persist and whether the added reciprocal connection has an effect on the appearance of DRs. The results are shown in Figure 4.6.

In case 1, we find that a larger feedback connection promotes the generation of DR-like responses as well as oscillatory activity. In case 2, we find that a band of DR-like activity

persists for higher values of $K^{2,1}$. This band does become slimmer as $K^{2,1}$ increases. For higher values of $K^{2,1}$ we see that DRs occur for slightly lower values of I_2.

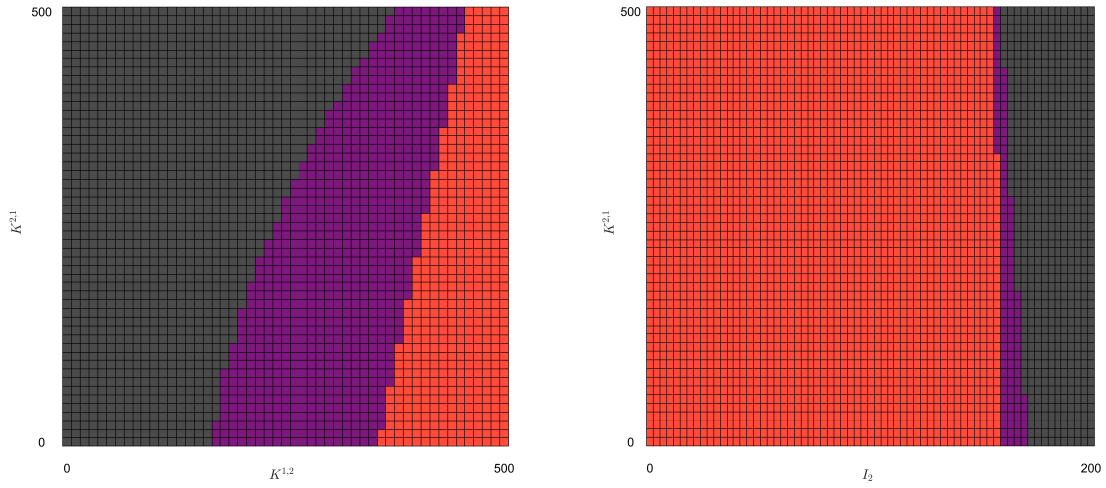

(a) Behaviour for $I_1 = 140$, $I_2 = 160$, $\beta = 0.7$. *(b)* Behaviour for $I_1 = 140$, $K^{1,2} = 300$, $\beta = 0.7$.

Figure 4.6: Observed evoked activity in node 2 of the network shown in Figure 4.5. Here, **gray** denotes oscillatory behaviour, **white** denotes no significant response, **red** denotes an ER, **blue** denotes a DR and **purple** denotes both an ER and DR.

Finally, we look at the case where a second neural mass provides constant external input. Our goal is to investigate the influence of this external constant input. The considered network is shown in Figure 4.7.

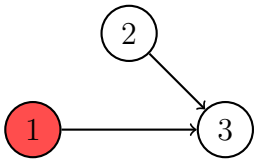

Figure 4.7: Two feedforward coupled NMMs with constant external input. A red color indicates stimulation of a neural mass.

Here, we fix $\beta = 0.7$, $I_1 = 140$, $I_2 = 110$ and $K^{1,3} = 100$ or $K^{1,3} = 200$. We thus vary $K^{2,3}$ and I_3. The results are shown in Figure 4.8. We see that a large external constant input stabilizes the system and DRs cease to exist for very large external input.

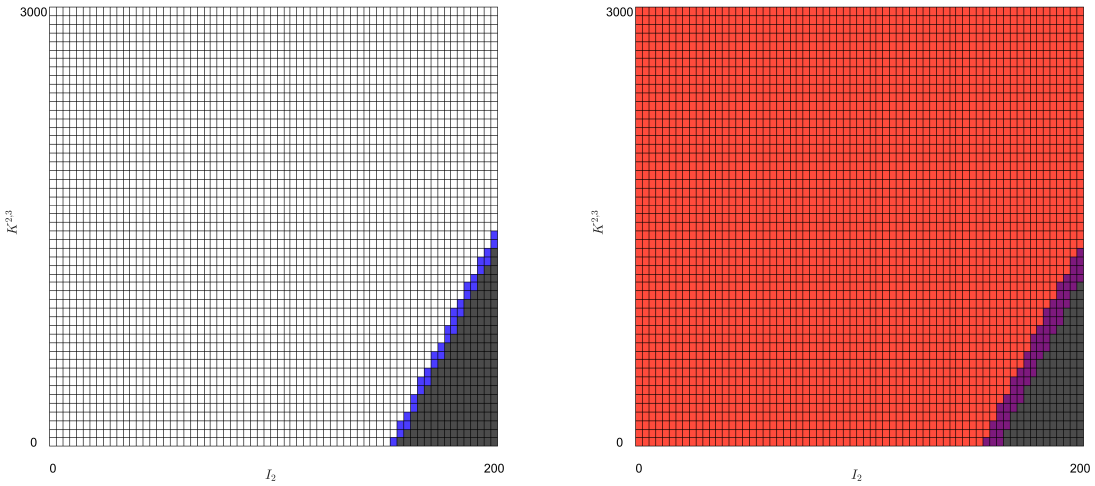

(a) Behaviour for $I_1 = 140$, $I_2 = 110$, $\beta = 0.7$ and $K^{1,3} = 100$.

(b) Behaviour for $I_1 = 140$, $I_2 = 110$, $\beta = 0.7$ and $K^{1,3} = 200$.

Figure 4.8: Observed evoked activity in node 2 of the network shown in Figure 4.7. Here, **gray** denotes oscillatory behaviour, **white** denotes no significant response, **red** denotes an ER, **blue** denotes a DR and **purple** denotes both an ER and DR.

Summarizing our results, we have found that a stronger coupling between stimulation electrode and response electrode promotes the appearance of ERs and DRs in two feedforward coupled neural mass models. Similarly, an increased amount of feedforward inhibition also has a positive effect on the appearance of ERs and DRs. A strong reciprocal connection also promotes the generation of DRs. Finally, external constant inputs stabilize the neural mass, diminishing the probability of the generation of DR-like activity.

4.3.2 Secondary responses to stimulation

We now investigate secondary responses to stimulation, meaning there is no direct connection between the stimulated electrode and the response electrode. Hence, no early response is expected. However, delayed responses may occur in these electrodes. We again investigate the influence of the parameters introduced at the start of this section.

We first consider a network with two feedforward connections. The network is given in Figure 4.9.

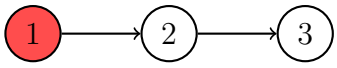

Figure 4.9: Graph with two feedforward connections. A red color indicates stimulation of a neural mass.

We fix $I_1 = 110$, $K^{1,2} = 250$ and I_2 and vary $K^{2,3}$ and I_3. Moreover, we set $\beta_1 = \beta_2 = \beta_3 = 0.7$. This yields the results shown in Figure 4.12a and 4.12b. We see that, as desired, no early responses occur. A parameter range does exist where delayed responses are seen. We have found that an increase of $K^{2,3}$ promotes the appearance of DR-like responses in the third neural mass. Moreover, we again see that delayed responses only occur for high values of I_3, hence signifying a positive relation between the value of I_3 and the generation of delayed responses. We note that the network in Figure 4.9 is considered by Hebbink et al. in [6]. Moreover, a network with an added connection from node 1 to node 3 is also considered in [6].

In order to quantify the influence of feedforward inhibition on the activity observed in the third neural mass, we now fix $K^{2,3} = 300$ and instead vary β_3 and I_3. This yields the result shown in Figure 4.12c. We here see that a larger amount of feedforward inhibition β_3 has a positive effect on the appearance of DRs in the network shown in Figure 4.9.
We now investigate whether a reciprocal connection between nodes 2 and 3 in the feedforward network in Figure 4.9 affects the obtained responses. The new considered network is shown in Figure 4.10.

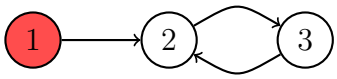

Figure 4.10: Graph with a feedforward connection and a reciprocal connection. A red color indicates stimulation of a neural mass.

For this network, we fix $K^{1,2} = 250$, $I_1 = 110$, $I_2 = 150$ and $I_3 = 155$. We then vary the connection strengths $K^{2,3}$ and $K^{3,2}$. This yields the results shown in Figure 4.12d. We here see that a reciprocal connection can both promote and abolish DR-like activity.

Finally, we look at a case where a constant external input is present for the response electrode.

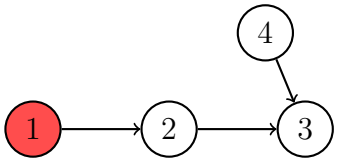

Figure 4.11: Graph with two feedforward connections and an external input. A red color indicates stimulation of a neural mass.

We fix $I_1 = 110$, $I_2 = 150$, $I_4 = 110$, $K^{1,2} = 250$, $K^{2,3} = 300$ and $\beta_i = 0.7$ for $i \in \{1, 2, 3, 4\}$. We then vary I_3 and $K^{4,3}$. The result is shown in Figure 4.12e. In

our simulations, we see an effect of external input similar to what is seen in the case of primary responses, namely that an increased external input stabilizes the system and impairs the appearance of DRs in neural mass 3. Summarizing our results, we find that various parameters have a significant effect on the appearance of responses resembling ERs and DRs in small networks of neural mass models. Namely, an increased external excitatory input, the amount of feedforward inhibition and strength of feedforward connections to the response electrode all promote the generation of ERs. Increasing these parameters also promotes the generation of DRs both as a primary and secondary response. The influence of an increased reciprocal connection is seen to be positive for the generation of DRs if a direct connection exists between the stimulation and response electrode and negative otherwise. Finally, external constant input diminishes the probability of the generation of a DR, both for primary and secondary responses. We note that the findings in this chapter only cover a small part of the possible parameter space and thus the conclusions obtained here cannot be extended to other parts of the parameter space. We do believe that in this section, a representative and interesting part of the parameter space is considered. The reason for this is that parameter choices in larger systems are chosen at parameter choices of smaller systems where interesting behaviour (generation of ERs and DRs) is seen. A summary of the findings from this section and the previous section is given in Table 4.2.

Table 4.2: Influence of model parameters on the generation of evoked responses as observed in small networks. Here, a $+$ means that increasing a parameter promotes the generation of the particular response, whereas a $-$ means that increasing a parameter diminishes the probability of generating a response.

Response $\rightarrow$	First order		Second order
Parameter $\downarrow$	ER	DR	DR
I_{resp}	$+$	$+$	$+$
β_{resp}	$+$	$+$	$+$
K_{ff}	$+$	$+$	$+$
K_{rec}	None	$+$	-
K_{ext}	None	-	-

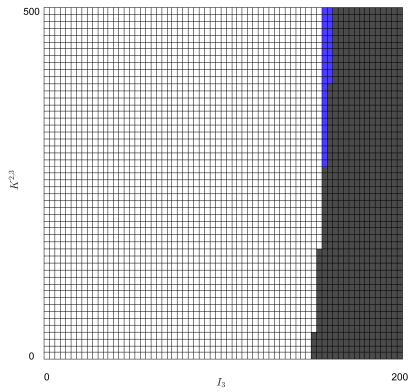

(a) Behaviour for $I_2 = 110$ and $\beta = 0.7$.

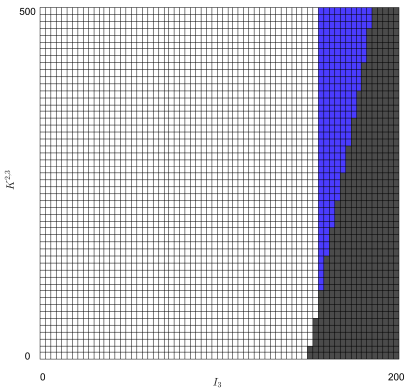

(b) Behaviour for $I_2 = 150$ and $\beta = 0.7$.

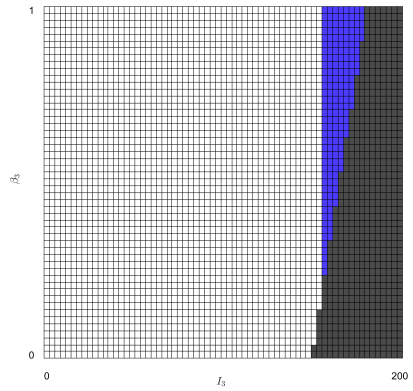

(c) Behaviour for $I_2 = 110$ and $K^{2,3} = 300$.

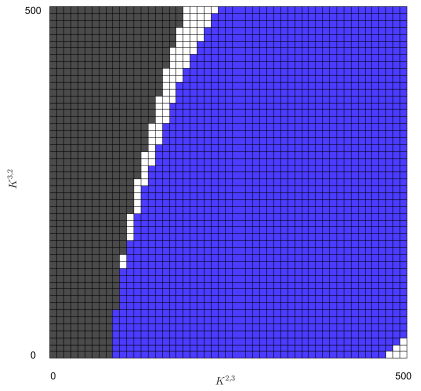

(d) Behaviour for $K^{1,2} = 250$, $I_1 = 110$, $I_2 = 150$ and $I_3 = 155$.

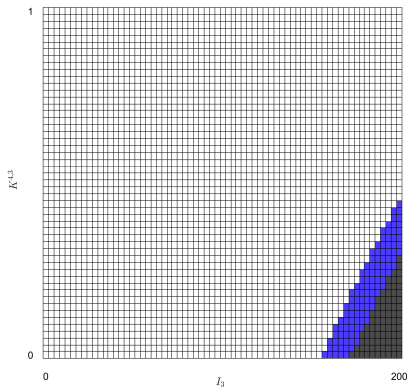

(e) Behaviour for $I_1 = 110$, $I_2 = 150$, $I_4 = 110$, $K^{1,2} = 250$, $K^{2,3} = 300$ and $\beta = 0.7$.

Figure 4.12: Observed evoked activity in node 2 of the network shown in Figure 4.9. Here, **gray** denotes oscillatory behaviour, **white** denotes no significant response, **red** denotes an ER, **blue** denotes a DR and **purple** denotes both an ER and DR.

4.3.3 Fitting ERs and DRs in 12-node networks

In the previous Section, we have investigated the influence of various parameter choices on the evoked activity in small networks of neural mass models. We are now interested in fitting I, β and K to fit responses in larger networks of neural mass models. To do this, we first generate ten sample networks following the procedure described in Section 4.2.4. The adjacency matrices for the 10 generated networks are provided in Figure 4.13. The desired early and delayed responses for each of the ten artificial networks are given in Figure 4.14.

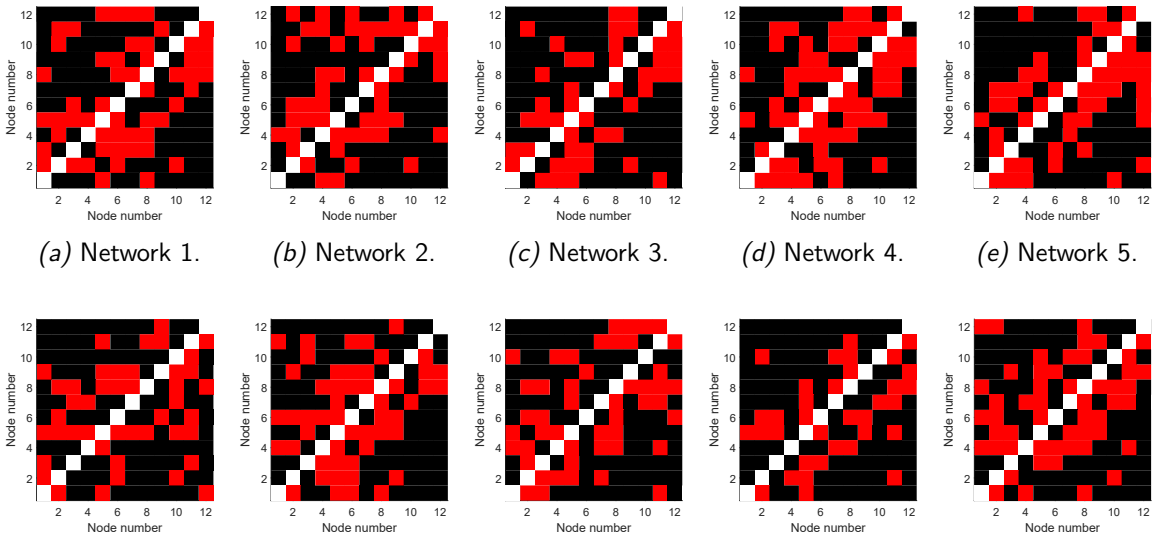

(a) Network 1. *(b)* Network 2. *(c)* Network 3. *(d)* Network 4. *(e)* Network 5.

(f) Network 6. *(g)* Network 7. *(h)* Network 8. *(i)* Network 9. *(j)* Network 10.

Figure 4.13: Visualization of the adjacency matrices for the used 12-node networks. If the square at row i and column j is **black**, $A_{ij} = 0$ and if the square is **red**, $A_{ij} = 1$. Connections from node i to itself are kept **white**, as no self-loops exist in the network.

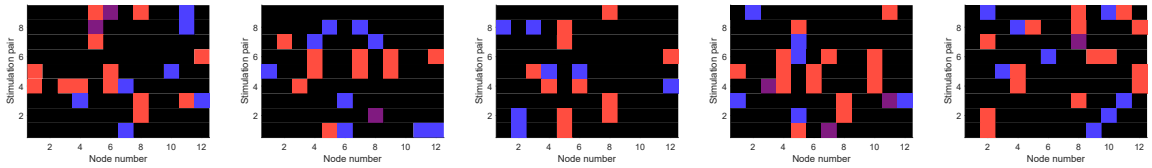

(a) Network 1. *(b)* Network 2. *(c)* Network 3. *(d)* Network 4. *(e)* Network 5.

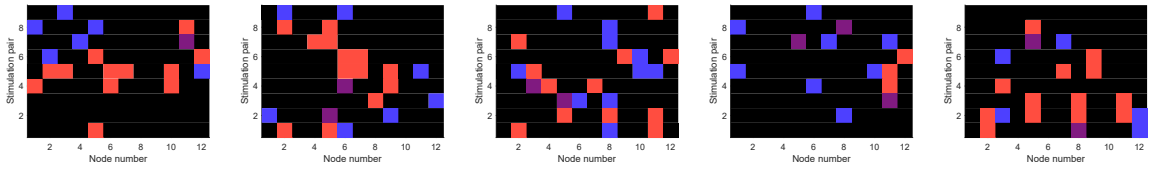

(f) Network 6. *(g)* Network 7. *(h)* Network 8. *(i)* Network 9. *(j)* Network 10.

Figure 4.14: Desired ERs and DRs for all used 12-node networks. Here, **black** indicates no ER or DR, **red** indicates an ER, **blue** indicates a DR and **purple** indicates both an ER and DR.

We fit parameters in this network using a differential evolution (DE) algorithm as described in Section 4.2.3, with the fitness function in Equation 4.2. Simulations needed for the evaluation of the loss function are performed using forward Euler with a time step of 0.003 s. The responses resulting from the best found parameters are shown in Figure 4.15. Statistics of the fitted responses are shown in Table 4.3.

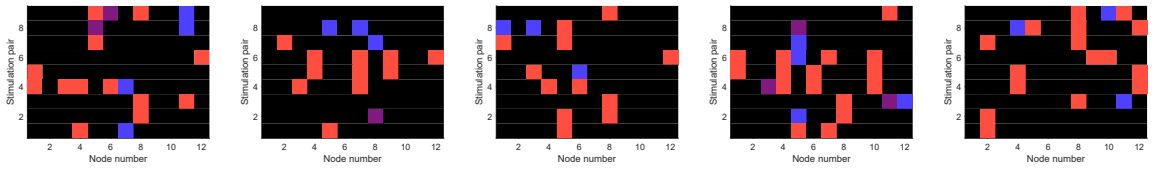

(a) Network 1. *(b)* Network 2. *(c)* Network 3. *(d)* Network 4. *(e)* Network 5.

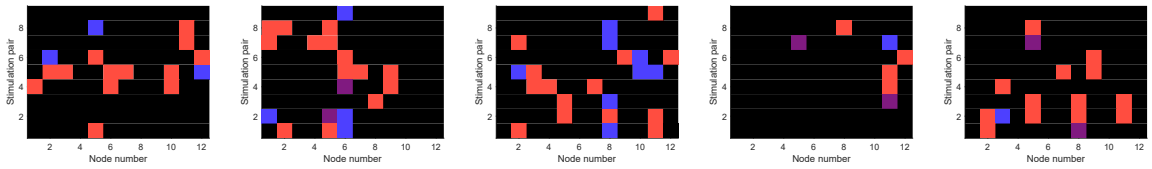

(f) Network 6. *(g)* Network 7. *(h)* Network 8. *(i)* Network 9. *(j)* Network 10.

Figure 4.15: Found ERs and DRs for all used 12-node networks. Here, **black** indicates no ER or DR, **red** indicates an ER, **blue** indicates a DR and **purple** indicates both an ER and DR.

Table 4.3: Results for fitting ERs and DRs in ten 12-node artificial networks. Here, the data in the column #Conn gives the amount of connections of the network. The data in the columns #Found are the amount of found desired responses. The columns #Desired give the amount of desired responses. Lastly, the columns #False give the amount of additional unwanted responses that are found.

	ERs			DRs		
	#Found	#Desired	#False	#Found	#Desired	#False
Network 1	14	15	1	6	9	0
Network 2	11	11	1	4	10	0
Network 3	11	11	1	3	7	0
Network 4	18	18	1	6	9	1
Network 5	16	16	0	3	9	0
Network 6	13	13	0	3	7	0
Network 7	14	15	2	5	9	1
Network 8	14	14	0	8	12	0
Network 9	6	6	0	3	11	0
Network 10	15	15	0	3	7	0

Before we consider the results obtained from optimization in more detail, we first provide a simulation for network 1, showing the simulated ECoG signal and evoked responses after optimization. The network contains 53 connections and 12 nodes, yielding a total of 77 parameters (53+12+12). After 229,200 steps and 229,311 loss function evaluations in our DE algorithm, the algorithm converges to a loss of 31. When inspecting the results, we find that this value stems from three DRs and one ER that were not found. Hence, using this method it was possible to correctly fit all but one of the desired ERs and a majority of the desired DRs (6/9). Results for all stimulation pairs are given in Figure 4.16.

In the simulations in 4.16, the results for the fitted ERs generally coincide with what is desired. All desired ERs are clearly seen in the simulations. Apart from node 4 for stimulation pair 1, where a faulty ER is found, there are several more cases where an ER-like response is seen in nodes that should not show ERs. These cases are seen mostly for stimulation pairs 1, 5 and 7. This can be attributed to the threshold value used for detecting ERs. These ER-like responses have an amplitude smaller than 5 and are thus disregarded when detecting ERs.

When looking at the fitted DRs, we find that no undesired DRs occur shortly after stimulation. For stimulation pairs 3 and 5, three expected DRs are not seen in simulations. In stimulation pair 8, we see that the occurrence of two DRs causes two other DR-like responses at a later time. These responses were not measured when evaluating the loss

function, and thus did not influence results.

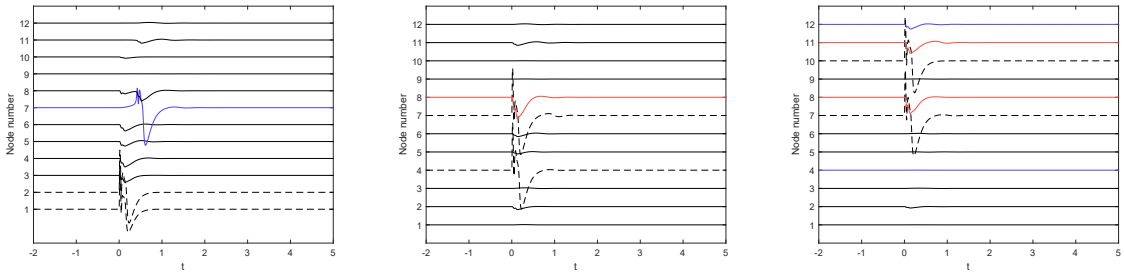

(a) Results for stimulation pair 1. *(b)* Results for stimulation pair 2. *(c)* Results for stimulation pair 3.

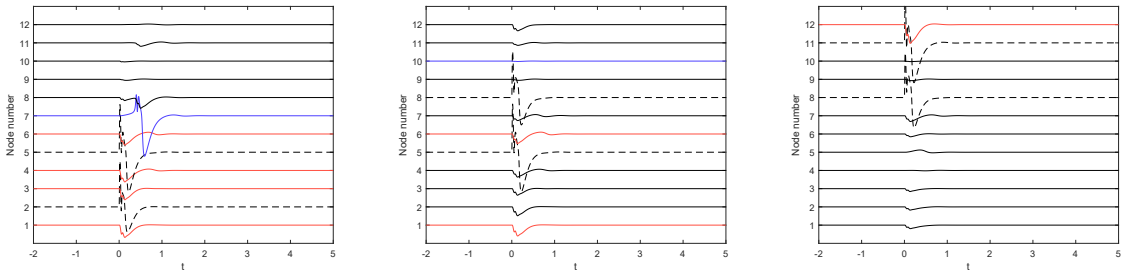

(d) Results for stimulation pair 4. *(e)* Results for stimulation pair 5. *(f)* Results for stimulation pair 6.

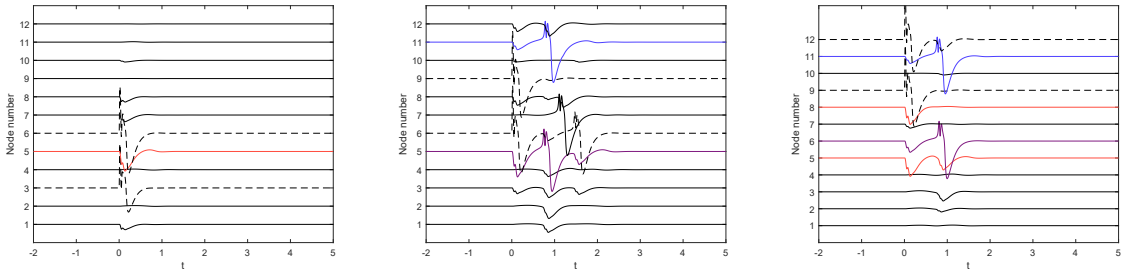

(g) Results for stimulation pair 7. *(h)* Results for stimulation pair 8. *(i)* Results for stimulation pair 9.

Figure 4.16: Results from simulation of all stimulation pairs of the generated artificial small network with the best found parameters. The stimulation pair is stimulated at $t = 0$. In these simulations, a **dashed** line indicates that a channel is stimulated. A **red** line indicates that an ER is expected. A **blue** line indicates that a DR is expected. A **purple** line indicates that both an ER and a DR are expected for this channel.

Our results show that fitting ERs works very well, as for most networks all ERs are found and few extra ERs are found. Around half of the total desired DRs are found. These results show that varying K, I and β can introduce sufficient heterogeneity in the network so that a majority of evoked responses is found as desired, despite performing stimulation from different nodes in a network with the same parameters. As only part of the delayed responses is found correctly, we now compare nodes where a DR is correctly found to nodes

where a desired DR is not found. We compare network structure and parameter choices to gain insight in what parameters are important for determining whether a DR is found.

First, we have considered the distance between stimulation pair and response electrode. If the electrode where a DR is desired is further away from the stimulation electrode, it may be harder to correctly fit parameters in order to generate a delayed response. A comparison of the distance between stimulation electrode and response electrode for found DRs and unfound DRs using a Mann-Whitney U test (at a significance level of $\alpha = 5\%$) yielded that there is a significant difference between the two groups ($p = 2.0060 \times 10^{-5}$). A majority of the correctly fitted DRs are at distance 1 from the stimulation electrode. Moreover, no DRs are fitted correctly at distance 3 or more from the stimulation electrode. A majority of all desired DRs at distance 1 from the stimulation electrode are found (66.07%). Of the desired DRs at distance 2 from the stimulation electrode, 24.14% are correctly fitted. In total, 48.89% of the desired DRs are fitted correctly in our ten artificial networks. We note that in networks derived from SPES measurements in patients with epilepsy, DRs are rarely seen at distance 3 or more from the stimulation pair [6].

To further look into the influence of connectivity, we investigate whether the percentage of incoming connections that show an ER and the percentage of connections that are bidirectional are significantly different between found DRs and unfound DRs. Once again, we use a Mann-Whitney U test at a significance level of $\alpha = 5\%$. We find that both the percentage of incoming connections with an ER ($p = 0.1810$) and the amount of bidirectional connections ($p = 0.2890$) are not significant for explaining whether DRs are found or not found in our optimization.

In order to investigate the influence of the feedforward inhibition β on the results of our optimization, we perform another Mann-Whitney U test ($\alpha = 5\%$). We find that the amount of feedforward inhibition is significantly different in nodes where a DR is correctly found ($p = 3.7647 \times 10^{-4}$). This is in agreement with the analysis in Sections 4.3.1 and 4.3.2, where it is found that an increased amount of feedforward inhibition promotes the generation of DRs, both for primary and for secondary responses. Boxplots showing the amount of feedforward inhibition for found and unfound DRs is shown in Figure 4.17a. Finally, we investigate the influence of the amount of excitatory background input on whether DRs are correctly found. We find, once again using a Mann-Whitney U test ($\alpha = 0.05$) that there is a significant relation between the amount of background input and whether a DR is correctly found ($p = 2.5033 \times 10^{-12}$). This is again in line with the results found in Sections 4.3.1 and 4.3.2, where it is found that DRs can only occur for high values of I in the response electrode. A boxplot is given in Figure 4.17b. A few outliers are present in this boxplot. These cases may be explained by the appearance of an ER-like response that

occurs later after stimulation. These responses are caused by DRs in other nodes of the network. Our analysis suggests that it is only possible to take the excitatory background input high for a few nodes to avoid oscillatory behaviour. If I is taken to be lower, no delayed responses can generically be found. This may be attributed to the equilibrium then being situated on a lower branch of equilibria.

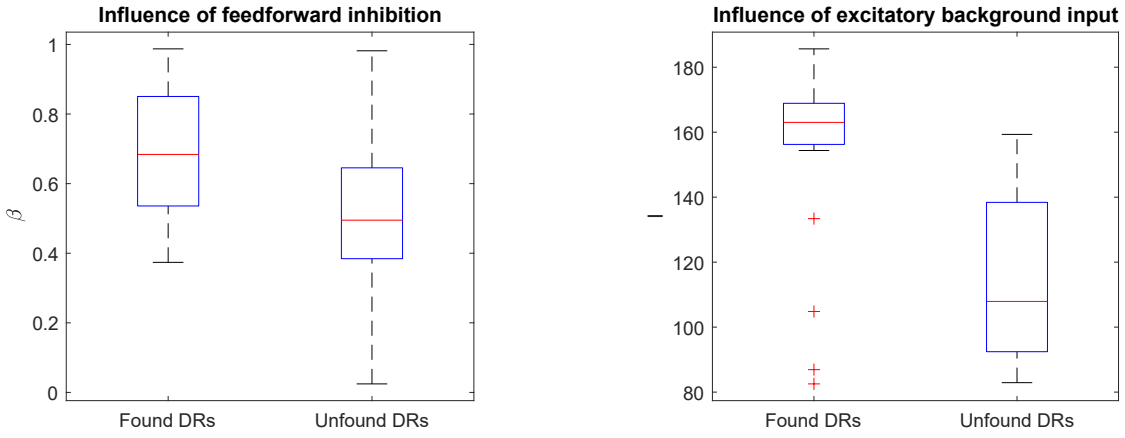

(a) *(b)*

Figure 4.17: Boxplots showing the relation between the values of parameters in the network and desired DRs that are found and not found after fitting these parameters.

4.3.4 Fitting ERs and DRs in networks derived from clinical data

We now consider the application of our DE algorithm to clinical data derived from measurements done for patients treated at the University Medical Centre Utrecht. Single pulse electrical stimulation measurements are used for four patients, and a network of neural mass models with connections based on the ER networks for these patients are used. The differential evolution algorithm was allowed to run for a range between 60000 to 75000 steps before optimization was stopped. For the evaluation of the loss function, forward Euler with a timestep of 0.005 s was used for simulations. The algorithm was not stopped because the DE algorithm converged, but rather because the evaluation of the loss function was too slow to warrant the continuation of running the code. Hence, better results could be obtained if the DE algorithm is run for more steps.

The results, given in Table 4.4, show that within networks derived from clinical data, it is possible to correctly fit a large majority of all ERs. Moreover, it is seen to be possible to correctly fit a few DRs in three of the four networks, without introducing oscillatory behaviour or a large amount of additional unwanted DRs.

Table 4.4: Results for fitting ERs and DRs in networks derived from clinical data using a differential evolution algorithm. Here, the data in the column #Conn gives the amount of connections of the network. The data in the columns #Found are the amount of found desired responses. The columns #Desired give the amount of desired responses. Lastly, the columns #False give the amount of additional unwanted responses that are found.

	#Conn	ERs			DRs		
		#Found	#Desired	#False	#Found	#Desired	#False
Patient 1	1047	697	701	28	0	313	0
Patient 2	920	613	624	39	1	247	0
Patient 3	464	281	292	14	7	251	1
Patient 4	1043	646	663	46	10	589	1

Finally, we give an example of a simulation for one of the stimulation pairs for the neural mass network derived for the data of Patient 4. This stimulation pair is picked because it shows the generation of ERs and DRs in the network. The simulation is shown in Figure 4.18. We note that a few unwanted additional ERs are found for nodes 2, 22 and 23.

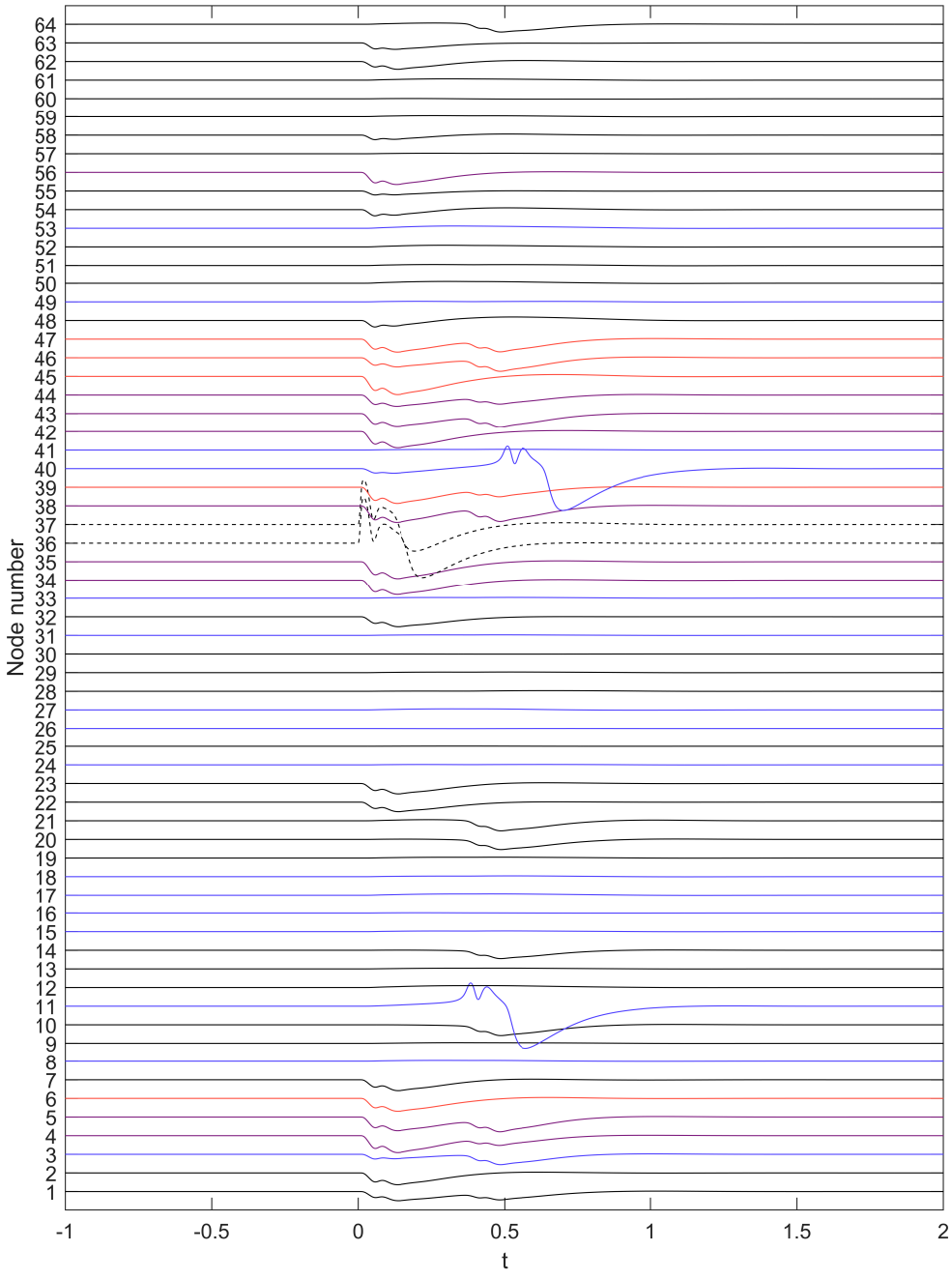

Figure 4.18: Simulation for one of the stimulation pairs for Patient 4, showing the generation of ERs and DRs in networks derived from clinical data. The stimulation pair is stimulated at $t = 0$. In this simulation, a **dashed** line indicates that a channel is stimulated. A **red** line indicates that an ER is expected. A **blue** line indicates that a DR is expected. A **purple** line indicates that both an ER and a DR are expected for this channel.

4.4 Conclusions

In this chapter, we have investigated evoked activity in small networks of neural masses. We have first looked at small networks before presenting results for the optimization of parameters in a network of 12 nodes.

Through simulations in tiny networks of up to three nodes, we have gained insight into evoked activity generated in coupled Wendling neural masses. We have seen that a higher connectivity and increased amount of feedforward inhibition between stimulation electrode and response electrode promotes the appearance of ERs and DRs. We have also found that a stronger reciprocal connection between stimulation electrode and response electrode promotes the appearance of DR-like responses. Lastly, we have found that high external input stabilizes the system.

In ten artificial 12-node networks, we have optimized parameter choices for the connectivity, external excitatory input and amount of feedforward inhibition using a differential evolution algorithm. These artificial networks have limitations and thus may include physiologically impossible desired responses. Through the optimization of parameter choices, we were able to simulate most desired ERs and part of the desired DRs, while generating few additional evoked responses. Moreover, we have found that almost all desired ERs and some desired DRs can be found through optimization of parameters in patient-specific networks of neural mass models. The results in this chapter show that it is possible to introduce sufficient heterogeneity in a network of neural mass models to model desired evoked responses that are distinct per stimulation pair. This is promising for the use of networks of neural mass models to explain clinical data and predict the outcome of epilepsy surgery. An analysis of our results for the ten 12-node networks reveals that a majority of delayed responses at distance 1 from a stimulation electrode could be fitted correctly, whereas responses far from a stimulation electrode are more difficult to obtain. We have also found that the amount of feedforward inhibition and the amount of excitatory background input are statistically important for explaining why certain DRs were found and others were not.

Chapter 5

Conclusions and discussion

In this thesis, we have investigated the influence of feedforward inhibition on the spontaneous activity of two reciprocally coupled neural mass models. Moreover, we have investigated evoked activity in small networks of neural mass models. We first present the main conclusions from our analysis. Afterwards, we discuss our results and provide an outlook to further work.

5.1 Conclusions

In our investigation of spontaneous activity in two coupled neural mass models through bifurcation analysis, we have found that feedforward inhibition has a significant influence on the appearance of activity associated with epilepsy in coupled neural mass models. This is seen both in two coupled Jansen-Rit models as well as in coupled Wendling models. The feedforward inhibition necessary for modelling delayed responses also promotes spike-wave-discharges (SWD) in neural mass models. Our finding is in accordance with the view of delayed responses as a biomarker for the epileptogenic cortex and thus for the region where seizures originate [9]. We have found that synchronous SWDs occur in a larger part of the parameter space for two coupled Wendling models with stronger connections, when compared to Jansen-Rit models with weaker connections. We have seen that a stronger reciprocal connection significantly affects the region in which simultaneous spiking is seen for two neural mass models. Finally, we find various possible pathways in our bifurcation analysis to SWD activity.

When considering evoked activity in networks of neural mass models, we have mapped the influence of several parameters on the generation of evoked responses in networks of Wendling neural masses of up to four nodes. We have then shown using a differential evolution algorithm that it is possible to model ERs and DRs in a network of 12 coupled Wendling neural masses, when only controlling connectivities, the amount of feedforward

inhibition and the amount of external excitatory input. Almost all desired ERs could be modelled correctly. Desired DRs that were further away from the stimulation electrodes were found only in some cases. However, desired DRs with a direct incoming connection from a stimulated electrode could be modelled correctly in a majority of the cases. Finally, we considered the application of our DE algorithm to clinical data provided by the University Medical Centre Utrecht. We have found that most of the desired ERs and a few desired DRs can be found through optimization of parameters in these patient-specific networks of neural mass models.

The findings in this thesis provide a promising outlook for the usage of neural mass models in epilepsy research. Our analysis of evoked activity shows that responses observed in SPES can be modelled in networks of Wendling neural masses, which is an essential step towards the creation of patient-specific neural mass models. Such models may eventually be used in the prediction of surgery outcome for epilepsy patients. Moreover, our analysis of reciprocally coupled neural mass models shows that the feedforward inhibition necessary for modelling delayed responses in neural mass models has a significant effect on the spontaneous activity of coupled neural mass models. This provides a theoretical link between the modelling of evoked activity in SPES and spontaneous activity associated with epilepsy.

5.2 Discussion and limitations

In our analysis of two reciprocally coupled neural mass models, we have highlighted a role for the connection strength in explaining synchronous SWD-like behaviour for the two considered neural mass models. However, the influence of connectivity in combination with feedforward inhibition on spontaneous activity of neural mass models could be investigated in more detail. Namely, in literature it is shown that the seizure-onset zone and resected area for patients correlate with a high in-degree and out-degree in ER networks [4]. It would be interesting to investigate whether these experimental findings can be explained through the analysis of networks of neural mass models. We note that some analysis does exist for the connectivity between coupled Jansen-Rit models [28], [29]. However, these publications do not consider the link to evoked activity nor the influence of feedforward inhibition.

Moreover, more work could be done comparing the use of the Jansen-Rit and Wendling model in the explanation of seizures. In our analysis, a weaker connection strength is considered in the Jansen-Rit model than in the Wendling model. It can be concluded from our analysis that the Wendling model with larger connectivity and a larger influence of the fast inhibition is preferred for explaining seizures. However, a direct comparison between the two models cannot be made with the analysis provided in this thesis.

The method of constructing 12-node sample networks in our analysis of evoked responses should be discussed. Firstly, we infer what ERs occur from a network assumed to be the true network. Only if both stimulation electrodes have an outgoing connection to another node, a desired ER is added. Adding connections if at least one node in the stimulation pair shows a true connection to another node would be more true to the way in which real ER networks are constructed. This method would likely lead to more ERs in the data set. Delayed responses are distributed randomly over the network. While this method of distributing DRs in theory should provide a large variety of configurations, it is not true to any patterns found in delayed responses in patients. Hence, more work could be done to construct artificial networks that are more true to clinical data.

In the analysis of our results of the optimization of parameters for fitting ERs and DRs, we have found that the found parameter choices are sometimes not numerically stable, meaning that an adjustment of the used ODE solver may remove or add a few early or delayed responses to the outcome of a simulation. Moreover, in a model that can be applied to clinical data it is desired that a part of the brain can be removed, simulating resection in epilepsy surgery. The removal of a few nodes in the neural mass model should thus generally still result in stability. By stability we mean that each neural mass should still converge to a stable equilibrium in absence of stimulation. In the current solutions found through our DE algorithm, numerical experiments show that this is generally not the case, and the system often tends to oscillatory activity with large amplitude upon the removal of a node. Hence, the necessity of stability upon the removal of nodes in the network provides extra conditions that results of parameter optimization should meet.

When fitting ERs and DRs using our DE algorithm, searching in a different parameter space may be better for obtaining correct responses. For example, it may be more physically accurate to view the feedforward inhibition as a characteristic of each specific connection rather than of each node. A numerical experiment with one of our 12-node networks and feedforward inhibition per connection did not yield significantly better results, but this may not be the case in patient-specific networks.

5.3 Outlook

The results in this thesis provide a small step towards the construction of patient-specific neural mass models that can assist in the delineation of epileptiform tissue and improve epilepsy surgery. There are various directions in which future research can be taken.

First, there are still future steps that can be taken to improve patient-specific models show-

ing desired ERs and DRs. As only a few DRs could be fitted correctly in large networks, it is interesting to investigate whether methods can be constructed by which more DRs can be found. Moreover, some conditions for stability after the removal of nodes in the network should be met in patient-specific networks. A possible method of improving parameter optimisation is to incorporate knowledge of evoked activity in small networks of neural mass models to improve the search space and rate of convergence of optimization methods. An alteration of the parameter search space as discussed in the previous section could also be considered.

Another step would be to model seizures in networks of neural mass models that also show characteristic evoked responses. In literature, the influence of network structure on seizure generation in Wendling neural mass models has been studied using a metric for the ictogenicity of nodes in the network [39], [40]. In these models, parameter choices for each node are the same. It would be interesting to investigate networks of neural masses with patient-specific parameter choices per node. Such research would be a next step towards more accurate prediction of surgery outcome for patients with epilepsy.

Bibliography

[1] G. S. Bell, A. Neligan, and J. W. Sander, "An unknown quantity—the worldwide prevalence of epilepsy," *Epilepsia*, vol. 55, no. 7, pp. 958–962, 2014.

[2] H. J. Lamberink, K. Boshuisen, P. C. van Rijen, P. H. Gosselaar, K. P. Braun, and D. C. E. S. P. (DCESP), "Changing profiles of pediatric epilepsy surgery candidates over time: A nationwide single-center experience from 1990 to 2011," *Epilepsia*, vol. 56, no. 5, pp. 717–725, 2015.

[3] J. Engel Jr, P. M. Thompson, J. M. Stern, R. J. Staba, A. Bragin, and I. Mody, "Connectomics and epilepsy," *Current opinion in neurology*, vol. 26, no. 2, p. 186, 2013.

[4] D. van Blooijs, F. S. Leijten, P. C. van Rijen, H. G. E. Meijer, and G. J. Huiskamp, "Evoked directional network characteristics of epileptogenic tissue derived from single pulse electrical stimulation," *Human brain mapping*, vol. 39, no. 11, pp. 4611–4622, 2018.

[5] A. Valentín, G. Alarcón, M. Honavar, J. J. G. Seoane, R. P. Selway, C. E. Polkey, and C. D. Binnie, "Single pulse electrical stimulation for identification of structural abnormalities and prediction of seizure outcome after epilepsy surgery: a prospective study," *The Lancet Neurology*, vol. 4, no. 11, pp. 718–726, 2005.

[6] J. Hebbink, G. Huiskamp, S. A. van Gils, F. S. Leijten, and H. G. E. Meijer, "Pathological responses to single-pulse electrical stimuli in epilepsy: The role of feedforward inhibition," *European journal of neuroscience*, vol. 51, no. 4, pp. 1122–1136, 2020.

[7] M. Lacruz, J. Garcia Seoane, A. Valentin, R. Selway, and G. Alarcon, "Frontal and temporal functional connections of the living human brain," *European Journal of Neuroscience*, vol. 26, no. 5, pp. 1357–1370, 2007.

[8] R. Matsumoto, T. Kunieda, and D. Nair, "Single pulse electrical stimulation to probe functional and pathological connectivity in epilepsy," *Seizure*, vol. 44, pp. 27–36, 2017.

[9] A. Valentin, R. Arunachalam, A. Mesquita-Rodrigues, J. J. Garcia Seoane, M. P. Richardson, K. R. Mills, and G. Alarcon, "Late EEG responses triggered by transcranial

magnetic stimulation (TMS) in the evaluation of focal epilepsy," *Epilepsia*, vol. 49, no. 3, pp. 470–480, 2008.

[10] G. Alarcón, D. Jiménez-Jiménez, A. Valentín, and D. Martín-López, "Characterizing EEG cortical dynamics and connectivity with responses to single pulse electrical stimulation (SPES)," *International journal of neural systems*, vol. 28, no. 06, p. 1750057, 2018.

[11] A. Valentin, M. Anderson, G. Alarcon, J. G. Seoane, R. Selway, C. Binnie, and C. Polkey, "Responses to single pulse electrical stimulation identify epileptogenesis in the human brain in vivo," *Brain*, vol. 125, no. 8, pp. 1709–1718, 2002.

[12] V. B. Mountcastle, "Modality and topographic properties of single neurons of cat's somatic sensory cortex," *Journal of neurophysiology*, vol. 20, no. 4, pp. 408–434, 1957.

[13] B. H. Jansen and V. G. Rit, "Electroencephalogram and visual evoked potential generation in a mathematical model of coupled cortical columns," *Biological cybernetics*, vol. 73, no. 4, pp. 357–366, 1995.

[14] F. Wendling, F. Bartolomei, J. Bellanger, and P. Chauvel, "Epileptic fast activity can be explained by a model of impaired gabaergic dendritic inhibition," *European Journal of Neuroscience*, vol. 15, no. 9, pp. 1499–1508, 2002.

[15] T. L. Eissa, K. Dijkstra, C. Brune, R. G. Emerson, M. J. van Putten, R. R. Goodman, G. M. McKhann, C. A. Schevon, W. van Drongelen, and S. A. van Gils, "Cross-scale effects of neural interactions during human neocortical seizure activity," *Proceedings of the National Academy of Sciences*, vol. 114, no. 40, pp. 10 761–10 766, 2017.

[16] O. N. Markand, "Slow spike-wave activity in eeg and associated clinical features: Often called'lennox'or'lennox-gastaut'syndrome," *Neurology*, vol. 27, no. 8, pp. 746–746, 1977.

[17] J. Terlau, J.-W. Yang, Z. Khastkhodaei, T. Seidenbecher, H. J. Luhmann, H.-C. Pape, and A. Lüttjohann, "Spike-wave discharges in absence epilepsy: segregation of electrographic components reveals distinct pathways of seizure activity," *The Journal of physiology*, vol. 598, no. 12, pp. 2397–2414, 2020.

[18] Y. Yamatogi and S. Ohtahara, "Severe epilepsy with multiple independent spike foci," *Journal of clinical neurophysiology*, vol. 20, no. 6, pp. 442–448, 2003.

[19] F. L. Da Silva, A. Hoeks, H. Smits, and L. Zetterberg, "Model of brain rhythmic activity," *Kybernetik*, vol. 15, no. 1, pp. 27–37, 1974.

[20] F. Grimbert and O. Faugeras, "Bifurcation analysis of jansen's neural mass model," *Neural computation*, vol. 18, no. 12, pp. 3052–3068, 2006.

[21] L. A. Ferrat, M. Goodfellow, and J. R. Terry, "Classifying dynamic transitions in high dimensional neural mass models: A random forest approach," *PLoS computational biology*, vol. 14, no. 3, p. e1006009, 2018.

[22] A. Dhooge, W. Govaerts, Y. A. Kuznetsov, H. G. E. Meijer, and B. Sautois, "New features of the software matcont for bifurcation analysis of dynamical systems," *Mathematical and Computer Modelling of Dynamical Systems*, vol. 14, no. 2, pp. 147–175, 2008.

[23] M. Halgren, I. Ulbert, H. Bastuji, D. Fabó, L. Erőss, M. Rey, O. Devinsky, W. K. Doyle, R. Mak-McCully, E. Halgren, L. Wittner, P. Chauvel, G. Heit, E. Eskandar, A. Mandell, and S. S. Cash, "The generation and propagation of the human alpha rhythm," *Proceedings of the National Academy of Sciences*, vol. 116, no. 47, pp. 23 772–23 782, 2019. [Online]. Available: https://www.pnas.org/content/116/47/23772

[24] G. Hebbink, "Activity types in a neural mass model," M.Sc. Thesis, University of Twente, September 2014. [Online]. Available: http://essay.utwente.nl/66085/

[25] M. Desroches, O. Faugeras, and M. Krupa, "Slow-fast transitions to seizure states in the Wendling-Chauvel neural mass model," *Opera Medica et Physiologica*, no. 3-4, 2016.

[26] A. Blenkinsop, A. Valentin, M. P. Richardson, and J. R. Terry, "The dynamic evolution of focal-onset epilepsies–combining theoretical and clinical observations," *European Journal of Neuroscience*, vol. 36, no. 2, pp. 2188–2200, 2012.

[27] S. Ahmadizadeh, P. J. Karoly, D. Nešić, D. B. Grayden, M. J. Cook, D. Soudry, and D. R. Freestone, "Bifurcation analysis of two coupled Jansen-Rit neural mass models," *PloS one*, vol. 13, no. 3, p. e0192842, 2018.

[28] G. Huang, D. Zhang, J. Meng, and X. Zhu, "Interactions between two neural populations: A mechanism of chaos and oscillation in neural mass model," *Neurocomputing*, vol. 74, no. 6, pp. 1026–1034, 2011.

[29] F. Wendling, J.-J. Bellanger, F. Bartolomei, and P. Chauvel, "Relevance of nonlinear lumped-parameter models in the analysis of depth-EEG epileptic signals," *Biological cybernetics*, vol. 83, no. 4, pp. 367–378, 2000.

[30] M. L. Saggio, D. Crisp, J. M. Scott, P. Karoly, L. Kuhlmann, M. Nakatani, T. Murai, M. Dümpelmann, A. Schulze-Bonhage, A. Ikeda *et al.*, "A taxonomy of seizure dynamotypes," *Elife*, vol. 9, p. e55632, 2020.

[31] R. P. Grimaldi, *Discrete and Combinatorial Mathematics, 5/e*. Pearson Education India, 2006.

[32] R. Storn and K. Price, "Differential evolution–a simple and efficient heuristic for global optimization over continuous spaces," *Journal of global optimization*, vol. 11, no. 4, pp. 341–359, 1997.

[33] J. Kennedy and R. Eberhart, "Particle swarm optimization," in *Proceedings of ICNN'95-international conference on neural networks*, vol. 4. IEEE, 1995, pp. 1942–1948.

[34] M. Iwan, R. Akmeliawati, T. Faisal, and H. M. Al-Assadi, "Performance comparison of differential evolution and particle swarm optimization in constrained optimization," *Procedia Engineering*, vol. 41, pp. 1323–1328, 2012.

[35] J. Vesterstrom and R. Thomsen, "A comparative study of differential evolution, particle swarm optimization, and evolutionary algorithms on numerical benchmark problems," in *Proceedings of the 2004 congress on evolutionary computation (IEEE Cat. No. 04TH8753)*, vol. 2. IEEE, 2004, pp. 1980–1987.

[36] J. Brest, S. Greiner, B. Boskovic, M. Mernik, and V. Zumer, "Self-adapting control parameters in differential evolution: A comparative study on numerical benchmark problems," *IEEE transactions on evolutionary computation*, vol. 10, no. 6, pp. 646–657, 2006.

[37] D. Li, J. Chen, and B. Xin, "A novel differential evolution algorithm with gaussian mutation that balances exploration and exploitation," in *2013 IEEE Symposium on Differential Evolution (SDE)*. IEEE, 2013, pp. 18–24.

[38] J. Bezanson, A. Edelman, S. Karpinski, and V. B. Shah, "Julia: A fresh approach to numerical computing," *SIAM review*, vol. 59, no. 1, pp. 65–98, 2017. [Online]. Available: https://doi.org/10.1137/141000671

[39] M. A. Lopes, M. P. Richardson, E. Abela, C. Rummel, K. Schindler, M. Goodfellow, and J. R. Terry, "An optimal strategy for epilepsy surgery: Disruption of the rich-club?" *PLoS computational biology*, vol. 13, no. 8, p. e1005637, 2017.

[40] M. Goodfellow, C. Rummel, E. Abela, M. Richardson, K. Schindler, and J. Terry, "Estimation of brain network ictogenicity predicts outcome from epilepsy surgery," *Scientific reports*, vol. 6, no. 1, pp. 1–13, 2016.

[41] Y. A. Kuznetsov, *Elements of Applied Bifurcation Theory (3rd Ed.)*. Berlin, Heidelberg: Springer-Verlag, 2004.

Appendix A

Bifurcation theory

We give a brief introduction to bifurcation theory. For a full description of the field of bifurcation analysis we refer to the book by Yu. A. Kuznetsov [41]. We consider a system of ODEs of the form

$$\dot{x} = f(x, \beta) \tag{A.1}$$

where the state $x \in \mathbb{R}^n$ and parameters are $\beta \in \mathbb{R}^k$. A bifurcation point is defined as a point $\beta_0 \in \mathbb{R}^k$ such that within any neighbourhood of β_0 there exists a $\beta_1 \in \mathbb{R}^k$ so that no homeomorphism exists that maps orbits of the system $\dot{x} = f(x, \beta_1)$ to orbits of the system $f(x, \beta_0)$. Loosely speaking, a bifurcation point indicates a change in the type of orbits that can be obtained from a dynamical system. In this section, we review codimension 1 bifurcations. These are bifurcations that can occur in systems where $\beta \in \mathbb{R}$.

A.1 Local codimension 1 bifurcations

We first look into bifurcations of equilibria. An equilibrium of the system (A.1) is a point such that $f(x, \beta) = 0$. The stability of an equilibrium can be found by investigating the eigenvalues $\lambda_k \in \mathbb{C}$ where $k \in \{0, 1, ..., n\}$ of the Jacobian matrix $f_x(x, \beta)$ evaluated at the equilibrium. If the real parts of all eigenvalues are negative the equilibrium is stable. If the real part of at least one eigenvalue is positive the equilibrium is unstable. This leaves two critical cases, namely the case that $\lambda_k = 0$ for some $k \in \{1, 2, ..., n\}$ **or** the case that $\lambda_{j,k} = \pm i\omega$ for some $j, k \in \{1, 2, ..., n\}$, $j \neq k$ and $\omega > 0$.

In the case that $\lambda_k = 0$ and a normal form coefficient a is nonzero (for the computation of normal form coefficients we refer to Kuznetsov [41]) a fold bifurcation occurs. When such a fold bifurcation occurs at $\beta = \beta_0$ two equilibria which exist either for $\beta > \beta_0$ or $\beta < \beta_0$ collide and disappear on the other side of β_0. An example of the change of dynamics is shown in Figure A.1.

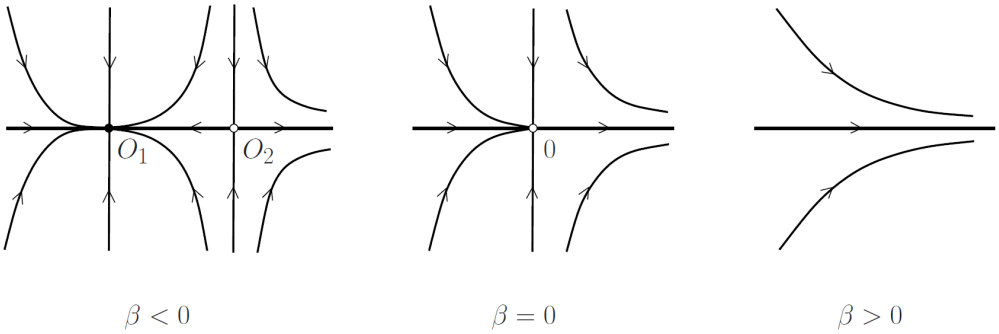

Figure A.1: Example of a fold bifurcation of equilibria, adapted from Kuznetsov [41]. Here, an equilibrium of saddle type O_2 and a stable node O_1 exist for $\beta < 0$. The two equilibria collide at $\beta = 0$. Neither equilbrium persists after the bifurcation point.

When $\lambda_{j,k} = \pm i\omega$ a Hopf bifurcation occurs. When a Hopf bifurcation occurs, a focus (equilibrium where the imaginary part of at least two eigenvalues of the Jacobian matrix are nonzero) changes stability. When this happens, a limit cycle emerges. Important in the consideration of Hopf bifurcations is the value of a coefficient called the first Lyapunov coefficient l_1. When this coefficient is larger than 0 a subcritical Hopf bifurcation occurs (Figure A.3). In this case, an unstable cycle disappears as the equilibrium switches from stable to unstable. On the other hand, if $l_1 < 0$ a supercritical Hopf bifurcation occurs and a stable cycle emerges from the Hopf bifurcation (Figure A.2). Lastly, we note that if $l_1 = 0$, the Hopf bifurcation is not generic and the analysis is more delicate.

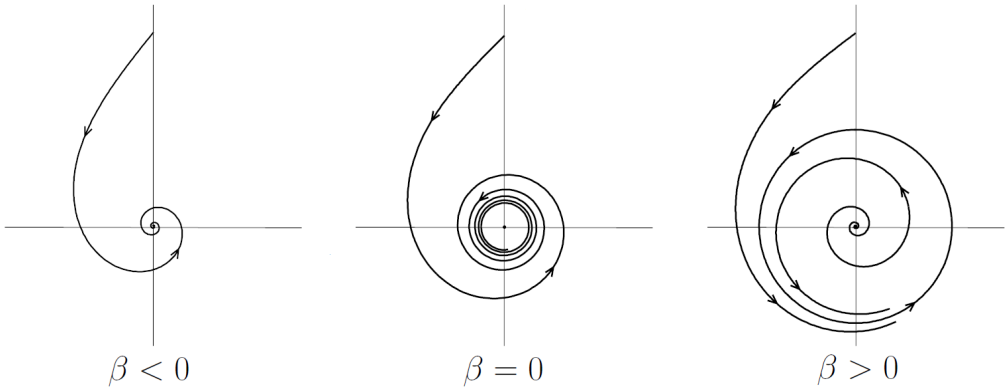

Figure A.2: Schematic view of a supercritical Hopf bifurcation, adapted from Kuznetsov [41]. Here, a stable focus exists for $\beta < 0$. After the Hopf bifurcation point at $\beta = 0$, the focus becomes unstable and a stable limit cycle emerges.

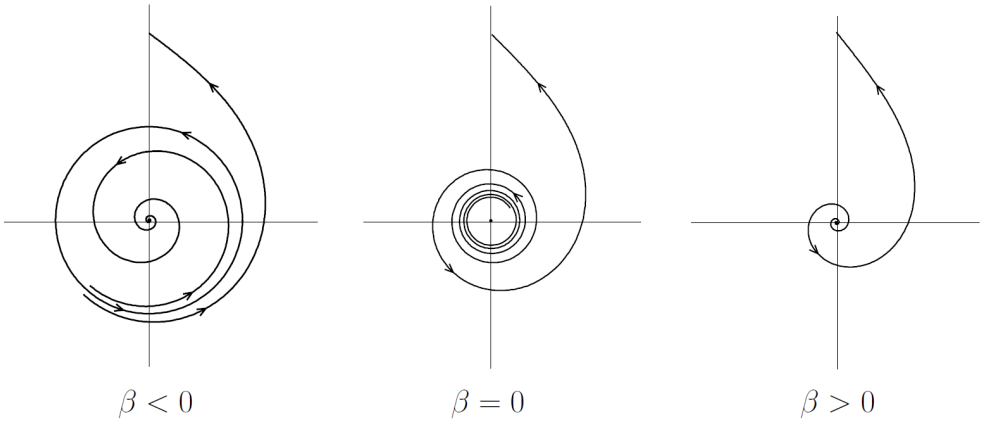

Figure A.3: Schematic view of a subcritical Hopf bifurcation, adapted from Kuznetsov [41]. Here, an unstable focus exist and an unstable cycle exist for $\beta < 0$. After the Hopf bifurcation point at $\beta = 0$, the focus becomes stable and the limit cycle ceases to exist.

A.2 Global codimension 1 bifurcations

We also describe codimension 1 bifurcations of cycles. Suppose that a cycle with period T_0 is given as $x^0(t)$. Then the monodromy matrix is given by $y(T_0)$ where $y(t)$ satisfies

$$\dot{y}(t) = f_x(x^0(t))y(t).$$

The monodromy matrix always has one trivial eigenvalue $\mu_n = 1$. When we consider the other eigenvalues of the monodromy matrix $\mu_k \in \mathbb{C}$, $k \in \{1, 2, ..., n-1\}$ the periodic orbit is stable if all of these eigenvalues satisfy $|\mu_k| < 1$ and is unstable if at least one eigenvalue has modulus larger than 1. In systems with dimension 3 or higher this leaves us with three critical cases:

- $\mu_k = 1$ for some $k \in \{1, 2, ..., n-1\}$.
- $\mu_k = -1$ for some $k \in \{1, 2, ..., n-1\}$.
- $\mu_{j,k} = e^{\pm i\theta}$ for some $j, k \in \{1, 2, ..., n-1\}$, $j \neq k$ and $0 < \theta < \pi$.

When $\mu_k = 1$ a fold of limit cycles (LPC) bifurcation occurs. This bifurcation corresponds to the collision and subsequent disappearance of two limit cycles in the system. A schematic view is given in Figure A.4.

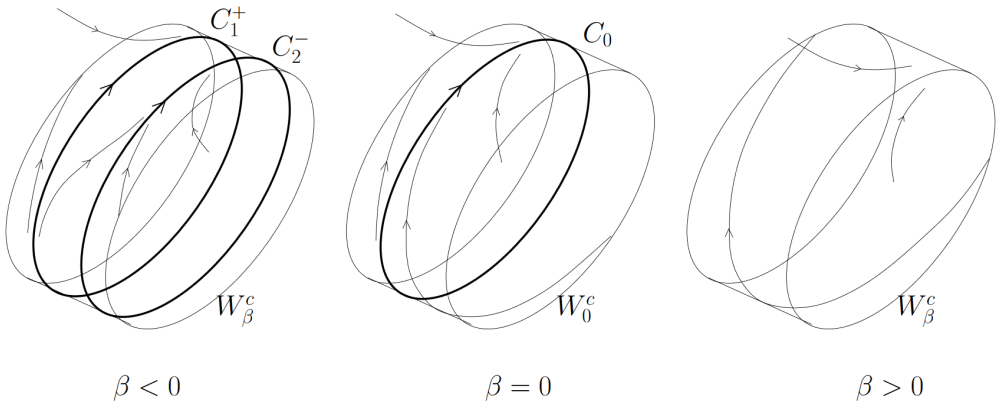

Figure A.4: Schematic view of an LPC bifurcation, adapted from Kuznetsov [41]. Here, two cycles exist for $\beta < 0$, one of which (C_1^+) is unstable and the other is stable (C_2^-). These cycles collide at the bifurcation point $\beta = 0$ and cease to exist for $\beta > 0$.

When $\mu_k = -1$ a period-doubling (PD) bifurcation occurs. This bifurcation corresponds to emergence of a cycle with twice the period of the original cycle. A schematic view is given in Figure A.5. We note that a common route to chaos in dynamical systems is a cascade of period-doubling bifurcations where period-doubling bifurcations occur closer and closer together leading to a chaotic attractor.

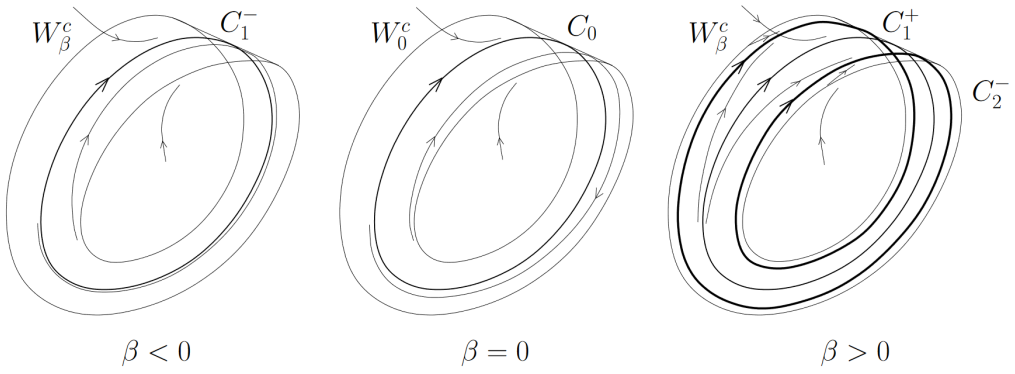

Figure A.5: Schematic view of a period-doubling bifurcation, adapted from Kuznetsov [41]. Here, one stable cycle C_1^- exists for $\beta < 0$. After the bifurcation point at $\beta = 0$, the original cycle becomes unstable and a new stable cycle with double period emerges (C_2^-).

When $\mu_{j,k} = e^{\pm i\theta}$ a Neimark-Sacker (NS) bifurcation occurs. From this bifurcation a torus-like structure or closed invariant curve emerges after the bifurcation point. This phenomenon is shown schematically in Figure A.6.

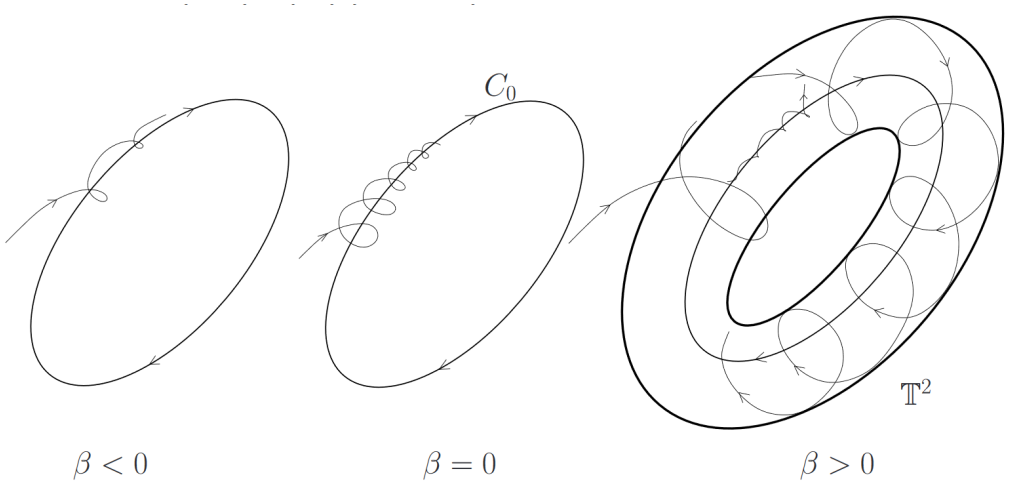

Figure A.6: Schematic view of a Neimark-Sacker bifurcation, adapted from Kuznetsov [41]. Here, a stable cycle C_0 exists for $\beta < 0$. After the bifurcation point, a stable torus $\mathbb{T}^2$ emerges and the cycle becomes unstable.

Lastly, we describe two types of homoclinic bifurcations. We recall that a homoclinic orbit is a solution $\phi(t)$ of the system (A.1) such that $\lim_{t\to-\infty} \phi(t) = \lim_{t\to\infty} \phi(t) = x_0$ where x_0 is a saddle equilibrium. A heteroclinic orbit is a solution $\phi(t)$ to the system (A.1) such that $\lim_{t\to-\infty} \phi(t) = x_0$ and $\lim_{t\to\infty} \phi(t) = x_1$ where x_0 and x_1 are both equilibria of the system.

The first homoclinic bifurcation we describe is a homoclinic-to-saddle bifurcation. When this bifurcation occurs, a homoclinic orbit exists exactly for the critical parameter. On one side of the bifurcation point a cycle emerges, the stability of which depends on properties of the homoclinic orbit. On the other side of the bifurcation point, the periodic orbit disappears. A schematic view of this bifurcation is given in Figure A.7.

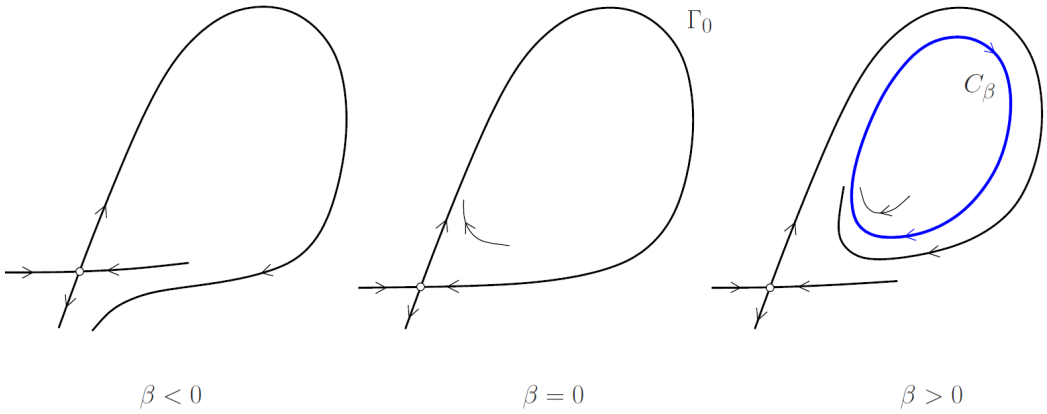

Figure A.7: Schematic view of a homoclinic-to-saddle bifurcation, adapted from Kuznetsov [41]. Here, for $\beta > 0$ a saddle point exists as well as a stable cycle C_β. At the bifurcation point $\beta = 0$, a homoclinic orbit Γ_0 exists. For $\beta < 0$, both the stable cycle and the homoclinic orbit disappear.

A second homoclinic bifurcation is the saddle-node on invariant curve (SNIC) bifurcation. In this case, two saddle points are connected through two heteroclinic orbits on one side of the bifurcation point. At the bifurcation point, a fold bifurcation occurs and the two saddle points coincide. This results in the existence of a homoclinic orbit. After the bifurcation point, a periodic orbit remains. This phenomenon is shown schematically in Figure A.8.

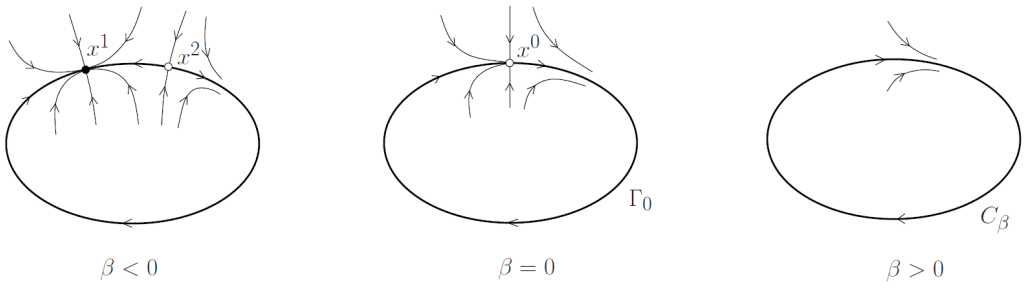

Figure A.8: Schematic view of a SNIC bifurcation, adapted from Kuznetsov [41]. Here, two saddle points x^1 and x^2 exist for $\beta < 0$ that are connected through two heteroclinic orbits. For $\beta = 0$, the two equilibria collide and a homoclinic orbit Γ_0 exists. For $\beta > 0$, both equilibria cease to exist and a stable cycle C_β remains.

Appendix B

The validity of ER networks

Due to the method by which ER networks are constructed from clinical data, it is possible that connections are added between nodes that are not connected in the underlying true network of connectivity within the brain. Namely, if a connection exists between A and C, and a stimulation pair (A, B) is chosen, a directed edge will also exist between B and C in the resulting ER network. We investigate whether this method of constructing ER networks qualitatively changes the network and thus whether ER networks can reliably be used to indicate connectivity between areas in the brain. In order to find an answer to our research question, we consider the values of several network measures that have been shown to be significant in previous research done on ER networks [4], [6]. We show that under the assumption of nearest neighbour coupling, ER networks can reliably be used to indicate connectivity between different areas of the brain.

We consider four network measures for directed graphs. For an introduction to graph theory, we refer to Grimaldi et al [31]. We denote the weighted network by $G(V, E)$. Moreover, we let $|V| = N$ and nodes are labelled $v_i \in V$, $i \in 1, ..., N$. We consider the in-degree defined as

$$d_{\text{i}}(v_i) = \sum_{j=1}^{N} A_{ji},$$

and the out-degree defined as

$$d_{\text{o}}(v_i) = \sum_{j=1}^{N} A_{ij}.$$

Moreover, we consider the closeness centrality defined as

$$c_{\text{c}}(v_i) = \left(\sum_{j=1, i \neq j}^{N} d(v_i, v_j) \right)^{-1}$$

where $d(v_i, v_j)$ is the shortest distance between nodes v_i and v_j in G. We also consider the eigenvector centrality $\mathbf{c}_{\text{e}} \in \mathbb{R}^N$ defined as the solution to the eigenvector problem

$$A\mathbf{c}_{\text{e}} = \lambda \mathbf{c}_{\text{e}}$$

where λ is the largest eigenvalue of A. The eigenvector centrality $\mathbf{c}_{\text{e}}$ defines a centrality measure for each node, given by the ith element $\mathbf{c}_{\text{e},i}$ for node v_i. If G has one strongly connected component, the solution to this eigenvector problem is unique up to scaling by the Perron-Frobenius theorem. The reasoning behind this choice for network measures is as follows. The in-degree and out-degree in electrodes in an ER network have both been found to correlate positively with the seizure-onset-zone and resected area [4]. Similarly, the in-degree, out-degree and eigenvector centrality all show a positive correlation to the amount of DRs in a node both in some individual patients and on the group level. Lastly, the closeness centrality characterizes the difference in path length between nodes. The path length between nodes has previously been found to correlate with the onset of DRs [6]. Hence, if these four network measures remain similar when adjusting weights within an ER network, we conclude that the adjusted network is similar to the original ER network.

When comparing measures for different networks, we use Spearman's rank correlation. In this method, each measure for a node in the original graph Y_i and measure for a node in the adjusted graph X_i is given a rank based on the ordering of these variables. The difference between the rank of X_i and the rank of Y_i is then denoted by d_i and Spearman's rank correlation can be calculated as

$$\rho = 1 - \frac{6 \sum_{i=1}^{n} d_i^2}{n(n^2 - 1)}.$$

Here, n denotes the amount of observations. For testing the null hypothesis that no correlation exists against a nonzero correlation a t-test can be applied.

We now assess how the method of constructing ER networks influences the properties of the resulting network. To do this, we first generate a graph representing the true network. We also choose stimulation pairs. We then construct a second network in the following way. For each stimulation pair in the true network (v_j, v_k) we add edges to the network according to the method of constructing ER networks that is used now (described in 4.2.1). That is, in the chosen patient network, we add an edge from v_i, $i \in \{j, k\}$ to v_l if an edge exists from v_m to v_l, $m \in \{1, 2\}, m \neq i$. We compare the network measures between the artificial "true" network and the network after adding connections. We use the eigenvector centrality, closeness centrality, in-degree and out-degree as our network measures of interest, and calculate Spearman's rank correlation. To test the null hypothesis that no correlation exists against a nonzero correlation a t-test is applied. The null hypothesis is rejected if $p < 0.05$. We define the adjusted network to be similar to the original network if there is a significant correlation between all considered network measures in the adjusted graph and the same network measures in the original random graph.

We generate two types of true networks. For both types, stimulation pairs are taken to be

adjacent electrodes on the rows of an 8×8 grid (similar to the method described in Chapter 4.2.4). We thus obtain $7 \times 8 = 56$ stimulation pairs. In the first method, the true network is taken to be a random Erdős-Rényi graph with 64 nodes and $p = 0.2$. For the second type a bias for nearest neighbour connections is added, and the method is analogous to the method described in Chapter 4.2.4. For each type, we construct 100 artificial networks.

For the 100 considered networks without bias for nearest neighbour connections, we find that 79 adjusted graphs are similar to the original graph. Considering the 100 networks with bias for nearest neighbour connections yielded 98 networks that were similar after adjustment. A comparison of the distributions of Spearman's rank correlation for the four considered network measures is given in Figure B.1. We see that Spearman's ρ is considerably larger in networks with nearest neighbour coupling for all considered network measures except the in-degree. We conclude that the constructed ER network do not change qualitatively if a bias for nearest neighbour coupling is assumed between electrodes.

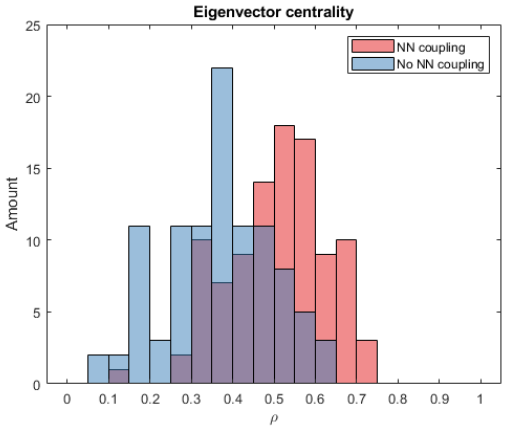

(a) Comparison of eigenvector centrality.

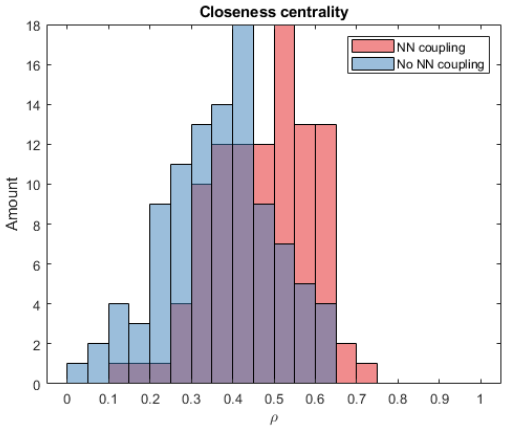

(b) Comparison of closeness centrality.

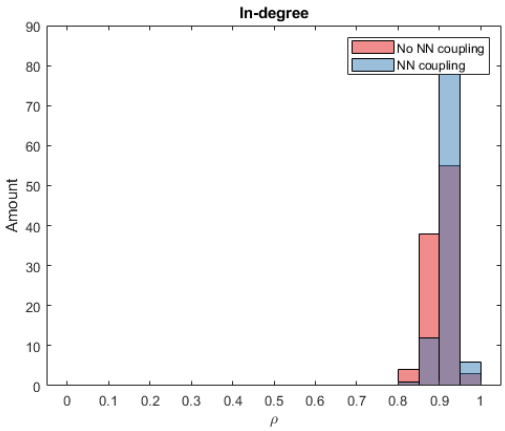

(c) Comparison of in-degree.

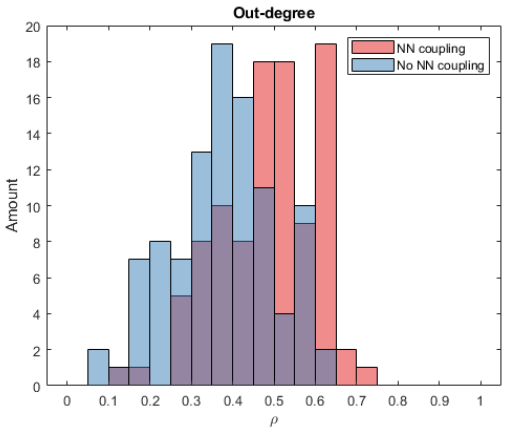

(d) Comparison of out-degree.

Figure B.1: Comparison of Spearman's rank correlation between the original network and networks after adjustment due to stimulation both in networks with nearest neighbour (NN) coupling and without nearest neighbour coupling.